NAVAL POSTGRADUATE SCHOOL

MONTEREY, CALIFORNIA

DISSERTATION

MATERIAL TRANSPORT IN THE INNER SHELF OF THE NORTHERN GULF OF MEXICO

by

Mathias K. Roth

December 2016

Dissertation Supervisor: Jamie H. MacMahan

Approved for public release. Distribution is unlimited.

THIS PAGE INTENTIONALLY LEFT BLANK

REPORT DOCUMENTATION PAGE		*Form Approved OMB No. 0704-0188*

Public reporting burden for this collection of information is estimated to average 1 hour per response, including the time for reviewing instruction, searching existing data sources, gathering and maintaining the data needed, and completing and reviewing the collection of information. Send comments regarding this burden estimate or any other aspect of this collection of information, including suggestions for reducing this burden, to Washington headquarters Services, Directorate for Information Operations and Reports, 1215 Jefferson Davis Highway, Suite 1204, Arlington, VA 22202-4302, and to the Office of Management and Budget, Paperwork Reduction Project (0704-0188) Washington, DC 20503.

1. AGENCY USE ONLY (*Leave blank*)	2. REPORT DATE December 2016	3. REPORT TYPE AND DATES COVERED Dissertation	
4. TITLE AND SUBTITLE MATERIAL TRANSPORT IN THE INNER SHELF OF THE NORTHERN GULF OF MEXICO		**5. FUNDING NUMBERS**	
6. AUTHOR(S) Mathias K. Roth			
7. PERFORMING ORGANIZATION NAME(S) AND ADDRESS(ES) Naval Postgraduate School Monterey, CA 93943-5000		**8. PERFORMING ORGANIZATION REPORT NUMBER**	
9. SPONSORING /MONITORING AGENCY NAME(S) AND ADDRESS(ES) N/A		**10. SPONSORING / MONITORING AGENCY REPORT NUMBER**	

11. SUPPLEMENTARY NOTES The views expressed in this thesis are those of the author and do not reflect the official policy or position of the Department of Defense or the U.S. Government. IRB number ____N/A____.

12a. DISTRIBUTION / AVAILABILITY STATEMENT Approved for public release. Distribution is unlimited.	12b. DISTRIBUTION CODE

13. ABSTRACT (maximum 200 words)

Material transport is investigated in the northern Gulf of Mexico with field observations obtained within the inner shelf, offshore of a beach where oil washed ashore following the Deepwater Horizon oil spill. In the fall, winter, and spring, extratropical cold air outbreaks frequently pass from the north, northwest across the nearly latitudinal coastline and experiment site, bringing winds that are stronger in the cross-shore than alongshore. Cross-shore winds drive depth-averaged along-shelf currents through an ageostrophic balance with the cross-shelf pressure gradient force and Coriolis force. Eulerian Acoustic Doppler Current Profiler and Lagrangian GPS-drifter-measured surface (< 1 m) currents differ from depth-averaged subsurface currents, and are 4–7 times larger than theoretical estimates of wind and wave-driven surface flow. Differences in surface flow are attributed to the presence of a buoyant river plume. Plume boundary fronts are sources of horizontal velocity and density gradients where drifters converge, slow, and are redirected. When the plume extended along the coast, 100% of drifters deployed offshore of the plume were barred from the beach. Plume kinematics and thickness, expected to be important for sustainment of the barrier, are examined with a one-year record of velocity observations in 10 m water depth.

14. SUBJECT TERMS material transport, inner shelf, cold air outbreak, coastline curvature, river plume, coastal barrier, HYCOM			**15. NUMBER OF PAGES** 113
			16. PRICE CODE
17. SECURITY CLASSIFICATION OF REPORT Unclassified	**18. SECURITY CLASSIFICATION OF THIS PAGE** Unclassified	**19. SECURITY CLASSIFICATION OF ABSTRACT** Unclassified	**20. LIMITATION OF ABSTRACT** UU

THIS PAGE INTENTIONALLY LEFT BLANK

MATERIAL TRANSPORT IN THE INNER SHELF OF THE NORTHERN GULF OF MEXICO

Mathias K. Roth
Lieutenant Commander, United States Navy
B.S., United States Naval Academy, 2002
M.S., Naval Postgraduate School, 2003

Submitted in partial fulfillment of the
requirements for the degree of

DOCTOR OF PHILOSOPHY IN PHYSICAL OCEANOGRAPHY

from the

NAVAL POSTGRADUATE SCHOOL
December 2016

Approved by: Jamie H. MacMahan   Ad J. H. M. Reniers
Professor of Oceanography   Professor of Fluid Mechanics
Dissertation Supervisor

Edward B. Thornton   Timour Radko
Professor Emeritus of Oceanography   Professor of Oceanography

Jeffrey Paduan   Wendell A. Nuss
Professor of Oceanography   Professor of Meteorology

Approved by: Peter Chu, Chair, Department of Oceanography

Approved by: Douglas Moses, Vice Provost of Academic Affairs

THIS PAGE INTENTIONALLY LEFT BLANK

ABSTRACT

Material transport is investigated in the northern Gulf of Mexico with field observations obtained within the inner shelf, offshore of a beach where oil washed ashore following the Deepwater Horizon oil spill. In the fall, winter, and spring, extratropical cold air outbreaks frequently pass from the north, northwest across the nearly latitudinal coastline and experiment site, bringing winds that are stronger in the cross-shore than alongshore. Cross-shore winds drive depth-averaged along-shelf currents through an ageostrophic balance with the cross-shelf pressure gradient force and Coriolis force. Eulerian Acoustic Doppler Current Profiler and Lagrangian GPS-drifter-measured surface (< 1 m) currents differ from depth-averaged subsurface currents, and are 4–7 times larger than theoretical estimates of wind and wave-driven surface flow. Differences in surface flow are attributed to the presence of a buoyant river plume. Plume boundary fronts are sources of horizontal velocity and density gradients where drifters converge, slow, and are redirected. When the plume extended along the coast, 100% of drifters deployed offshore of the plume were barred from the beach. Plume kinematics and thickness, expected to be important for sustainment of the barrier, are examined with a one-year record of velocity observations in 10 m water depth.

THIS PAGE INTENTIONALLY LEFT BLANK

TABLE OF CONTENTS

LIST OF FIGURES

LIST OF TABLES

THIS PAGE INTENTIONALLY LEFT BLANK

LIST OF ACRONYMS AND ABBREVIATIONS

ADCP	Acoustic Doppler Current Profiler
BP	British Petroleum
CAO	Cold Air Outbreak
CARTHE	Consortium for Advanced Research on Transport of Hydrocarbon in the Environment
CTD	Conductivity, Temperature, and Depth
DwH	Deepwater Horizon
hr	Hours
HYCOM	Hybrid Coordinate Ocean Model
GOM	Gulf of Mexico
GoMRI	Gulf of Mexico Research Initiative
JBP	John Beasley Park
kg	Kilograms
m	Meters
MSL	Mean Sea Level
N	Newton
NAVGEM	Navy Global Environmental Model
NEGoMex	Northeastern Gulf of Mexico
NGoMex	Northern Gulf of Mexico
NOAA	National Oceanic and Atmospheric Administration
OB	Orange Beach
PDF	Probability Density Function
ppt	Parts per thousand
psu	Practical salinity units
s	Seconds
SCOPE	Surfzone and Coastal Oil Pathways Experiment
USGS	United States Geological Survey
WFS	West Florida Shelf
YD	YearDays

THIS PAGE INTENTIONALLY LEFT BLANK

ACKNOWLEDGMENTS

I.   INTRODUCTION

On 20 April 2010, an explosion at the Macondo Oil Well 80 km SE of Louisiana's Bird's Foot Delta, within the northern Gulf of Mexico, initiated the largest accidental release of oil into the ocean to date (Kourafalou and Androulidakis 2013; Robertson and Krauss 2010). It is estimated that more than four million barrels of oil spilled during the Deepwater Horizon (DwH) oil spill (Mariano et al. 2011; Aigner et al. 2010). Efforts began immediately to contain the oil and mitigate its impact on the coastal environment. Officials from the U.S. government and academics, particularly from Gulf Coast state institutions, worked together to predict the paths of oil from deep waters at the Macondo Well, across the continental shelf, and ultimately to the beach and wetlands in the backshore. These efforts relied upon visual observations, satellite imagery, and ocean circulation models (NOAA 2010) and were intended to determine oil fate with confidence to address the numerous ecological, economic, and public health concerns associated with where the oil would flow and ultimately beach. Unfortunately, nearshore surface oil forecasts from the National Oceanic and Atmospheric Administration's Office of Response and Restoration (NOAA 2010) had large "uncertainty boundaries" and were often inconsistent between forecasts (Mariano et al. 2011). This presented additional challenges to mitigation efforts. The uncertainty also demonstrated a clear need to better understand and model the physical processes that are important for oil transport in the ocean.

Understanding the physical processes that control oil transport became one of the research themes for the Gulf of Mexico Research Initiative (GoMRI), which was established in May 2010 by British Petroleum (BP) as an independent research program with a $500 million commitment over 10 years (GoMRI 2016). Within GoMRI, the Consortium for Advanced Research on Transport of Hydrocarbon in the Environment (CARTHE) funded the Surf zone and Coastal Oil Pathways Experiment (SCOPE) in December 2013 to investigate transport in the nearshore. The efforts presented here are based on field observations obtained by instruments deployed during SCOPE. These observations are particularly important for future prediction of oil transport pathways

because the nearshore acts as a conduit between the deep ocean and the coastal ocean and bays and is the "last mile" for oil to transit before arriving at the beach. Progress in understanding the physical processes that force nearshore circulation, in particular, is necessary to improve the response to future oil spills (Dzwonkowski et al., 2014).

Here, circulation and material transport are studied in the inner shelf of the northern Gulf of Mexico (NGoMex) along the Florida Panhandle, where oil from DwH washed ashore in June 2010 (Aigner et al. 2010). The coastline in this region is nearly latitudinal and broken by a series of river inlets that discharge freshwater with the diurnal ebb tide. The tidal range in NGoMex is small, < 1.0 m and can be classified as microtidal (Seim et al. 1987; Valle-Levinson et al. 2015; Davies 1964). Circulation in this region is driven by synoptic wind forcing (Ohlmann and Niiler 2005), which is strongest during fall, winter, and spring when extratropical cyclones, known as Cold Air Outbreaks (CAO), routinely pass at 3–10 day intervals (Huh et al. 1984; Dagg 1988; Fernandez-Partegas and Mooers 1975; DiMego et al. 1976). Winds fluctuate predominantly onshore and offshore, but rotate 360° with passing storms in fall and winter, then become southeasterly in the spring and from the southwest during the summer (Guiterrez de Velasco and Winant 1996). Outside of periods with hurricanes, waves are typically small, < 1 m, as will be shown with observations in the following chapters. Owing to small waves and tides, and both synoptic and seasonal wind patterns, the NGoMex is well suited for studying cross-shore winds as a forcing mechanism for coastal circulation and material transport. The conditions in this region also aid in the investigation of the dynamics and kinematics of buoyant river plumes as they relate to material transport in the inner shelf, which can be studied during various wind speeds and directions.

The inner shelf exists within the nearshore, offshore of the surf zone, and is dynamically defined as the region where the surface and bottom boundary layers overlap (Lentz and Fewings 2012). The inner shelf does not have a set depth or offshore extent, but instead varies primarily with shelf slope, winds, and waves (Lentz and Fewings 2012). Cross-shore winds are more effective at driving cross-shelf transport than alongshore winds in the vertically well-mixed inner shelf (Lentz and Fewings 2012; Dzwonkowski et al. 2011). In the absence of wind, Stokes drift and undertow balance

each other and there is no net transport to the coast (Lentz et al. 2008). Along east and southern coasts of the United States, observational studies of the inner shelf momentum balance conclude that alongshore winds and pressure gradients are the most important mechanisms for along-shelf currents and transport (Fewings and Lentz 2010; Lentz et al. 1999; Liu and Weisberg 2005). Cross-shore winds have not been observed to drive sustained along-shelf currents or transport.

In Chapter II, the importance of cross-shore winds to the inner shelf circulation is investigated along the coastline from Mobile Bay, AL. to Panama City, FL. Based on a numerical modeling study on the West Florida Shelf (Li and Weisberg 1999a,b), cross-shore winds can drive along-shelf flows. Observations on the same shelf employed in an analysis of the inner shelf momentum balance suggest that cross-shore winds may become a driver of along-shelf currents during strong wintertime synoptic storms (Liu and Weisberg 2005). In this investigation, it is hypothesized that cross-shore winds drive along-shelf currents when synoptic storms cross coastlines that are oriented west to east. Wintertime field observations of inner shelf currents in 10 m water depth offshore of a latitudinal stretch of coastline and forced by passing synoptic storms are discussed. These observations are compared with numerical simulations from the Navy Global Environmental Model (NAVGEM) and the Hybrid Coordinate Ocean Model (HYCOM) to validate the use of simulations for analysis of the momentum balance. The momentum balance analysis is extended numerically to an additional 13 inner shelf stations to examine how coastline curvature affects the dynamics. This analysis is applied to rapid along-shelf current reversals that are well timed with passing CAO and observed at both straight and curved sections of coastline in the inner shelf of NGoMex (Crout 1983: Huh et al. 1984).

Buoyant river plumes that deliver brackish terrestrial water to the coastal sea are a second physical mechanism that can alter material transport pathways within the inner shelf. River plumes emerge with the ebb tide (Garvine 1984) and can proceed away from the inlet as a coastal current in the direction of a Kelvin wave (Horner-Devine et al. 2015). When they form, these currents are often shallow features that extend a few meters below the surface (Chapman and Lentz, 1994) that vertically thicken with downwelling

winds (Fong and Geyer 2001, 2002; Hetland 2005; Haus et al. 2003) and persist for tens to hundreds of kilometers along the coast before mixing with the ambient oceanic water (Garvine 1987; Garvine 1999; Yankovsky et al. 2000). Whether a plume creates a coastal current or not, density fronts form boundaries between the brackish riverine water and oceanic water (Garvine, 1987) where surface material converges and slows (Garvine, 1974; Garvine and Monk, 1974; Schroeder et al. 2012), altering material transport. Observations of the spatial and temporal influence of buoyant river plumes on inner shelf surface material transport are needed to improve the prediction of oil transport pathways.

In Chapter III, the effects of small-scale river plume on inner shelf circulation and transport are investigated. Buoyant river plumes have been the subject of numerous numerical and observational studies over the last half-century (Garvine 1974a, among others). These studies have focused on plume structure and dynamics and are summarized well in a review paper discussing mixing and transport in plumes (Horner-Devine et al. 2015). Kourafalou and Androulidakis (2013) employed a HYCOM-derived model and satellite imagery of the DwH oil spill to argue that high river discharge delayed oil from washing ashore along the Mississippi, Alabama, and Florida coastlines. In this study, small-scale plumes, like those found to the east of the Mississippi River, are hypothesized to disrupt surface oil transport pathways to the beach by becoming coastal barriers when the plume flows away from the inlet as a coastal current. Eulerian measurements of water column temperature, salinity, and velocities quantify the effect of the plume on surface currents. Lagrangian surface drifters, < 1m in height with GPS units affixed, are deployed in the river inlet and within the plume once it has emerged into the inner shelf to observe the temporal and spatial (X-Y plane) evolution of plume transport away from the inlet. Drifters deployed in the ambient shelf water are employed to observe interaction between surface material and plume boundaries. Drifter statistics quantify plume transport along the shelf and the role of the plume as a coastal barrier to cross-shelf material transport. This study describes a unique set of observations of surface material transport as forced by the interaction between winds from synoptic storms and a small-scale plume.

In Chapter IV, the far field region of the plume is explored further with a single Acoustic Doppler Current Profiler (ADCP) for one year within the inner shelf in 10 m water depth. The observations obtained are a unique record of plume front kinematics and thickness. Trends between the ambient currents and the velocity of the plume fronts and plume thickness are examined. Along-shelf straining and advection is expected to thicken (thin) the plume front when the ambient shelf currents and plume flow in the same (opposite) direction (Marques et al. 2010; Giddings et al. 2011). Similarly, downwelling (upwelling) winds are expected to thicken (thin) plume fronts based on numerical simulations (Fong and Geyer 2001) and observations (Haus 2003). The relationship between wind and plume thickness is explored across all seasons and synoptic conditions using a long-term wind record obtained from the NOAA Orange Beach buoy. Plume front velocity and thickness are likely measures of the effectiveness of the coastal barrier. Faster and thicker plume fronts are expected to correlate with more persistent and more extensive barriers than slower and thinner plume fronts.

In Chapter V, a summary of the results from SCOPE is provided. The importance of cross-shelf winds for inner shelf circulation within the NGoMex is addressed. Additionally, interaction between seasonal wind patterns and a small-scale plume are discussed. Coastal barriers that form as a result of interaction between the wind, ambient inner shelf currents, and plume are investigated as an important mechanism for inhibiting surface material transport across the inner shelf to the beach. The results presented here are expected to improve coastal circulation models and reduce uncertainty in oil fate predictions, providing dependable information for future response and mitigation efforts. The results also have application to military operations and should be considered in all phases of planning, from strategic to tactical, for missions in the littoral environment.

THIS PAGE INTENTIONALLY LEFT BLANK

II. ALONG-SHELF CURRENTS FORCED BY CROSS-SHORE WINDS IN THE INNER SHELF OF THE NORTHEASTERN GULF OF MEXICO

A. INTRODUCTION

Dynamically, the inner shelf is defined as the region offshore of the surf zone where the surface and bottom boundary layers intersect (Lentz and Fewings 2012). It is an important conduit for terrestrial pollution to move offshore and for material transport from the deep ocean to the beach. In this region, along-shelf currents are faster than cross-shelf currents due to the presence of the coastal boundary (Lentz and Fewings 2012). Unlike the mid- and outer continental shelves where alongshore winds drive both along-shelf and cross-shelf flows, in the inner shelf cross-shore winds are most effective at driving cross-shelf flows (Lentz and Fewings 2012; Fewings et al. 2008). Despite the faster along-shelf flow and importance of cross-shore winds, observational studies on broad, shallow inner shelves of the Gulf of Mexico and east coast of the United States typically conclude that cross-shore winds do not force along-shelf currents (Fewings and Lentz 2010; Lentz et al. 1999; Liu and Weisberg 2005). However, a three-dimensional numerical modeling study of the West Florida Shelf (WFS) indicates that cross-shore winds can produce along-shelf geostrophic currents through coastal setup and setdown (Li and Weisberg 1999a,b). On the same shelf, Liu and Weisberg (2005) suggest that cross-shore winds may become more important for inner shelf circulation during storms. Further investigation of the oceanic response to passing synoptic storms is necessary to resolve the role of cross-shore winds in driving inner shelf, along-shelf currents.

[a] Delft University of Technology, Delft, the Netherlands.

[b] Naval Postgraduate School.

[c] Rosentiel School of Marine and Atmospheric Science, University of Miami.

Wintertime extratropical cyclones increase wind stress as they rotate counter-clockwise and pass from the continental United States to over the Gulf of Mexico and east coast shelves (Huh et al. 1984; Crout 1983; Beardsley and Butman 1974). On the east coast, the track of the storm relative to the coastline determines how the cross- and alongshore components of the counter-clockwise winds force setup and setdown at the coast (Beardsley and Butman 1974; Beardsley et al. 1977). In the case of storms propagating north offshore of the coast, nor'easters ensue with alongshore winds that drive coastal setup (Beardsley et al. 1977; Lentz et al. 1999). Similarly, cold fronts that move southeast along the WFS force sea level variation along the coast (Marmorino 1982). Only cross-shore wind stress should be important to wind-driven setup when a storm moves along a nearly latitudinal coastline (Csanady 1982). When this scenario developed on the east-west oriented southern coast of Long Island, NY a 3 hr offshore wind impulse was observed to drive a westward current within the inner shelf (Csanady 1980). However, storm trajectories rarely align so well with latitudinal coastlines on the east coast of the United States (Csanady 1982). Consequently, infrequent and short-lived cross-shore wind impulses from nor'easters are likely not a significant forcing mechanism for along-shelf currents and material transport on east coast shelves.

In contrast, the northern Gulf of Mexico coastline is nearly latitudinal from east of Texas at the West Louisiana Inner Continental Shelf to the northwest portion of the WFS. Cold fronts associated with strong winter extratropical storms, also referred to as Cold Air Outbreaks (CAO), propagate west to east along this coast at speeds of 7–9 ms^{-1} (Feng and Li 2010; Price 1976; Fernandez-Partegas and Mooers 1975). CAO routinely pass at 3–10 day periods during winter, but also occur regularly in the fall and spring (Huh et al. 1984; Dagg 1988; Fernandez-Partegas and Mooers 1975; DiMego et al. 1976). CAO are less frequent in summer (DiMego et al. 1976; Henry 1979). Atmospheric pressure decreases steadily ahead of the front, levels off when the front arrives, and rapidly increases after the cold front passes (Huh et al. 1984). When the front arrives, the wind shifts from steady southwesterly pre-front to steady northwesterly post-front over ~140 km and 4.5 hours, on average (Fernandez-Partaga and Mooers 1975). Subsurface coastal current reversals of 0.30 ms^{-1} or more in <1 day are well-timed with the arrival of the

cold fronts in both the West Louisiana Inner Continental Shelf and near Panama City, in the inner shelf of the WFS (Crout 1983; Huh et al. 1984). However, an explanation of the dynamics leading to these rapid current reversals is missing from the literature. Alongshore winds are not expected to explain large current accelerations in the inner shelf of the northern Gulf of Mexico because the cold front commonly propagates nearly perpendicular to the coastline and cross-shore wind stress, pre- and post-front, should be the more important component of the wind forcing.

In this study, local wind forcing and along-shelf flows, including frequent and rapid along-shelf current reversals, are examined in the inner shelf of the northeastern Gulf of Mexico (NEGoMex). The orientation of this coastline is east to west near the Alabama-Florida border but changes to northwest to southeast on the WFS. It is hypothesized that cross-shore wind stress drives along-shelf currents along the latitudinal portion of the coast. The Surfzone and Coastal Oil Pathways Experiment (SCOPE) collected observations of wind stress and currents offshore of the Florida Panhandle, along a straight, nearly latitudinal section of the coastline. Output from a Gulf of Mexico Hybrid Coordinate Ocean Model (HYCOM) simulation forced by wind stress from the Navy Global Environmental Model (NAVGEM) augment the investigation at the field site. Details of SCOPE and HYCOM are provided in Section 2. The forcing mechanisms that drive along-shelf currents are determined by evaluating the depth-averaged, time-variant along- and cross-shelf momentum balances with field observations and model output at the field site (Section 3). Using model simulations only, local momentum balances are evaluated at an additional 14 inner shelf sites to determine the effects of coastline curvature on the forcing mechanisms and along-shelf current response. In Section 4, the dynamics of along-shelf flows forced by cross-shore winds are discussed in the context of rapid current reversal generation, timing, and persistence along the NEGoMex coastline.

B. METHODS

1. Inner Shelf Field Experiment

SCOPE was a nearshore experiment that focused on circulation offshore of John Beasley Park (JBP) 7 km west of Choctawhatchee Bay in Destin, FL., where oil washed ashore during the Deepwater Horizon oil spill in 2010 (Huguenard et al. 2016; Brouwer et al. 2015; Roth et al., submitted). The principal goal of SCOPE was to improve understanding of the physical mechanisms that combine to transport oil and other materials across the inner shelf to the beach and along the coastline. A Nortek Aquadopp 2 MHz Acoustic Doppler Current Profiler (ADCP) with a co-located pressure sensor was deployed to monitor inner shelf coastal currents and waves in 10 m water depth (Fig. 2.1, red triangle). The ADCP was located 500 m offshore of a nearly east-west portion of the NEGoMex coastline from December 2013 through November 2014. Cross-shelf (u) and along-shelf (v) velocity data were recorded in 50 cm vertical bins at 1 Hz. In this location, the near-surface current data in the top 1 m of the water column can be different in direction and magnitude than the subsurface currents owing to the presence of a buoyant river plume (Roth et al. submitted). Consequently, only the subsurface observations below 8.5 m were retained for describing the depth-averaged flow.

Wind stress was calculated following Large and Pond (1981) from hourly wind observations at the Orange Beach (OB) NOAA buoy 100 km west, southwest of JBP (Fig. 2.1, orange circle). OB anemometer data are available throughout the experiment and are advantageous because the buoy is located 20 km offshore, away from man-made structures and topography that can bias observations. Though distant, OB winds compare favorably with those measured by a 10 m wind tower erected in the backshore of JBP for two weeks in December 2013. Wind stress records from OB and the JBP tower have correlation coefficients of r = 0.90 in the cross-shore and r = 0.66 in the alongshore. In this study, all correlations are made to the 95% confidence level.
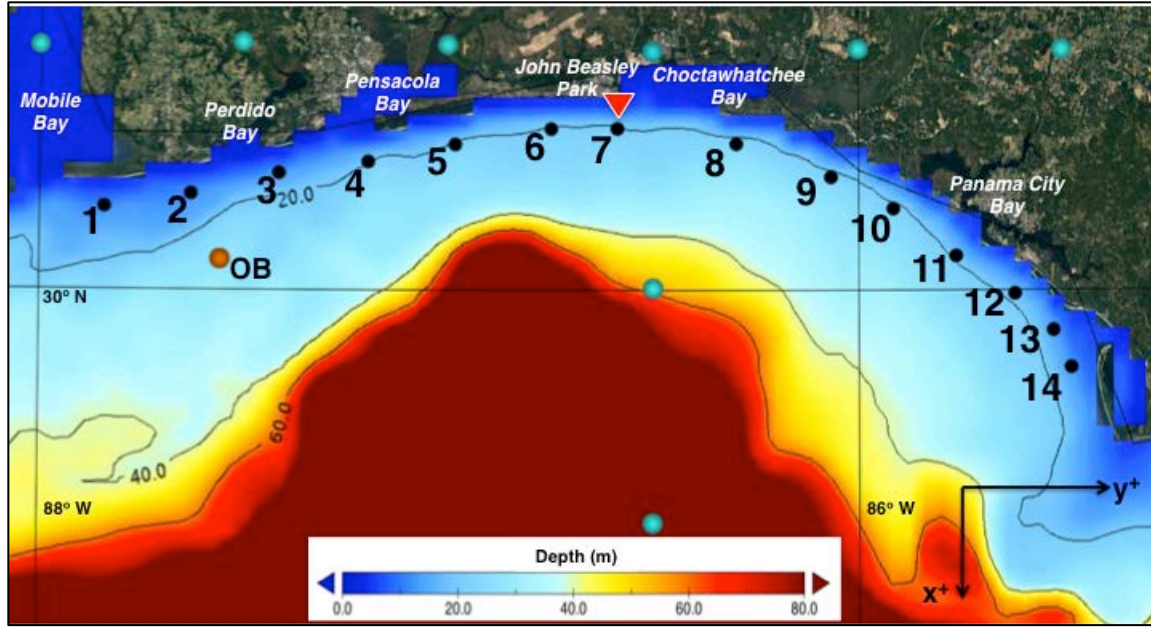
Northeastern Gulf of Mexico displayed in Google Earth with HYCOM bathymetry overlaid. Depth contours are in 20 m increments. The seaward extent of the inner shelf is expected to be within the light blue region. The northern tip of the 60 m contour is the onshore extent of DeSoto Canyon. Red triangle indicates the location of the 10 m ADCP at John Beasley Park. Orange circle is the Orange Beach buoy. Light blue circles represent the NAVGEM wind stress grid. Black circles show the locations of 14 stations along the coast where the momentum balances are calculated. At each station x is positive offshore and y is positive eastward, parallel to the coastline.

Figure 2.1.   John Beasley Park and the Northeastern Gulf of Mexico

2.   Regional Model Simulation

All modeled parameters employed in this study were retrieved from publically available archives on HYCOM.org. Specifically, sea surface height (η), and u and v components of the current were drawn from a regional Gulf of Mexico simulation conducted by the Naval Research Laboratory that spanned April 2009 through July 2014 (GOM 10.04/Experiment 31.0; HYCOM.org). The simulation was run by the Major Shared Resource Center at the Naval Oceanographic Office at $1/25^{\circ}$ resolution, and output parameters were projected to a rectilinear grid with ~3.8 km resolution in both the cross-shelf, x, and along-shelf, y, at this latitude. Previous nearshore studies involving ocean currents on the WFS (Olascoaga et al. 2008) and wind-driven circulation in the northern Gulf of Mexico (Schiller et al. 2011), among others, have also relied upon regional Gulf of Mexico HYCOM simulations. HYCOM simulations include satellite

11

altimetry and in situ hydrographic observations, which are ingested through Navy Coupled Ocean Data Assimilation. River input to the inner shelf is accounted for as a surface salinity flux term. For the period of interest, the regional simulation is forced by 3 hr wind stress from NAVGEM at ½^o resolution, as depicted by light blue circles in Figure 2.1. Note that the full NAVGEM grid and HYCOM grid points are not shown for aesthetic reasons.

This study is focused on a 6-month period during the winter of 2013–2014 and the spring of 2014, when CAO are frequent, and before the end of the HYCOM simulation in the summer of 2014. Specifically, the period of investigation is from December 2013 through May 2014, YearDays (YD) -27 through 151. Negative YD describe values from 2013, whereas positive values represent 2014.

3.   Momentum Balance Analysis

An analysis of the subtidal, time-variant, depth-averaged momentum balance is conducted to determine the terms that force the along-shelf currents. This procedure follows that of momentum balance investigations in the inner shelf of the east coast (Fewings and Lentz 2010; Lentz et al. 1999) and WFS (Liu and Weisberg 2005). Of the two east coast studies, Fewings and Lentz (2010) examined the momentum balance along the southern, latitudinal coastline of Martha's Vineyard, MA. and Lentz et al. (1999) observed the balance at Duck, NC. along a nearly longitudinal stretch of coastline. The WFS study occurred offshore of Sarasota, FL. where the coastline is more longitudinal than latitudinal. The horizontal momentum equations for all three of these studies are reduced forms of the depth-averaged equations provided by Lentz and Fewings (2012) for the along-shelf,

$$\frac{\partial \bar{v}}{\partial t} + f(\bar{u} + \bar{u}_{st}) = -\frac{1}{h\rho_0}\int_{-h}^{0}\frac{\partial p}{\partial y}dz + \frac{\tau^{sy}-\tau^{by}}{h\rho_0} - \frac{1}{h\rho_0}\left(\frac{\partial S^{xy}}{\partial x} + \frac{\partial S^{yy}}{\partial y}\right) - \frac{\tau^{bwy}}{h\rho_0} \quad (1)$$

(1)   (2)   (3)   (4)   (5) (6)   (7)   (8)   (9)

and cross-shelf,

$$\frac{1}{h\rho_0}\int_{-h}^{0}\frac{\partial p}{\partial x}dz = f(\bar{v} + \bar{v}_{st}) + \frac{\tau^{sx}-\tau^{bx}}{h\rho_0} - \frac{1}{h\rho_0}\left(\frac{\partial S^{xx}}{\partial x} + \frac{\partial S^{yx}}{\partial y}\right) - \frac{\tau^{bwx}}{h\rho_0}, \quad (2)$$

(10)   (11) (12)   (13)(14)   (15) (16)   (17)

where each term is: the change of local along-shelf velocity with time, (1); Coriolis, (2) and (11); Stokes-Coriolis, (3) and (12); along- and cross-shelf pressure gradients, (4) and (10); along- and cross-shore wind stress, (5) and (13); along- and cross-shelf bottom stress, (6) and (14); cross-shelf gradient, (7) and (15), and along-shelf gradient, (8) and (16), of wave radiation stresses; and along- and cross-shelf wave bottom stresses, (9) and (17). $\bar{u}$ in terms (2) and (3), and $\bar{v}$ in terms (1), (11), and (12) are depth-averaged velocities in the cross- (x) and along-shore (y) directions. x is positive offshore, y is positive east along the coast, and z is positive upward and zero at the surface. A local cross-shelf acceleration term, $\frac{\partial \bar{u}}{\partial t}$, is not included in Equation (2) because of the small values of $\bar{u}$ near the coast (Lentz and Fewings 2012). Note that Lentz and Fewings (2012) neglect both the nonlinear advection terms and nonlinear terms resulting from the interaction of waves and current to focus on the linear form of the momentum equations given in Equations (1) and (2).

In all three studies, analysis of the inner shelf momentum balance begins by finding the standard deviations of the subtidal records for each term. The along- and cross-shelf equations are treated separately. Terms with standard deviations an order of magnitude smaller than the largest term are assumed to make small contributions to the balance and are removed from further consideration. Of the remaining terms, each record is correlated with the record of the term that has the greatest variability. Terms with significant correlations are considered important for the respective momentum balance and are retained. Finally, all kept terms are individually, then cumulatively linearly regressed to the term with greatest variability. When the slope of the linear regression is equal to 1 the balance is closed by the terms involved in the regression.

The assumptions and results from the three studies discussed above are evaluated to determine the form of horizontal momentum balance equations employed here. Wave terms are only considered in the east coast studies. The Stokes-Coriolis terms were only evaluated at Martha's Vineyard but were found to be small and discarded from the balances by Fewings and Lentz (2010). With the exception of $\frac{\partial s^{xx}}{\partial x}$, the wave radiation stress terms associated with shoaling waves outside the surf zone do not contribute to the

momentum balances (Fewings and Lentz 2010; Lentz et al. 1999). $\frac{\partial s^{xx}}{\partial x}$ can be the same order of magnitude as both the Coriolis and cross-shore wind stress terms (Lentz and Fewings 2012), but is not correlated with the cross-shelf pressure gradient term (Fewings and Lentz 2010) and generates a setdown that is counteracted by wind-driven setup during passing nor'easters (Lentz et al. 1999) in ~10 m water depth. The significant wave heights were 0.5 – 3 m at Martha's Vineyard and 0.2 to 4 m at Duck in ~10 m water depth, respectively (Fewings and Lentz 2010; Lentz et al. 1999), which are ~1-2 m larger than those observed during periods of southerly winds ahead of CAO in the northeastern Gulf of Mexico during winter (Huh et al. 1984). Therefore, waves are not expected to contribute to the momentum balance and are dropped from Equations (1) and (2).

In all three studies, the along-shelf balance includes wind stress, pressure gradient, and bottom stress, and terms (4), (5), and (6) are retained. Following Lentz and Fewings (2012), the bottom stress term can be evaluated as a function of $\bar{v}$ as $\frac{b\bar{v}}{h}$, where h is water depth and b is a linear drag coefficient equal to 5.0×10^{-4} ms^{-1}. Comparisons of observations and model simulations of the along-shelf velocities with different values of b demonstrate that the value of b above is correct for 10 m water depth on the WFS (Liu and Weisberg 2005). Bottom stress values calculated with b are found to be consistent with those calculated from quadratic theory in 12 m depth (Fewings and Lentz 2010) and log profiles in 21 m depth (Lentz et al. 1999), the range of water depths considered in this study (Fig. 2.1). Liu and Weisberg (2005) report that the along-shelf balance closes best with secondary contributions from the local acceleration and Coriolis terms. However, the along-shelf Coriolis term is often smaller than the other terms inside the 20 m isobath (Lentz and Fewings 2012); therefore, term (1) is kept but term (2) is discarded. The depth-averaged along-shelf momentum balance is:

$$\frac{\partial \bar{v}}{\partial t} + \frac{b}{h}\bar{v} = -\frac{1}{h\rho_0}\int_{-h}^{0}\frac{\partial p}{\partial y}dz + \frac{\tau^{sy}}{h\rho_0}, \tag{3}$$

where ρ_0 is the reference water density, 1025 kgm^{-3}.

For the cross-shelf equation, terms (10) and (11) helped close the balance in all 3 studies. Owing to the small values of terms that contain $\bar{u}$ in all 3 studies, term (14) is dropped because it is a frictional response to $\bar{u}$ and is therefore assumed to be small and insignificant to the cross-shelf balance. Only terms (10), (11), and (13) are kept and the depth-averaged cross-shelf momentum balance is,

$$f\bar{v} = \frac{1}{h\rho_0}\int_{-h}^{0}\frac{\partial p}{\partial x}dz - \frac{\tau^{sx}}{h\rho_0}, \tag{4}$$

where f is the Coriolis parameter equal to 7.3×10^{-5} s^{-1}, and the along-shelf velocity appears within the Coriolis term.

The pressure gradient terms in Equations (3) and (4) are re-written as gradients of sea surface elevation, $\frac{\partial \eta}{\partial x,y}$, because density measurements from the 10 m site reported by Roth et al. (submitted) suggest that the pressure gradient can be assumed to be barotropic:

$$\frac{\partial \bar{v}}{\partial t} + \frac{b}{h}\bar{v} = -g\frac{\partial \eta}{\partial y} + \frac{\tau^{sy}}{h\rho_0}, \tag{5}$$

and

$$f\bar{v} = g\frac{\partial \eta}{\partial x} - \frac{\tau^{sx}}{h\rho_0}, \tag{6}$$

where $g = 9.81$ ms^{-2} and η is sea surface elevation. With the equations in this form model simulations of η can be used to determine the forcing mechanisms that drive along-shelf velocities in multiple locations along the coastline. The terms in Equations (5) and (6) have been organized so that terms with $\bar{v}$ on the left hand side are the response to forcing from pressure gradients and wind stresses. Note that all terms have units of ms^{-2}, but that each term is equivalently a force per unit mass, and will be referred to simply as a force, for brevity.

The momentum balance analysis procedure discussed above is applied to determine the mechanisms that force along-shelf currents at the location of the ADCP along the latitudinal section of the NEGoMex coastline (Fig. 2.1, red triangle). The time series of each term is filtered using a 33 hr running average to focus on subtidal forcing and response. The analysis is then extended along the coastline, east and west of the field site to 14 inner shelf locations, to determine how the terms within the momentum balances change with coastline curvature (Fig. 2.1, black circles). Each of the 14 stations

15

is located 6 km offshore, perpendicular to the local coastline. This distance is selected to ensure that there is at least one model grid point on each side of the station for calculations of pressure gradients, while still remaining well within the inner shelf.

Calculations of the radius of curvature (RC) quantify coastline curvature. The coastline that bounds the full extent of the experiment domain from station 1 to 14, has a RC of ~175 km (Fig. 2.1). Sections of the coast with RC values that exceed this total RC are considered straight. Local RC values that are small compared to the total RC occur along curved portions of the coast. The segment of coastline from station 1 to station 7 (JBP) has a RC of 735 km, and is considered straight. The coastline between stations 8 and 14 has a RC of 141 km and is considered curved. The RC at individual stations will be discussed below.

C.   RESULTS

1.   Observations of Along-shelf Currents and Cross-shore Winds at John Beasley Park

Subtidal, depth-averaged currents are consistently faster in the along-shelf component, $O(0.20 \text{ ms}^{-1})$, than the cross-shelf component, typically $O(0.02 \text{ ms}^{-1})$, as measured by the ADCP (Fig. 2.2a). A similar relationship was observed during a multi-year ADCP deployment offshore of Mobile Bay, AL. in 20 m water depth (Dzwonkowski and Park 2010). The standard deviations of $\bar{u}$ and $\bar{v}$ are 0.02 ms^{-1} and 0.05 ms^{-1} respectively, providing additional support for neglecting terms with $\bar{u}$, as well as the cross-shelf bottom stress term, from the momentum equations. The slow oscillation of the cross-shelf component of the current as the along-shelf component quickly reverses between westward and eastward indicates that the depth-averaged flow is an alternating along-shelf coastal current in 10 m water depth (Fig. 2.2a). The shift in current from up-coast to down-coast is frequent, but aperiodic.

16
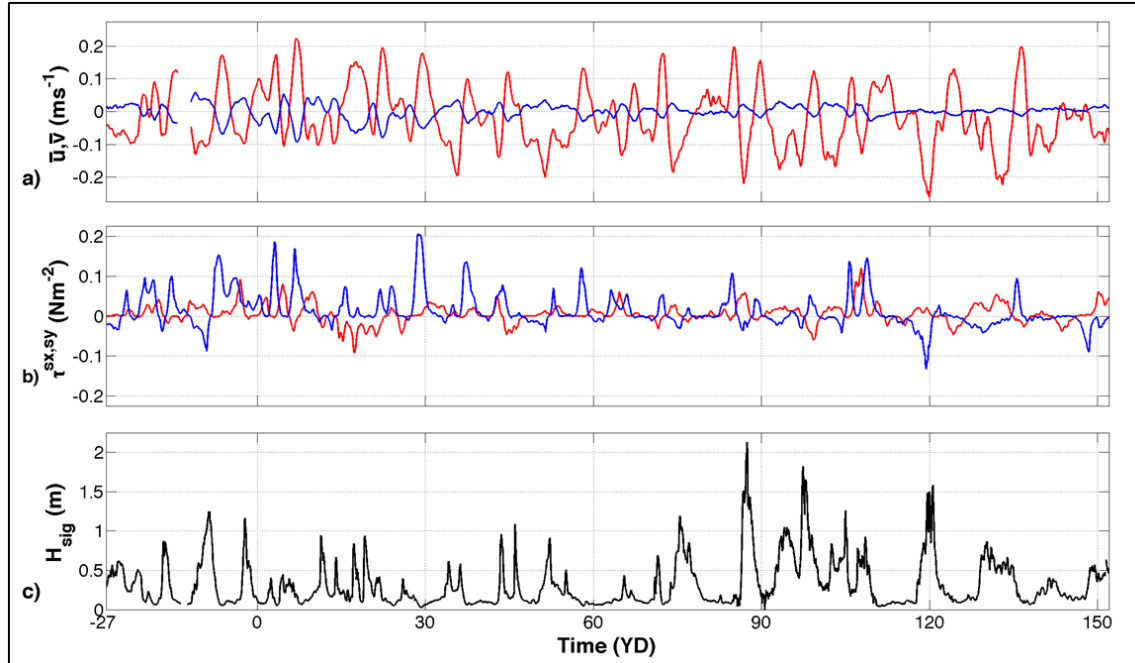
a) Subtidal (33 hr), depth-averaged, along-shelf (red) and cross-shelf (blue) currents at JBP, with positive values to the east and north. b) 33 hr-averaged alongshore (red) and cross-shore (blue) wind stress components from the Orange Beach NOAA buoy (Station #42012). Positive values are from the east and north. c) Hourly significant wave height at 10 m water depth measured by the ADCP.

Figure 2.2.   Field Observations of Currents, Wind Stress, and Wave Height

The cross-shore wind stress is frequently $O(0.1 \ Nm^{-2})$ when the wind blows from the north and is generally larger in magnitude than the along-shelf wind stress (Fig. 2.2b). Strong oscillations of the cross-shore component of wind stress are indicative of CAO passing the OB buoy. Though these storms occur throughout the winter and spring, the period of investigation will be referred to as winter, consistent with the synoptic winter season in the northern Gulf of Mexico that includes fall, winter and spring (Gutierrez de Velasco and Winant 1996; Wang et al. 1998).

During the winter, eastward currents occur with wind stress from the north, and westward flow aligns with southerly wind stress (Fig. 2.2a,b). The mean along-shelf current per increment of wind stress is used to further evaluate this relationship (Fig. 2.3). Every sixth data point from both the alongshore and cross-shore wind stress hourly, subtidal records (6 hour decimation) are sorted into 0.05 Nm^{-2} bins between -0.2 and 0.2

17

Nm^{-2}. A mean value for $\bar{v}$ is only calculated if 5 or more observations of $\bar{v}$ exist within a particular wind stress bin. Mean $\bar{v}$ flow to the west with easterly alongshore wind stress and to the east with westerly alongshore wind stress (Fig. 2.3a). Mean $\bar{v}$ are eastward with northerly wind stress and westward with southerly wind stress (Fig. 2.3b).
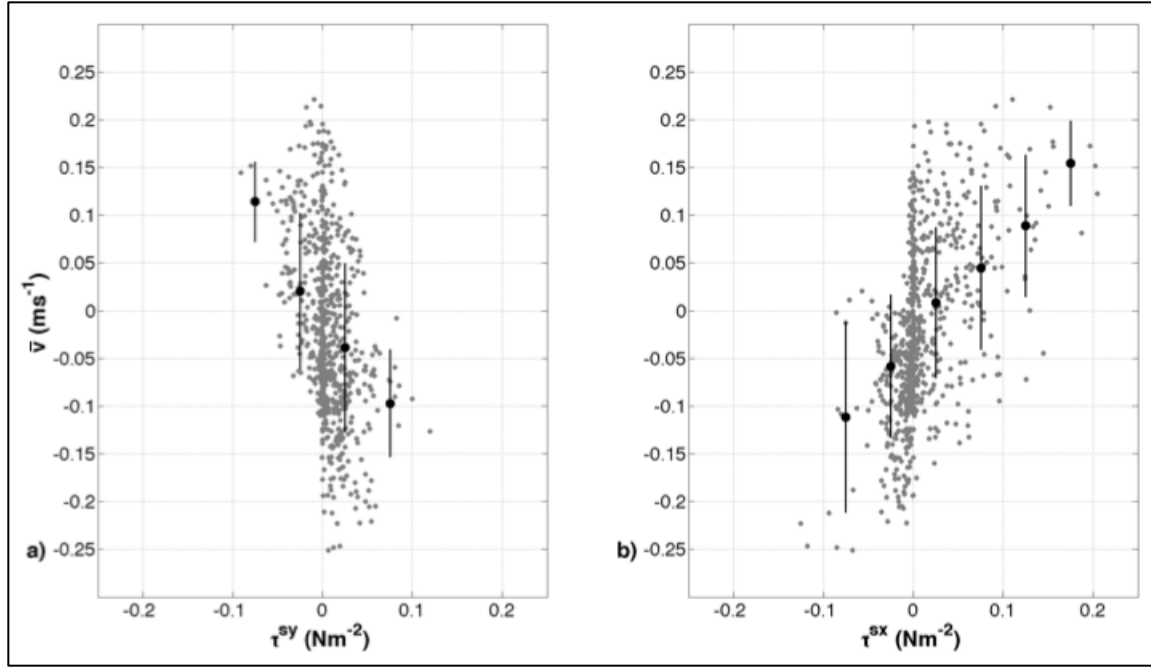
Scatter plots of subtidal, depth-averaged, along-shelf currents with 33 hr averaged a) alongshore and b) cross-shore wind stresses. Gray circles represent along-shelf flow as a function of wind stress. Black circles are the mean current per wind stress bin. Standard deviations of the currents are depicted with black vertical lines. Positive currents are to the east and negative currents are to the west. Positive values of wind stress are from the east in a) and from the north in b). Winter wind stress and current records are decimated by 6 hours.

Figure 2.3.   Wind Stress and Along-shelf Currents

Onshore winds generate waves with typical periods of 6–7 sec. On average, significant wave height (Hsig) is 0.3 m and infrequently rises above 1 m (Fig. 2.2c). Waves are largest when winds are from the south (Fig. 2.2b,c), but are small compared to the waves observed at Duck and Martha's Vineyard. At maximum observed significant wave height, wave breaking is expected to occur in ~4.0 m water depth. This follows from Thornton and Guza (1983), who demonstrate that the depth that waves break is

18

$h = Hsig/\gamma$, where $\gamma = 0.6$. Based on maximum observed Hsig, waves do not break in 10 m water depth and the ADCP is outside the surf zone in the inner shelf for the duration of the winter. Therefore, small waves are not expected to force along-shelf currents and neglecting wave terms from the momentum balances is appropriate.

a.   Passage of a Cold Air Outbreak

On YD -20, a cold front passes JBP with high-pressure systems behind the front over Texas (1033 mb) and Tennessee (1030 mb) and a low-pressure system (1013 mb) ahead of the front over South Carolina (Fig. 2.4a). The strong atmospheric pressure gradient causes winds to blow from the north toward JBP and NAVGEM simulations produce 3 hr averaged wind stress values of ~0.2 Nm^{-2} over the ADCP (Fig. 2.4b). Modeled southwest winds ahead of the front are O(0.1 Nm^{-2}). The counter-clockwise rotation of wind around the low-pressure system is well documented in the surface analysis chart (Fig. 2.4a).

When the atmospheric front arrives at JBP westward flowing, -0.15 ms^{-1} currents slow to 0 ms^{-1} after ~1 hr (0.05 YD) and reverse to eastward at 0.15 ms^{-1} in the ~5 hr period between YD -20.7 and YD -20.5 (Fig. 2.4c). Eastward flow continues throughout the day and into YD -19 (Fig. 2.4c). The currents shown in Figure 2.4c are sampled at 1 Hz and averaged over 2.5 min, instead of 33 hr, to emphasize the speed of the response of the currents to the passing storm. By assuming that the westward flow is steady before and after the current reversal the frictional timescale from Lentz and Fewings (2012), $T_f = \frac{h}{b}$, demonstrates that b is equal to 5.6E-4 in 10 m water depth, and validates the use of the linear drag coefficient given above. Based on observations of atmospheric pressure changes and 33 hr-averaged wind shift patterns, an additional 20 current reversals driven by CAO occur during this 6-month study.

19
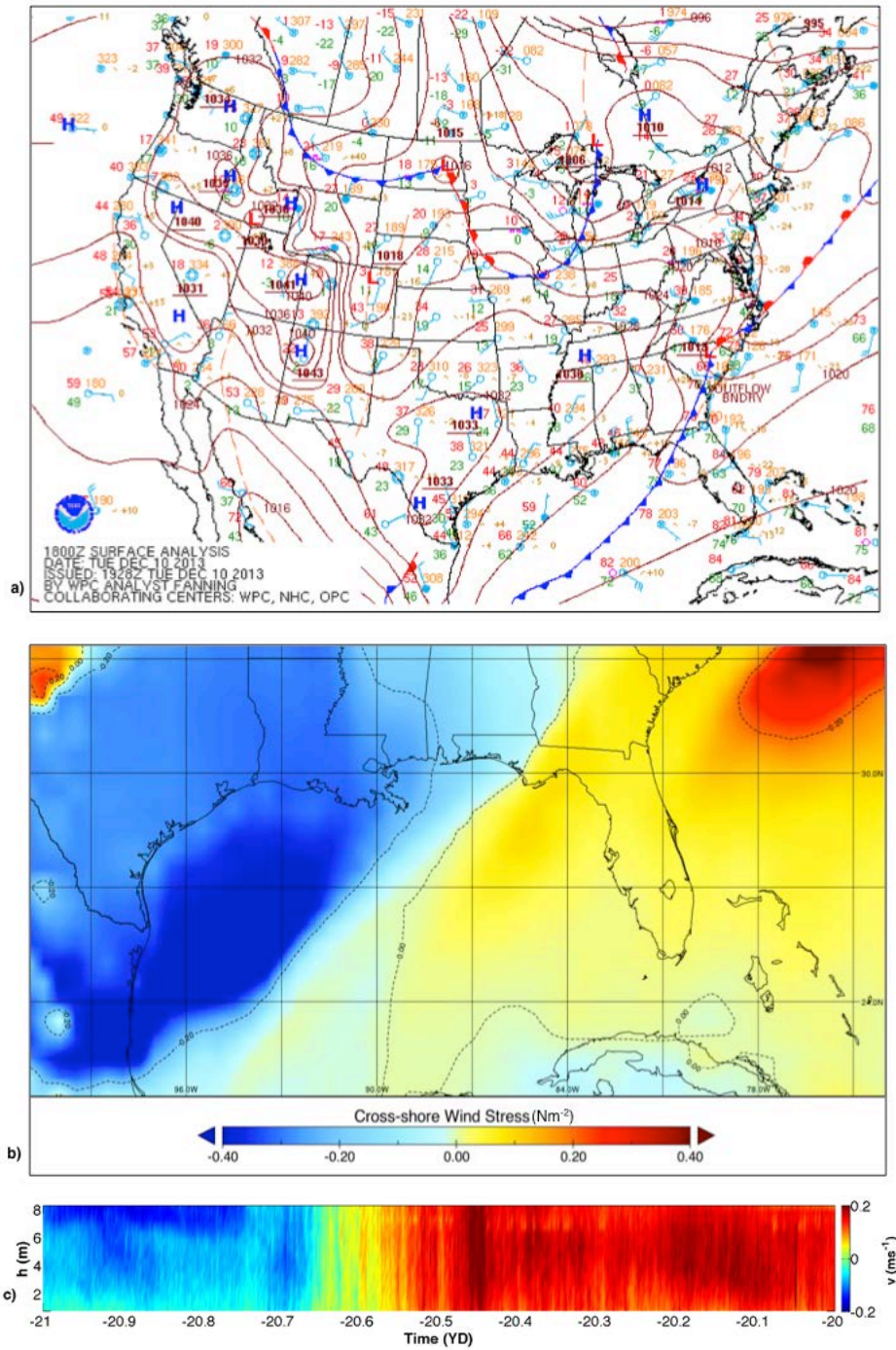
Cold front passage across the northeastern Gulf of Mexico on YD -20 as depicted in a) NOAA surface analysis chart and b) NAVGEM 3 hr averaged cross-shore wind stress field. Blue is wind stress to the south and yellow and red indicate wind stress to the north. c) Response of 2.5 min along-shelf currents measured in 10 m depth at JBP to the passing storm on YD -20. Negative velocities (blue) are to the west and positive velocities (red) are to the east.

Figure 2.4. A Cold Air Outbreak and Ocean Current Response

20

2.   Validation of Model Simulations

NAVGEM cross- and along-shore wind stress are significantly correlated with OB wind stress, r = 0.94 and r = 0.87 (Fig. 2.5 a,b). Depth-averaged HYCOM along-shelf currents are also significantly correlated with observations, r = 0.67 (Fig. 2.5c). For both NAVGEM and OB observations the ratio of the standard deviation of cross-shore wind stress to the standard deviation of along-shore wind stress is >1.5:1, indicating that cross-shore wind stress is the more significant forcing mechanism. The pattern of offshore winds aligning with eastward currents, and onshore winds with westward currents also remains valid in the model output (Fig. 2.5a,c). Therefore, HYCOM simulations forced by NAVGEM are a viable means to investigate the dynamics between cross-shore winds and along-shelf currents along the NEGoMex coastline.
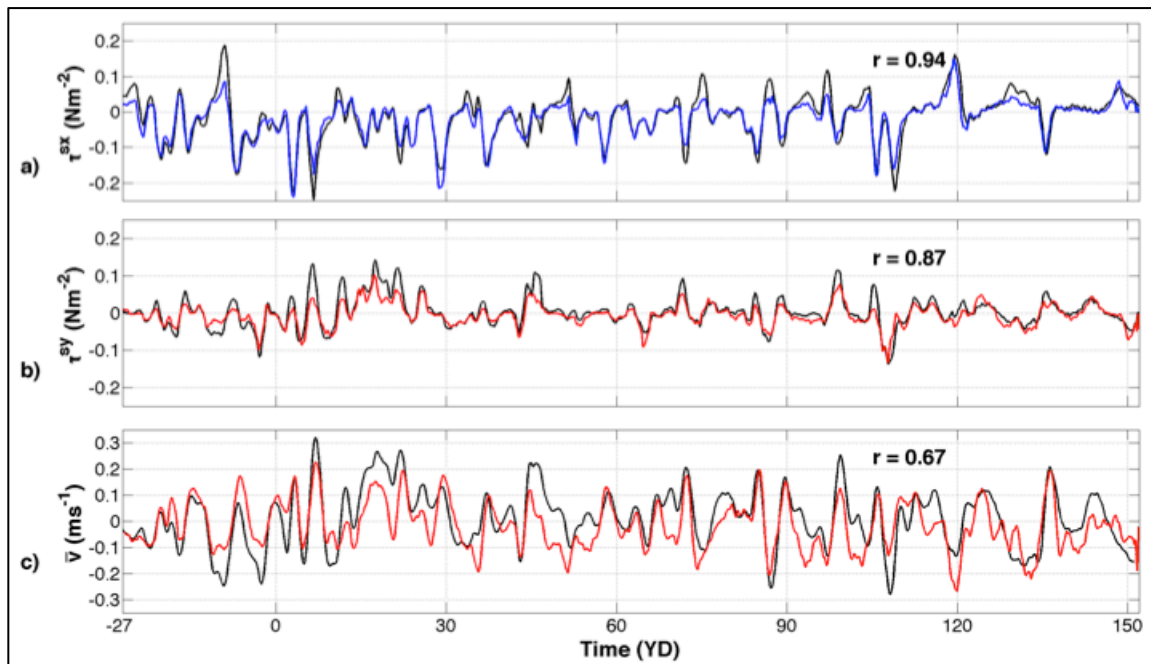
Time series comparisons of 33 hr averaged a) cross-shore and b) alongshore wind stress observations at Orange Beach buoy with NAVGEM wind stress. c) Depth-averaged, subtidal along-shelf currents from JBP and HYCOM. Colored lines are observations and black lines are model data. Winds are positive to the north and east; currents are positive to the east.

Figure 2.5.   Comparison of Wind Stress and Along-shelf Current Simulations with Observations

The forcing mechanisms for the along-shelf flow cannot be evaluated from observations because cross- and along-shelf pressure gradients cannot be determined from a single pressure sensor. Additionally, without measurements of the pressure gradients it is unknown whether observations of wind stress and along-shelf currents yield solutions to Equations (3) and (4) that represent solely the pressure gradients or also include summations of the small terms that were neglected in the formulation of the equations. Therefore, the solutions to Equations (3) and (4) are considered estimates of the pressure gradient terms and cannot be used directly in the momentum balance analysis. The standard deviations of the estimated cross-shelf and along-shelf pressure gradient terms are 6.2E-6 ms^{-2} and 2.7E-6 ms^{-2} respectively, suggesting that the cross-shelf component is more important for the overall momentum balance.

In contrast to the pressure gradient estimates, HYCOM simulations of sea surface elevation and Equations (5) and (6) enable a true evaluation of the roles of pressure gradient and wind stress in forcing along-shelf currents. To determine $\frac{\partial \eta}{\partial y}$ from the model output, an along-shelf length scale of 100 km is selected, consistent in order of magnitude with the distance between nearly steady winds pre- and post CAO (Fernandez-Partaga and Mooers 1975). The estimated along-shelf pressure gradient and ∂y of 100 km yields a $\frac{\partial \eta}{\partial y}$ equal to 2.8E-7 ms^{-2}. The expected cross-shelf extent of the inner shelf, ~30 km, is chosen as the value for ∂x and yields a $\frac{\partial \eta}{\partial x}$ equal to 6.4E-7 ms^{-2} from the estimated cross-shelf pressure gradient. The estimated values of $\frac{\partial \eta}{\partial y}$ and $\frac{\partial \eta}{\partial x}$ are the same order of magnitude as those calculated in 12 m depth at Martha's Vineyard (Fewings and Lentz 2010). Furthermore, the estimated $\frac{\partial \eta}{\partial x}$ is consistent with the expectation of setup and setdown of a few centimeters (1.9 cm over 30 km) caused by wind stress of O(0.1 Nm^{-2}) over a Gulf of Mexico shelf, where the shelf slope is O(10^{-3}) (Lentz and Fewings 2012). Therefore, Equations (5) and (6) are evaluated at the JBP site with model wind stress; depth-averaged along-shelf velocity calculated from current simulations at the surface, 5 m, and 10 m depth layers; modeled η; and 30km and 100 km length scales. Specifically, the $\frac{\partial \eta}{\partial x}$ term is determined by the difference between model simulations of η at JBP and a

point 30 km directly south of JBP. A nearly straight, RC = 440 km, 100 km section of the coast between JBP and Perdido Bay is selected to calculate $\frac{\partial \eta}{\partial y}$ (Fig. 2.1, station 7 to station 2).

3.   Momentum Balance Analysis at John Beasley Park from HYCOM Simulations

The first step in analyzing the momentum balances at the field site is to calculate the standard deviations of each of the modeled terms in Equations (5) and (6). The $\frac{\partial \bar{v}}{\partial t}$ term is eliminated from the along-shelf balance because its standard deviation is an order of magnitude smaller than the standard deviation of the other three terms (Table 2.1). The remaining three terms are retained because they are of the same order of magnitude as the largest term, the bottom stress. All three terms are retained in the cross-shelf balance.

Table 2.1.   Standard Deviations of the Terms in the Momentum Balances at JBP[a]

Standard Deviation	Acceleration (ms^{-2})	Pressure Gradient (ms^{-2})	Coriolis (ms^{-2})	Wind Stress (ms^{-2})	Bottom Stress (ms^{-2})
Cross-Shelf	------	6.9E-6	4.6E-6	4.4E-6	------
Along-Shelf	0.8E-6	1.6E-6	------	2.8E-6	3.1E-6

[a]Standard deviations are of NAVGEM wind and HYCOM oceanographic output. Dashed lines represent terms that are not included in Equation (5) or (6).

In the cross-shelf direction, $g\frac{\partial \eta}{\partial x}$ is comparable in value to the standard deviation of the cross-shelf pressure gradient estimated from observations and produces a nearly equivalent 2.1 cm change in η over 30 km, further validating the employment of HYCOM simulations. $g\frac{\partial \eta}{\partial x}$ is the largest term in the cross-shelf balance and has a high correlation with both $f\bar{v}$ (r = 0.86) and $\frac{\tau^{sx}}{h\rho_0}$ (r = 0.74) (Fig. 2.6a,b). When the $\frac{\tau^{sx}}{h\rho_0}$ and $f\bar{v}$ terms are added together and correlated with $g\frac{\partial \eta}{\partial x}$ the correlation coefficient improves to r

= 0.95 (Fig. 2.6c). An ageostrophic balance, defined as a balance that is not strictly geostrophic because of the importance of wind stress, exists and drives along-shelf currents. The linear regression of $f\bar{v} + \frac{\tau^{sx}}{h\rho_0}$ to $g\frac{\partial\eta}{\partial x}$ has a slope, m, of 1.01, indicating that the balance closes with all three terms.
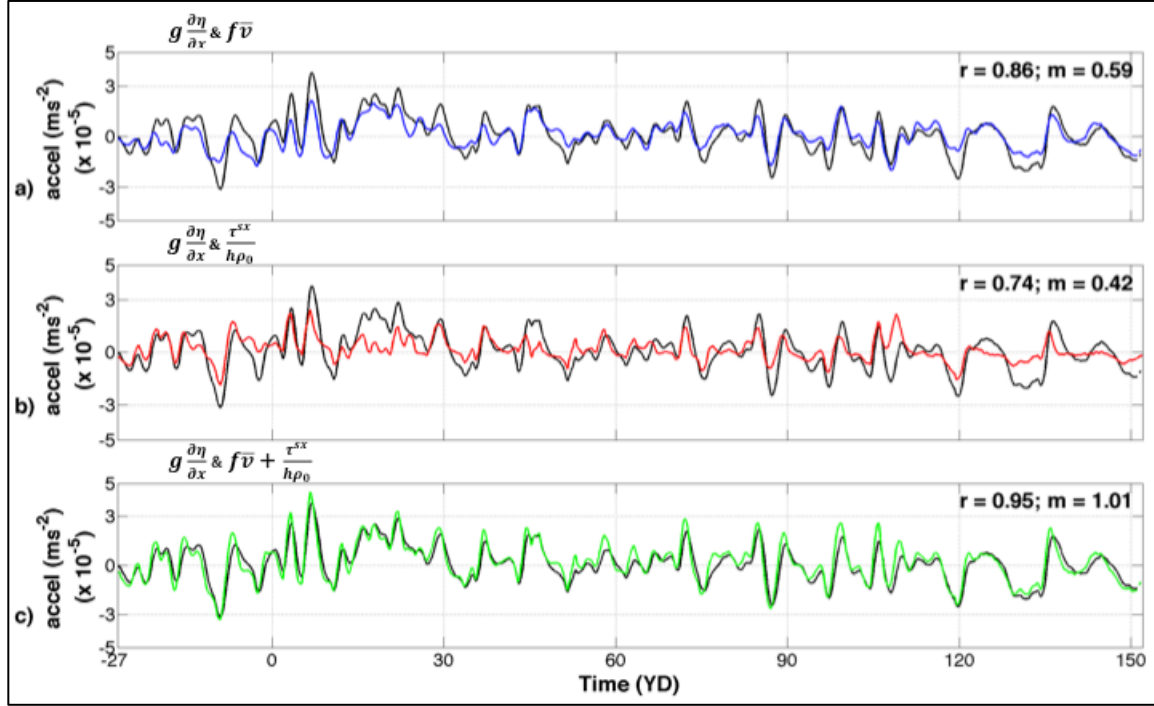
Time series comparisons of the cross-shelf pressure gradient term (black lines) with a) the cross-shelf Coriolis term (blue), b) cross-shore wind stress term (red), and c) the term representing the combination of Coriolis and wind stress (green). All records are from NAVGEM or HYCOM and depict subtidal accelerations.

Figure 2.6.   Cross-shelf Momentum Balance Terms at John Beasley Park

In the along-shelf direction, $-g\frac{\partial\eta}{\partial y}$ is not significantly correlated with either $\frac{b}{h}\bar{v}$ (r = 0.37) or $-\frac{\tau^{sy}}{h\rho_0}$ (r = 0.27; Fig. 2.7a,b). Consequently, $-g\frac{\partial\eta}{\partial y}$ is eliminated from the along-shelf balance. $\frac{\tau^{sy}}{h\rho_0}$ and $\frac{b}{h}\bar{v}$ are significantly correlated, r = 0.90, and the slope of the linear regression of $\frac{b}{h}\bar{v}$ to $\frac{\tau^{sy}}{h\rho_0}$ is 1.23 (Fig. 2.7c).

24
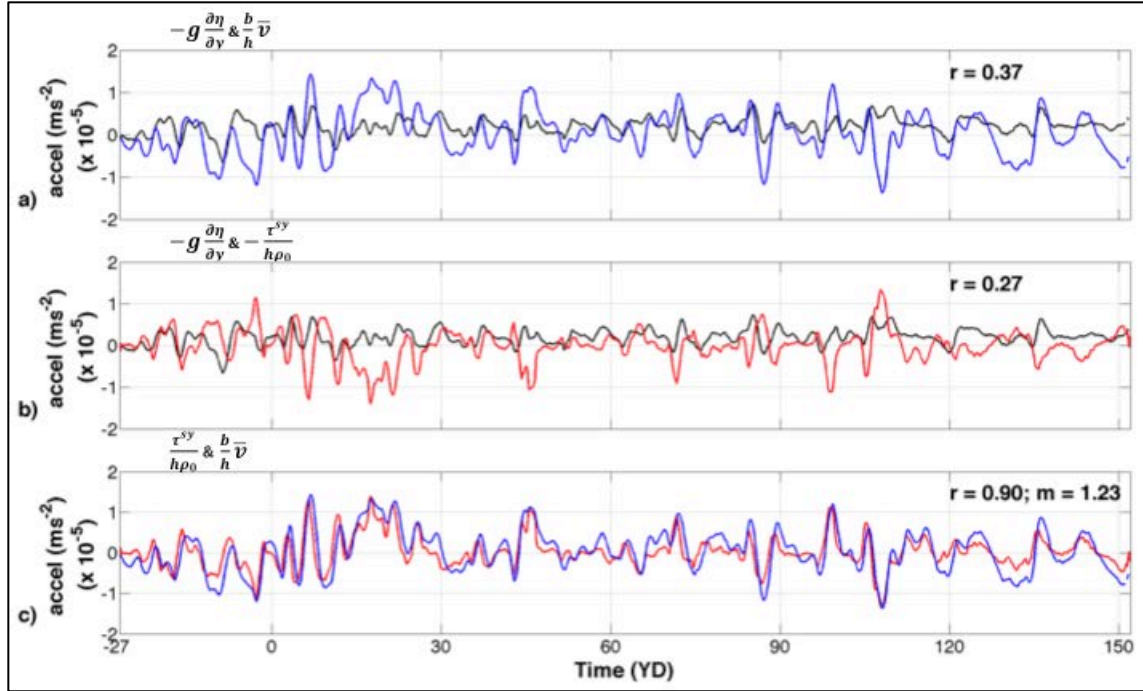
Time series comparisons of the along-shelf pressure gradient term (black lines) with
a) the along-shelf bottom stress (blue), and b) alongshore wind stress (red) terms.
c) Comparison of the along-shelf wind stress and alongshore bottom stress terms. Note
that the vertical scale for Figure 2.7a-c is smaller than the vertical scale of Figure 2.6a-c.
All records are from NAVGEM or HYCOM and depict subtidal accelerations.

Figure 2.7.   Along-shelf Momentum Balance Terms at John Beasley Park

4.   Momentum Balance Analysis along the Curved Coastline

A similar procedure employing HYCOM simulations is followed at all 14 stations
along the coast (Fig. 2.1). Water depth at each station is determined from model
bathymetry and varies from ~10 to 20 m (Fig. 2.1; Table 2.2). Coordinate rotation is
performed individually by station such that the cross-shelf components of wind stress,
current, and $\partial\eta$ are locally perpendicular to the beach. The angle of rotation is positive,
counterclockwise of north for stations 1–6 and negative, clockwise of north for stations
7–14 (Table 2.2). Local RC of the coastline varies at each station and is calculated for
stations 2–13 using the neighboring stations to define the coordinates of the curve.
Stations 6–10 and 12–13 are considered to lie along curved sections of the coast because
the local RC at these points is less than the total RC from stations 1–14, 175 km (Fig. 2.1;
Table 2.2).

25

Table 2.2.   Water Depth, Angle of Rotation, and Local Curvature at
the 14 Coastal Stations

Station Number	h (m)	Angle of rotation (^{o})	Radius of curvature ($\times 10^5$ m)
1	10.0	0.0	------
2	11.0	10.0	2.48
3	11.0	12.5	2.02
4	19.0	4.5	2.88
5	20.0	9.5	7.03
6	20.0	1.5	1.22
7	20.0	-7.5	1.69
8	22.0	-18.5	1.25
9	21.0	-30.5	1.58
10	21.0	-39.0	0.99
11	18.0	-47.0	2.44
12	15.0	-46.0	0.78
13	13.0	-50.0	0.31
14	13.0	-75.0	------

Cross- and along-shore components of wind stress and $\partial\eta$ are interpolated to each station. Instead of prescribing ∂x or ∂y, as was done for the momentum balance at JBP, $\frac{\partial\eta}{\partial x,y}$ are computed from the η values at the four closest model grid points surrounding each station. As measured by standard deviation, τ^{sx} is larger at stations 1–8 than τ^{sy}, but smaller at stations 10–14 (Fig. 2.8a). At station 9 the two components of wind stress are effectively equal. Standard deviations of η increase constantly from 6.8 cm at station 1 to 8.0 cm at station 14, suggesting that variability in η is a function of the curvature at larger sections of coastlines and not a function of local curvature, which can increase or decrease from station to station (Fig. 2.8b; Table 2.2, col. 4).

Though along-shelf currents are expected to be larger offshore, away from the coastal boundary, the magnitude and standard deviation of depth-averaged along-shelf velocities are expected to be similar in 10 m and 20 m water depth. Consequently, the surface, 5 m, and 10 m model velocity layers are again averaged and interpolated to each station, including those in ~20 m water depth. The standard deviation of $\bar{v}$ increases from 0.04 ms^{-1} at station 2 to > 0.06 ms^{-1} between stations 5 and 11 (Fig. 2.8c, red line). The largest standard deviation of $\bar{u}$ at any of the stations is ~0.02 ms^{-1} and is generally $\leq$ .01 ms^{-1} (Fig. 2.8c, blue line). Therefore, terms with $\bar{u}$ remain neglected from Equations (5) and (6) for momentum balance analysis along the coast.
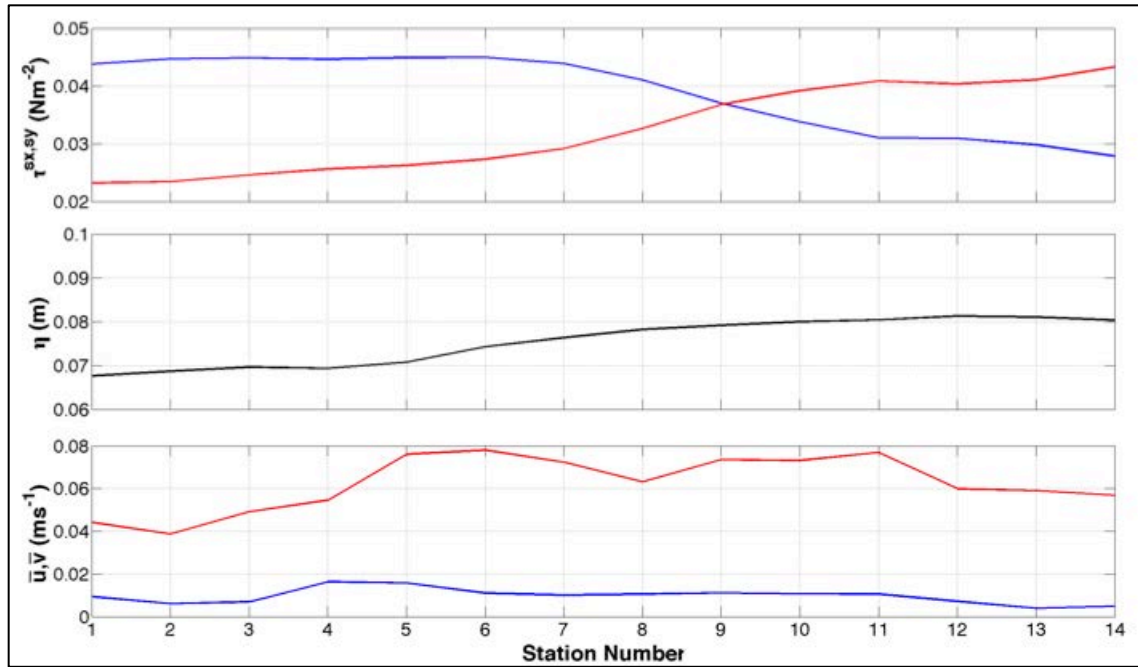
Standard deviations of model output a) wind stress, b) η, and c) depth-averaged currents at the 14 stations along the coast of the NEGoMex. Cross-shore components are blue lines and alongshore components are red lines.

Figure 2.8.   Standard Deviations of Simulated Wind Stress, Sea Surface
                 Elevation, and Currents along the Coast

The standard deviations of the terms in Equations (5) and (6) indicate that the same terms that are important at JBP are important all along the coast (Table 2.3). $g\frac{\partial \eta}{\partial x}$ is

27

greater than $g\frac{\partial\eta}{\partial y}$ at every station (Table 2.3, col. 2 & 3). After $g\frac{\partial\eta}{\partial x}$, $f\bar{v}$ is the next greatest term, on average, across all 14 stations. $\frac{\tau^{sx}}{h\rho_0}$ is the second most important term to the balance at stations 1–3, but then becomes the 3rd most important term behind $g\frac{\partial\eta}{\partial x}$ and $f\bar{v}$ from stations 4–8 (Table 2.3). After station 9, $\frac{\tau^{sx}}{h\rho_0}$ falls behind both $\frac{\tau^{sy}}{h\rho_0}$ and $\frac{b}{h}\bar{v}$ in importance (Table 2.3).

Table 2.3.   Standard Deviations of the Terms in the Momentum
Balance at the Coastal Stations

Station Number	$g\frac{\partial\eta}{\partial x}$ x10^{-6} (ms^{-2})	$g\frac{\partial\eta}{\partial y}$ x10^{-6} (ms^{-2})	$f\bar{v}$ x10^{-6} (ms^{-2})	$\frac{\tau^{sx}}{h\rho_0}$ x10^{-6} (ms^{-2})	$\frac{\tau^{sy}}{h\rho_0}$ x10^{-6} (ms^{-2})	$\frac{b}{h}\bar{v}$ x10^{-6} (ms^{-2})
1	6.2	1.2	3.2	4.3	2.3	2.2
2	5.9	1.5	2.8	4.0	2.1	1.8
3	6.7	1.7	3.6	4.0	2.2	2.2
4	4.6	1.7	4.0	2.3	1.3	1.4
5	6.9	2.1	5.6	2.2	1.3	1.9
6	7.5	1.6	5.7	2.2	1.3	2.0
7	7.4	1.0	5.3	2.1	1.4	1.8
8	6.3	1.2	4.6	1.8	1.4	1.4
9	6.3	1.1	5.4	1.7	1.7	1.7
10	6.1	1.0	5.4	1.6	1.8	1.7
11	6.1	0.8	5.6	1.7	2.2	2.1
12	5.7	1.4	4.4	2.0	2.6	2.0
13	6.6	1.5	4.3	2.2	3.1	2.3
14	4.8	1.8	4.2	2.1	3.2	2.2

In the cross-shelf balance, both $f\bar{v}$ and $\frac{\tau^{sx}}{h\rho_0}$ correlate well with $g\frac{\partial\eta}{\partial x}$ with values typically greater than r = 0.70 (Fig. 2.9a). Correlation improves to r ≥ 0.95 when the two terms are combined (Fig. 2.9a, green stars). An obvious change occurs at station 3 where $\frac{\tau^{sx}}{h\rho_0}$ no longer has a higher correlation with $g\frac{\partial\eta}{\partial x}$ than $f\bar{v}$ (red squares vs. blue diamonds). East of station 3, correlation between $g\frac{\partial\eta}{\partial x}$ and $f\bar{v}$ rapidly improves before fluctuating between r = 0.87 and r = 0.94 from stations 5 to 14 (Fig. 2.9a, blue diamonds). Owing to the application of a 33 hr running average to 3 hr data, a lead or lag of 0–3 hrs in the correlation between $g\frac{\partial\eta}{\partial x}$ and any of the other terms is treated as zero lag/lead. A near-immediate response exists at all stations when all three terms are correlated (Fig. 2.9b, green stars). The cross-shelf momentum balance closes best with slope values near 1 at all stations as the result of an ageostrophic balance between $g\frac{\partial\eta}{\partial x}$, $f\bar{v}$, and $\frac{\tau^{sx}}{h\rho_0}$ (Fig. 2.9c, green stars).
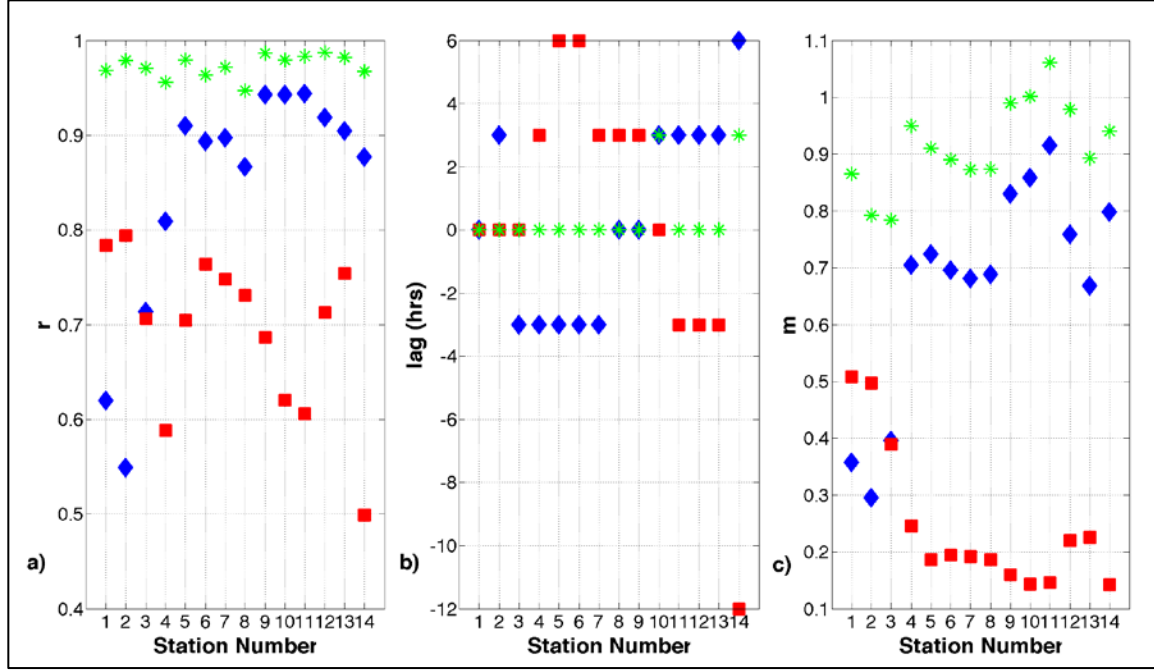
Cross-shelf momentum balance analysis at the 14 coastal stations between $g\frac{\partial \eta}{\partial x}$ and $\frac{\tau^{sx}}{h\rho_0}$ (red squares), $g\frac{\partial \eta}{\partial x}$ and $f\bar{v}$ (blue diamonds), and $g\frac{\partial \eta}{\partial x}$ and $f\bar{v} + \frac{\tau^{sx}}{h\rho_0}$ (green stars). a) Correlation coefficients greater than 0.6 are significantly correlated. b) Lags in hours for the maximum correlation between each set of terms. Positive values indicate that $g\frac{\partial \eta}{\partial x}$ leads the other term(s). c) The slope of the linear regression between each set of terms. The closer m is to 1, the better the balance closes with the terms considered.

Figure 2.9.　　Cross-shelf Momentum Balance along the Coast

In the along-shelf balance, $\frac{\tau^{sy}}{h\rho_0}$ and $\frac{b}{h}\bar{v}$ are significantly correlated with r-values of 0.69 or better at all stations (Fig. 2.10a, black circles). In contrast, $\frac{\tau^{sy}}{h\rho_0}$ and $g\frac{\partial \eta}{\partial y}$ have r-values ≤ 0.60 at 11 of 14 stations, and on average are not significantly correlated along the coastline (Fig. 2.10a, red squares). Combining $g\frac{\partial \eta}{\partial y}$ and $\frac{b}{h}\bar{v}$ provides little improvement on the correlation between $\frac{\tau^{sy}}{h\rho_0}$ and $\frac{b}{h}\bar{v}$ (Fig. 2.10a, green stars). $\frac{\tau^{sy}}{h\rho_0}$ lags $\frac{b}{h}\bar{v}$ by 6–18 hr at every station, which suggests that along-shelf current exists prior to forcing from $\frac{\tau^{sy}}{h\rho_0}$ (Fig. 2.10b, black circles). The momentum balance closes best with $\frac{\tau^{sy}}{h\rho_0}$ and $\frac{b}{h}\bar{v}$ alone at stations 1–12 and with all three terms at stations 13 and 14 (Fig. 2.10c).

30
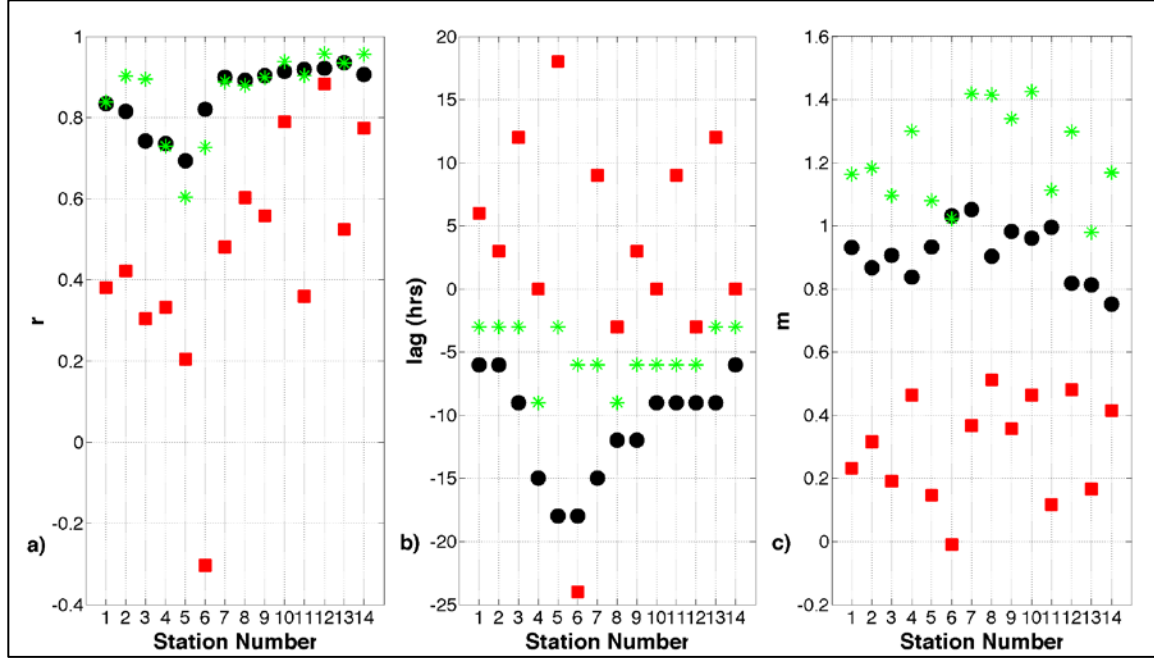
Along-shelf momentum balance analysis at the 14 coastal stations between $\frac{\tau^{sy}}{h\rho_0}$ and $g\frac{\partial \eta}{\partial y}$ (red squares), $\frac{\tau^{sy}}{h\rho_0}$ and $\frac{b}{h}\bar{v}$ (black circles), and $\frac{\tau^{sy}}{h\rho_0}$ and $\frac{b}{h}\bar{v} + g\frac{\partial \eta}{\partial y}$ (green stars). a) Correlation coefficients greater than 0.6 are significantly correlated. b) Lags in hours for the maximum correlation between each set of terms. Positive values indicate that $\frac{\tau^{sy}}{h\rho_0}$ leads the other term(s). c) The slope of the linear regression between each set of terms. The closer m is to 1, the better the balance closes with the terms considered.

Figure 2.10.   Along-shelf Momentum Balance along the Coast

D.   DISCUSSION

During the winter of 2013 to 2014, 21 CAOs passed along the nearly latitudinal NEGoMex coastline. As they move from west to east, inner shelf currents reverse at each of the stations along the coast (Fig. 2.11). As expected close to the coastal boundary, the cross-shelf component of the reversals are slow (<0.10 ms^{-1}; Fig. 2.11a) in comparison to typical along-shelf velocities of ~0.25 ms^{-1} (Fig. 2.11b). Current reversals persist for a couple of days (Fig. 2.2a). Though the relative magnitude of the wind stress components changes with coastline curvature (Fig. 2.8a), the response of the $\bar{v}$ is similar in magnitude, timing, and persistence, regardless of whether the coastline is straight or curved (Fig. 2.11b).
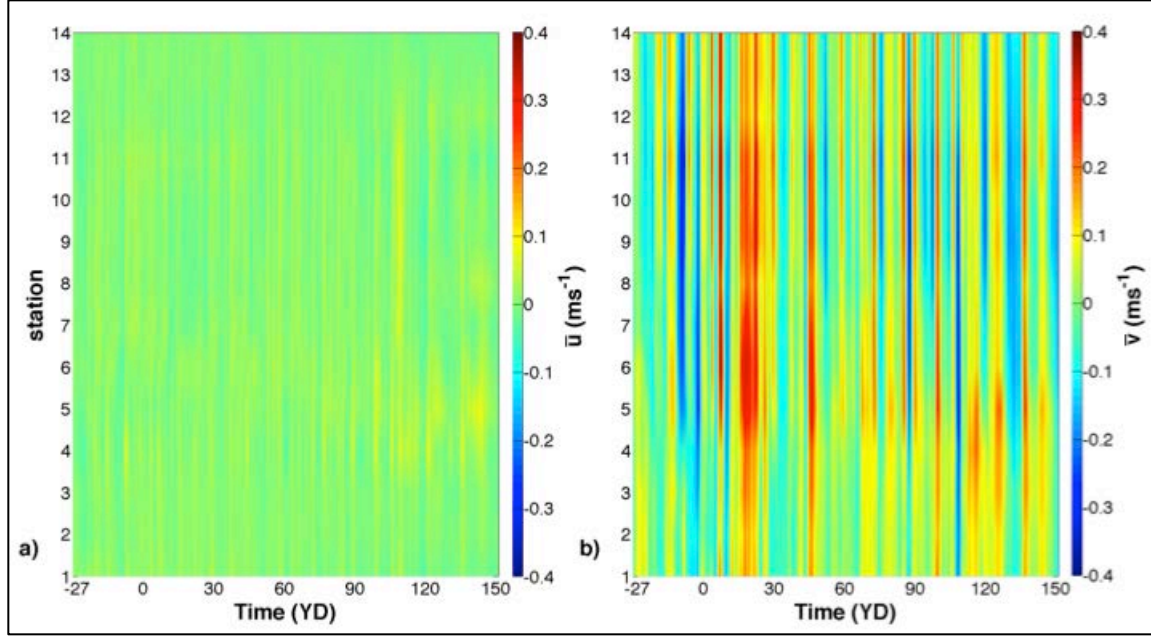
Depth-averaged modeled a) cross-shelf and b) along-shelf currents at all 14 coastal stations. Positive values (red) are offshore for $\bar{u}$ and east alongshore for $\bar{v}$.

Figure 2.11.   Depth-averaged Cross- and Along-shelf Currents along the Coast

1.   The Importance of Cross-shore Wind Stress

The momentum balance analysis demonstrates that $\frac{\tau^{sx}}{h\rho_0}$ and $g\frac{\partial \eta}{\partial x}$ are the forcing mechanisms most responsible for the variability in along-shelf coastal currents along the straight section of the NEGoMex coastline (Fig. 2.6; Fig. 2.9). An ageostrophic cross-shelf balance is also observed in the shallowest part of the inner shelf along the eastern shelf of the United States and along the WFS (Fewings and Lentz 2010; Lentz et al. 1999; Liu and Weisberg 2005). Along stretches of curved coastline, $g\frac{\partial \eta}{\partial x}$ remains the most important term, but $\frac{\tau^{sx}}{h\rho_0}$ diminishes as $\frac{\tau^{sy}}{h\rho_0}$ and $\frac{b}{h}\bar{v}$ become larger and more important to the balance (Table 2.3). An Ekman response to increased τ^{sy} likely contributes to maintaining commensurate values of $g\frac{\partial \eta}{\partial x}$ for stations 10–14 (Table 2.3). The dynamics are then indicative of an Ekman-geostrophic balance discussed by Li and Weisberg (1999a,b) in their numerical model study of the WFS.

32

Linear regression analysis reveals that at each of the 14 stations the cross-shelf and along-shelf balances close best with contribution from the respective component of the wind stress (Fig. 2.9c, green stars; 10c, black circles). However, poor correlations between $\frac{\tau^{sy}}{h\rho_0}$ and $g\frac{\partial\eta}{\partial y}$ (Fig. 2.10a, red squares), and 6–18 hr lags of $\frac{\tau^{sy}}{h\rho_0}$ behind $\frac{b}{h}\bar{v}$ (Fig. 2.10b, black circles) suggest that $\bar{v}$ are not generated by either $\frac{\tau^{sy}}{h\rho_0}$ or $g\frac{\partial\eta}{\partial y}$. In contrast, the cross-shelf ageostrophic balance sets up almost immediately, even along the curved section of coastline (Fig. 2.9b, green stars). Consequently, $\frac{\tau^{sx}}{h\rho_0}$ is instrumental in forcing along-shelf flows throughout the NEGoMex. This result is different than both Fewings and Lentz (2010) and Liu and Weisberg (2005), among others, who have attributed along-shelf currents to $\frac{\tau^{sy}}{h\rho_0}$ and/or $g\frac{\partial\eta}{\partial y}$.

2.   Coastal Pressure Gradients

The standard deviation of the along-shelf pressure gradient force is consistently smaller than the standard deviation of the cross-shelf pressure gradient force at all 14 stations (Table 2.3), reinforcing the idea that $g\frac{\partial\eta}{\partial y}$ do not drive the along-shelf currents depicted in Fig. 2.11b. The difference in magnitude between $g\frac{\partial\eta}{\partial x}$ and $g\frac{\partial\eta}{\partial y}$ is the result of relatively strong cross-shore winds from passing CAO that drive coastal setup pre-front and setdown post-front, of $O(10^{-2}$ m), over long stretches of the coastline, $O(10^5$ m). The wind-driven setup and setdown from the passage of the YD -20 storm is depicted in Figure 2.12. Six hours before frontal passage when winds are from the southwest η increases near the coast (Fig. 2.4b; Fig. 2.12a). Setup is greatest along the curved section of coastline from station 7 to station 14 and within the Pensacola and Choctawhatchee Bays (Fig. 2.12a). Setup within the bays is consistent with setup inside Louisiana bays during the approach of cold fronts (Feng and Li 2010). Along the coast, η changes minimally between stations 1 and 7 (Δy = 120 km), on either side of station 7, and between stations 7 and 14 (Δy = 125 km). η decreases by a similar amount offshore over distances an order of magnitude shorter. When the cold front is at JBP setup occurs along the curved part of the coastline and setdown increases along the straight section of the

33

coast, from station 1 to 7 (Fig. 2.12b). Twelve hours post-front setdown increases to ~0.2 m in the north and eastern portions of the coast. Along the straight section of coastline, between station 1 and Pensacola Bay, η is rising (Fig. 2.12c). Again, $\frac{\partial \eta}{\partial x}$ is greater than $\frac{\partial \eta}{\partial y}$ along both the straight and curved sections of the coast. Therefore, $g\frac{\partial \eta}{\partial x}$ is larger than $g\frac{\partial \eta}{\partial y}$ before and after cold front passage (Fig. 2.12a,c). $g\frac{\partial \eta}{\partial y}$ makes a negligible contribution to the along-shelf currents for all but stations 13 and 14, where the along-shelf wind stress accelerations are the greatest (Fig. 2.10c; Table 2.3).

Along the shelf, standard deviations of η are least at station 1 but increase steadily with coastline curvature to station 12, where η fluctuates the most (Fig. 2.8b). This trend is consistent with the variability of η between straight and curved portions of the WFS during winter cold front passage (Marmorino 1982). Coastal setup and setdown values of ~0.05-0.20 m along the NEGoMex coastline are representative of those observed by Marmorino (1982) along straight sections of the WFS under similar wind stress.
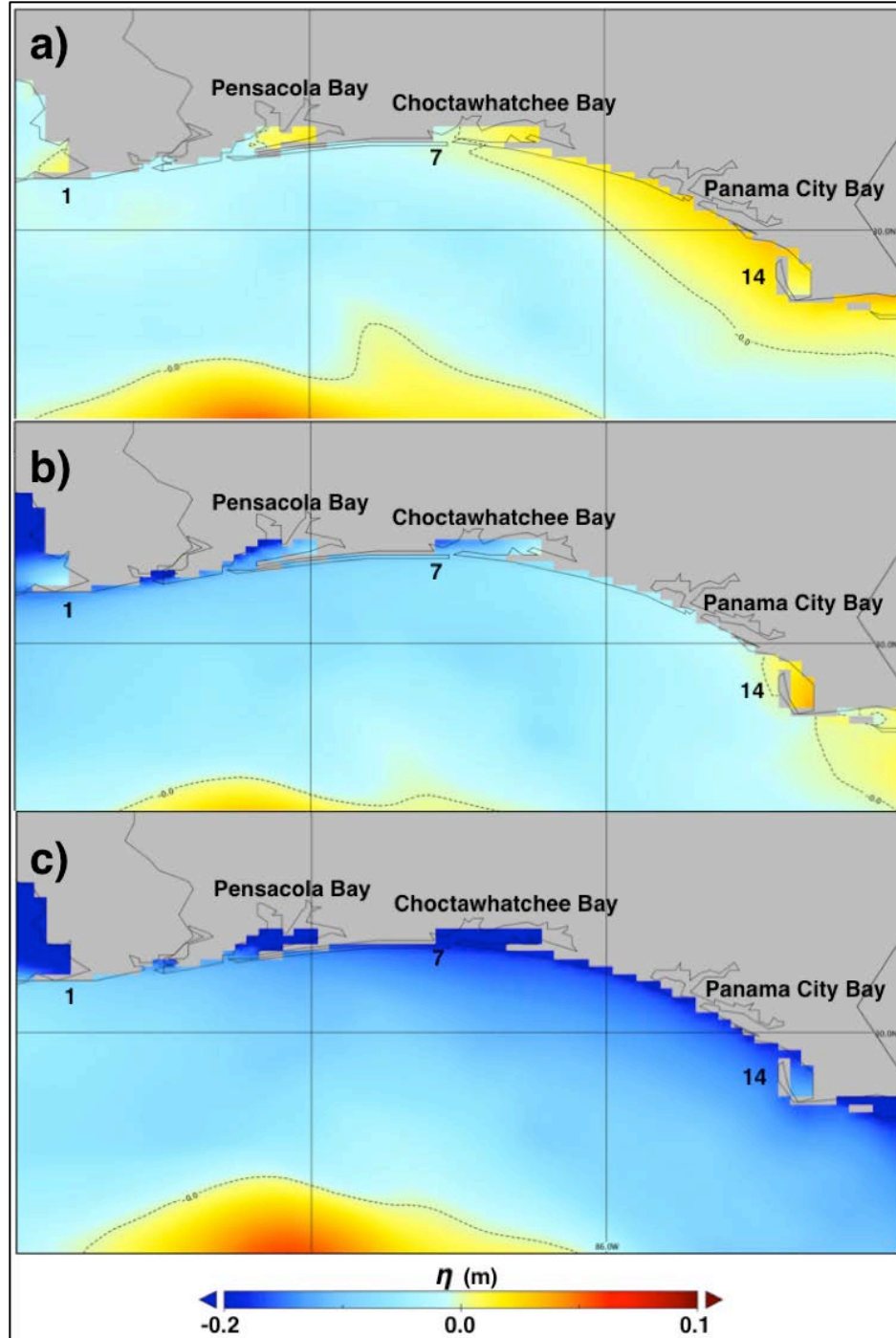
Wind-driven coastal setup and setdown along the NEGoMex a) 6 hours before the front arrives at JBP (station 7), b) as the cold front arrives at JBP, and c) twelve hours after the front passed JBP. Stations 1–7 mark the straight section of the coastline; stations 7–14 the curved portion.

Figure 2.12.   Coastal Setup and Setdown from a Passing Cold Air Outbreak

3. Cold Air Outbreak-induced Current Reversals

The synoptic set up for the YD -20 storm is similar to that of a CAO that produced a current reversal off the coast of Panama City, along the curved portion of the coastline (Huh et al. 1984). In the Panama City reversal on 9 December 1978, a 1033 mb high pressure system that originated over Texas trailed a low pressure system to the east and produced wind stress from the north behind the front (Huh et al. 1984). In response to the arrival of the cold front, a northwestward flowing subsurface current stopped within 1 hour and reversed to southeastward within a day, representing a shift of $O(0.50 \text{ ms}^{-1})$ (Huh et al. 1984). This response is similar in magnitude and timing to the YD -20 current reversal observed at JBP along a nearly straight section of the coastline (Fig. 2.4c). Together passing CAO and coastline curvature explain the generation, timing, and persistence of the current reversals in both locations (Fig. 2.13).
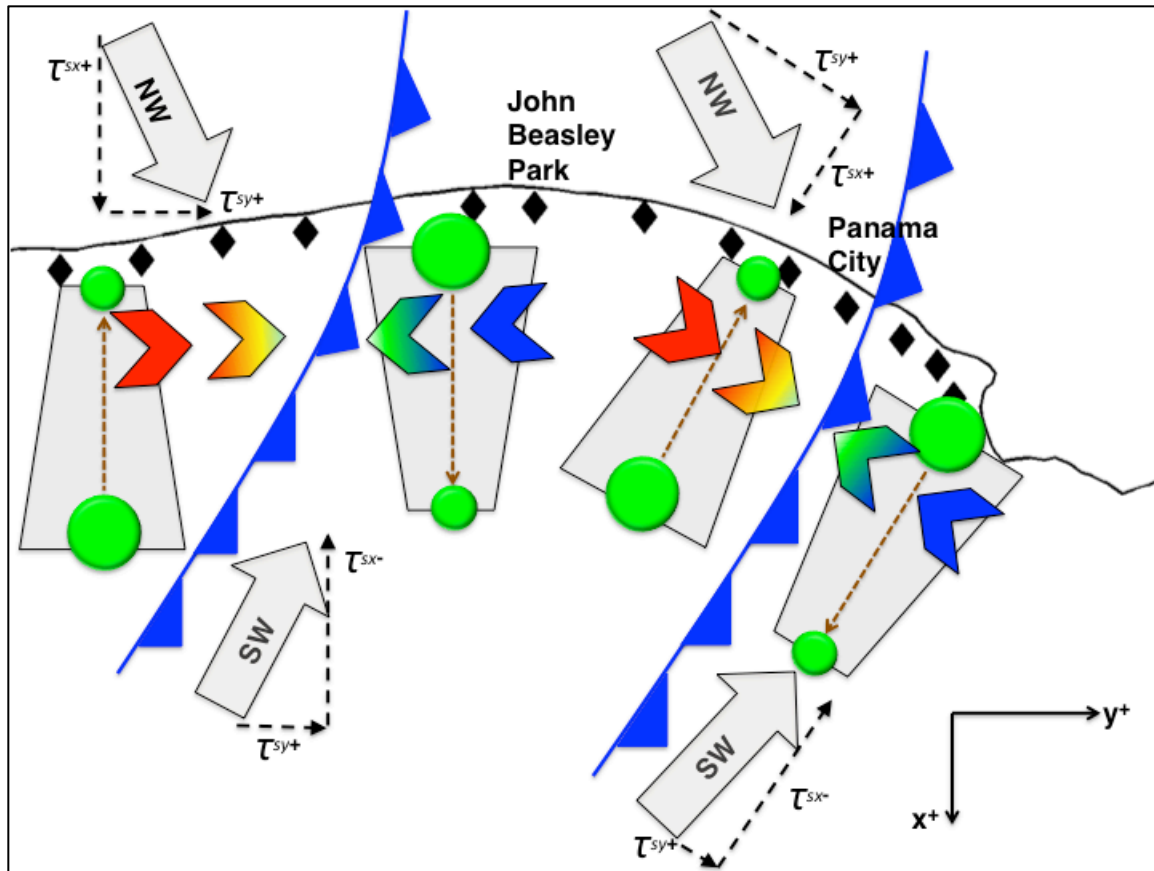
Coastal current reversals driven by cross-shelf winds along the northeastern Gulf of Mexico. Blue cold fronts represent the location of passing storms. Wind stress (gray arrows) is shown in component form (black dashed arrows) driving cross-shelf pressure gradients, $\frac{\partial p}{\partial x}$, (green circles) through wind-driven setup and setdown (gray trapezoids) along the coast. Dashed brown lines represent the direction of the pressure gradient force opposite to the pressure gradient. Current reversals are depicted by horizontal chevrons. Chevrons fade blue to red to show the reversal as the cold front passes and mimic the color of westward and eastward currents in Figure 4c.

Figure 2.13. Conceptual Diagram of Cross-shore Wind Stress Driving Along-shelf Currents

As the CAO approaches NEGoMex wind stress at JBP is from the south, southwest parallel to the front. This drives setup near the coast, as described previously. In response, the cross-shelf pressure gradient force and Coriolis balance to force a westward current, which is portrayed in Figure 13 with blue-green chevrons. The relatively weak alongshore wind stress to the east cannot reverse the current. Once the front passes, north, northwest wind stress perpendicular to the front forces coastal setdown, a near-immediate increase in the pressure gradient offshore (large green circle),

and ageostrophic flow to the east, as indicated with red-green chevrons. The weaker alongshore component of the wind stress now aids in driving the current to the east. It takes 36–48 hours after frontal passage for the atmosphere to return to pre-frontal conditions (DiMego et al. 1976). Meanwhile, the ageostrophic balance is sustained by northerly wind stress and the current persists in the eastward direction for a day or more. Feng and Li (2010) report that bay flushing events in response to passing cold fronts also have a similar duration of 25 – 45 hrs.

As the front continues east to Panama City standard deviations of τ^{sx} are smaller than τ^{sy}. Pre-front southerly wind stress again causes an ageostrophic balance and along-shelf current flows to the northwest. Post-front, increased positive alongshore wind stress creates an Ekman response to the right of τ^{sy} that aids the reduced τ^{sx} in driving coastal setdown, and currents reverse to the southeast. Again, persistence of the atmospheric conditions post-front, namely northerly wind stress, explains the duration of the current reversal. The combined, post-front ageostrophic and Ekman-geostrophic balance along the curved portion of the coastline includes the cross-shelf pressure gradient, Coriolis, both components of wind stress, and bottom stress and is supported by results from Li and Weisberg's (1999a,b) numerical modeling study of the WFS.

E.   CONCLUSION

Inner shelf, depth-averaged, along-shelf currents forced by passing cold air outbreaks are examined along straight and curved sections of coastline in the northeastern Gulf of Mexico with both field observations and a numerical model simulation. In response to these extratropical storms, subtidal along-shelf currents oscillate ~weekly throughout the winter and spring in the northeastern Gulf of Mexico. When the currents reverse, westward flow slows from ~-0.20 ms^{-1} or more to 0 ms^{-1} within an hour and continues to accelerate to ~0.20 ms^{-1} eastward within a day or less. Eastward along-shelf flow can persist for ~2 days. The forcing mechanisms that drive along-shelf coastal currents, as well as the generation, timing, and persistence of the current reversals, are important for understanding material transport along this coast.

The cross-shelf pressure gradient force is consistently the most variable, and therefore the most important, term in the subtidal, time-variant, depth-averaged momentum balance. For straight sections of the coastline this term is balanced by the combination of cross-shelf wind stress and Coriolis resulting in ageostrophic along-shelf currents. Along curved sections of the coast, variability in the alongshore wind stress is greater than variability in the cross-shore wind stress, but the cross-shore wind stress is still important for generating coastal setup and setdown. Along-shelf currents in these areas are a response to an ageostrophic balance pre-front and an additional contribution from an Ekman-geostrophic balance post-front. The along-shelf pressure gradient force is consistently of little importance to the momentum balance, and only helps close the balance where the coastline is nearly longitudinal.

Cross-shore wind stress drives along-shelf currents in the inner shelf of the northeastern Gulf of Mexico during the winter. The change between onshore and offshore wind stress pre- and post-cold air outbreak explains the timing of observed rapid along-shelf current reversals at both straight and curved sections of the coastline. The current is sustained by persistent cross-shore winds pre- and post-front. This differs from inner shelf studies in the northern Gulf of Mexico and east coast of the United States that attribute along-shelf flows to along-shelf forcing (Fewings and Lentz 2010; Liu and Weisberg 2005; Lentz et al. 1999; Crout 1983). Due to the frequency of cold air outbreaks (3-10 days), cross-shore winds regularly accelerate along-shelf currents. These findings are not attributed to a unique event or unusual set of circumstances. Additionally, because it takes the atmosphere and ocean a day or two to return to pre-storm conditions, cross-shore winds can influence the inner shelf for days at a time and are a substantial part of the wind-driven coastal circulation. Owing to a similar relative orientation between coastline and winter storm trajectories, it is expected that the dynamics described herein explain wintertime circulation, including along-shelf coastal current reversals, in the inner shelf of the northwestern Gulf of Mexico as well.

THIS PAGE INTENTIONALLY LEFT BLANK

III. NATURAL COASTAL BARRIERS TO SURFACE MATERIAL TRANSPORT IN THE NORTHERN GULF OF MEXICO

This chapter has been submitted to *Continental Shelf Research* for publication with minor formatting changes. As the main author of this work, I made the major contributions to the research and writing. Co-authors include Jamie MacMahan,[a] Ad Reniers,[b] Tamay M. Özgökmen,[c] Kate Woodall,[a] and Brian Haus.[c]

A. INTRODUCTION

The Deepwater Horizon (DwH) oil spill demonstrated a need to further understand the physical processes that are important for the transport of oil and other floating materials at the surface of the ocean. This understanding is critical within the shallower nearshore portion of the ocean, defined as the region that encompasses both the surf zone, where waves break, and the inner shelf, seaward of the surf zone, where the surface and bottom boundary layers overlap (Lentz and Fewings 2012). The nearshore acts as a conduit between the deep ocean and the coastal environment and is the "last mile" for oil to transit before potentially washing ashore. This region is home to many marine species and has tremendous ecological and economic importance.

As oil approached the Florida Panhandle in early June of 2010, nearshore surface oil forecasts available from the National Oceanic and Atmospheric Administration's Office (NOAA) of Response and Restoration relied upon satellite imagery and ocean circulation models that produced large "uncertainty boundaries" for where the oil would wash ashore (NOAA 2010; Mariano et al. 2011). Additionally, oil location estimates were often inconsistent between forecasts (Mariano et al. 2011). The spreading of surface material, particularly at the submesoscale (1-10 km), is not predicted well by circulation models (Poje et al. 2014; Gildor et al. 2009). Surface dispersion prediction is further challenged in the nearshore by anisotropic conditions that prevent accurate parameterization of a bulk eddy diffusivity term (LaCasce 2008; Swenson and Niller

---

[a] Naval Postgraduate School.

[b] Delft University of Technology, Delft, the Netherlands.

[c] Rosentiel School of Marine and Atmospheric Science, University of Miami.

1996; LaCasce and Ohlmann 2003; Haza et al. 2008; Romero et al. 2013). Increased knowledge of small-scale, nearshore processes will improve oil forecasting capabilities and cause uncertainty boundaries to shrink. Further study of nearshore circulation is necessary to improve the response to future oil spills (Dzwonkowski et al. 2014).

Inner shelf circulation studies suggest that waves and winds are the principal forcing mechanisms for cross-shelf surface transport (Lentz and Fewings 2012 among others). Outside the surf zone, when winds are absent, wave forcing from Stokes drift and undertow balance each other and there is no net transport to the coast (Lentz et al. 2008). Onshore winds create onshore flow near the surface and offshore flow at depth (Fewings et al. 2008; Hendrickson and MacMahan 2009). Offshore winds and undertow from swell are additive and result in strong offshore flow at the surface with decreasing offshore flow (Fewings et al. 2008) or onshore flow (Lentz and Fewings 2012) at depth. In the inner shelf, cross-shore winds are more effective at driving cross-shelf transport than alongshore winds when the water column is well mixed (Lentz and Fewings 2012; Dzwonkowski et al. 2011).

The water column velocity observations to support these and other inner shelf circulation and transport studies are commonly collected using bottom-mounted Acoustic Doppler Current Profilers (ADCP). Many of these studies eliminate the observations from the near-surface ADCP collection bins to avoid poor data caused by acoustic side lobe errors at the surface. Velocity data from the highest remaining bin(s), which are often >2 m below the actual ocean surface, are then extrapolated to create the surface layer. This process is followed at the Martha's Vineyard Coastal Observatory (Fewings et al. 2008; Lentz et al. 2008) and near the mouth of Mobile Bay, where an ADCP is maintained as part of the Fisheries Oceanography in Coastal Alabama program (Dzwonkowski et al. 2014; Dzwonkowski et al. 2011). A substantial loss of data occurs in shallow waters when near-surface observations are eliminated (Dzwonkowski et al. 2014). Oil is a buoyant material that was transported at the surface during DwH (Kourafalou and Androulidakis 2013). For the study of oil transport across the nearshore, deleting the upper ADCP bins leads to the loss of the most important velocity layer of the water column.

Drifters that are designed to float only in the top meter of the water column observe the Lagrangian surface flow well (Schmidt et al. 2003; MacMahan et al. 2009; Poulain 1999). Drifter paths can be used to describe the speed, direction, and temporal and spatial variability of circulation patterns, as was done during the Surface Current and Lagrangian Drift Program (SCULP) in the northern Gulf of Mexico (Ohlmann and Niiler 2005). Drifters can be deployed in groups to observe how material disperses, or mixes, in both the surf zone (Brown et al. 2009; MacMahan et al. 2010; Spydell et al. 2007) and inner shelf (Ohlmann et al. 2012). Calculations of relative dispersion, D^2, the spreading between pairs of drifters, from GPS positions reveal the temporal and spatial scale of the physical mechanisms that contribute to transport, but do not attribute the mixing to a specific forcing mechanism (LaCasce 2008; LaCasce and Ohlmann 2003).

Schroeder et al. (2012) investigate submesoscale dispersion with drifters at the front associated with a coastal current generated by river outflow in the North-Western Mediterranean Sea. Coastal currents commonly develop in the far field region of river plumes when riverine water emerges into the inner shelf (Horner-Devine et al. 2015). The coastal current associated with river discharge is often a shallow surface feature (Chapman and Lentz 1994) that can deepen with down-welling winds (Haus et al. 2003), and persist for tens of kilometers before mixing with the ambient oceanic water (Garvine 1987; Yankovsky et al. 2000). Density fronts form as boundaries between the brackish riverine water and oceanic water (Garvine 1987). Surface material converges and slows at river plume boundaries (Garvine 1974a; Garvine and Monk 1974). A numerical modeling study of the Perdido Bay Estuary plume, in the northern Gulf of Mexico, demonstrates that wind forces both the location of small-scale plume in the inner shelf and the density difference between the plume and oceanic water (Xia et al. 2011). Based on the work described above, it is expected that buoyant plumes, and the coastal currents they produce, will alter surface material transport in the nearshore. However, an understanding of the spatial and temporal influence of wind-driven buoyant river plumes on nearshore surface material transport from field observations is missing.

It is hypothesized that coastal barriers will form and prevent oil and other offshore surface materials from washing ashore in regions adjacent to a river inlet when the wind-

driven plume parallels the beach as a coastal current. The Surfzone and Coastal Oil Pathways Experiment (SCOPE) deployed both an ADCP and drifters in the inner shelf adjacent to Destin Inlet, Florida to test this hypothesis (Section 2). Observations of drifter pathways and dispersion during the approach and passage of a synoptic storm are used to evaluate the effectiveness of the plume as a barrier to surface material transport under light and variable winds (<2 m/s) and moderate winds (>2 m/s) from the east, north, and south (Section 3). Additionally, a method that takes advantage of low wave conditions is used to retain near-surface ADCP velocity data. ADCP surface pathlines are compared with drifter trajectories to assess long-term monitoring of surface current trends with ADCP. Coastal barrier formation, frequency, persistence, and extent westward, away from the inlet are explored in Section 4. SCOPE results are applied to the conditions that occurred at the beach adjacent to Destin Inlet during DwH.

B.   MATERIALS AND METHODS

1.   Field Experiment

SCOPE was conducted in December 2013 at John Beasley Park (JBP) in Destin, FL. along an open, nearly east-west stretch of the NGoMex on a barrier island that was impacted by the Deepwater Horizon oil spill (Fig. 3.1). A cross-shore array of 4 RBR bottom Conductivity, Temperature, and Depth (CTD) sensors were deployed 50 m, 100 m, 200 m, and 500 m from the beach in 1.5 m, 2.0 m, 3.0 m, and 10.0 m water depths. At the end of the array, collocated with the 10 m CTD, a bottom-mounted, upward-looking ADCP was deployed to collect pressure and along- (u) and cross-shore (v) velocity in 0.5 m bins continuously at 1 Hz for ~ 2 weeks (white diamond, Fig. 3.1).
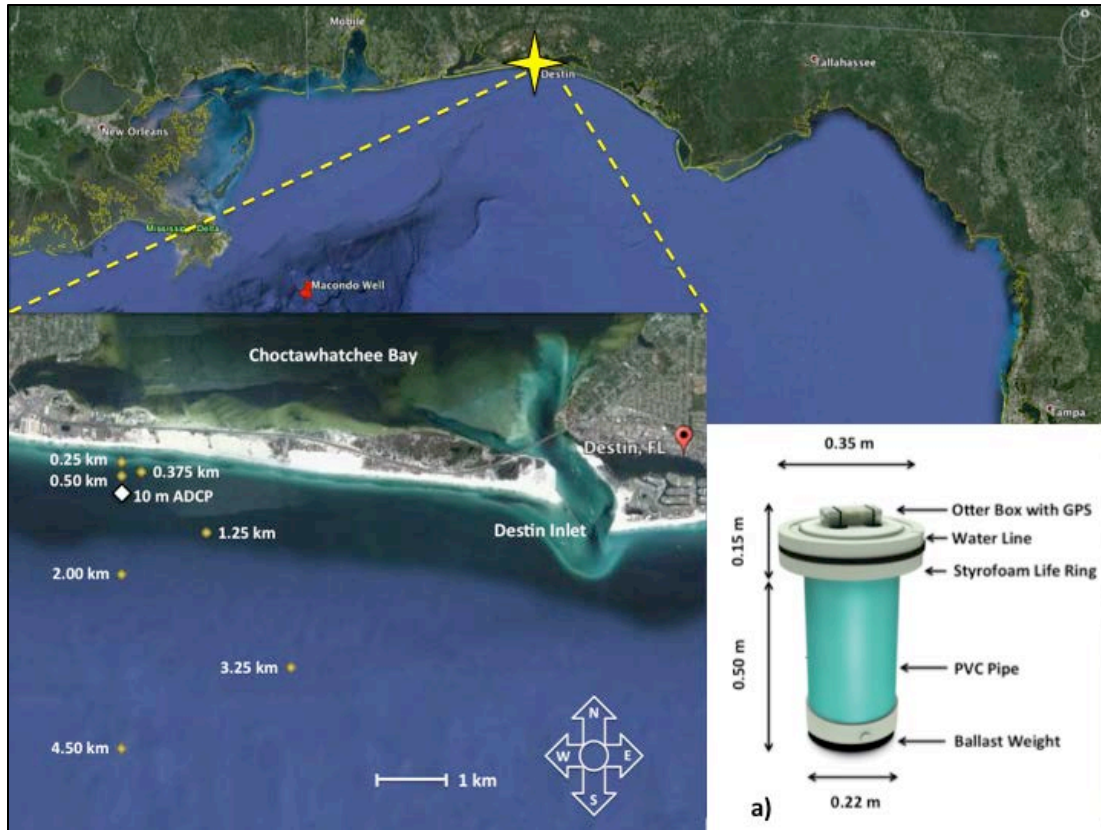
Google Maps image of the northern Gulf of Mexico with SCOPE site indicated with a yellow star and the Macondo Well with a red marker to the southwest. Inner shelf drifter deployment locations are depicted by gold dots on zoom in of Destin Inlet and adjoining beach. 10 m ADCP is annotated with a white diamond and offset farther south for clarity. Inset a) SCOPE drifter with SPOT hand-held GPS affixed on top, inside an Otter Box.

Figure 3.1.   SCOPE Location and Instrumentation

Along- and cross-shore wind velocities were obtained using sonic anemometers mounted on a 10 m high mobile wind tower deployed in the backshore at JBP. Wind velocities were also obtained from NOAA Pensacola station located 75 km to the west of JBP (Fig. 3.2a,b). Note that JBP and NOAA Pensacola wind velocities are correlated ($r=0.72$ and 0.92 for u and v) at the 95% confidence level. The wind velocities were low-pass filtered using a 12-hour cut-off frequency. The Pensacola winds are used to represent the mesoscale forcing, O(100 km). The JBP winds are used to determine local forcing effects with the nearby ADCP.

45
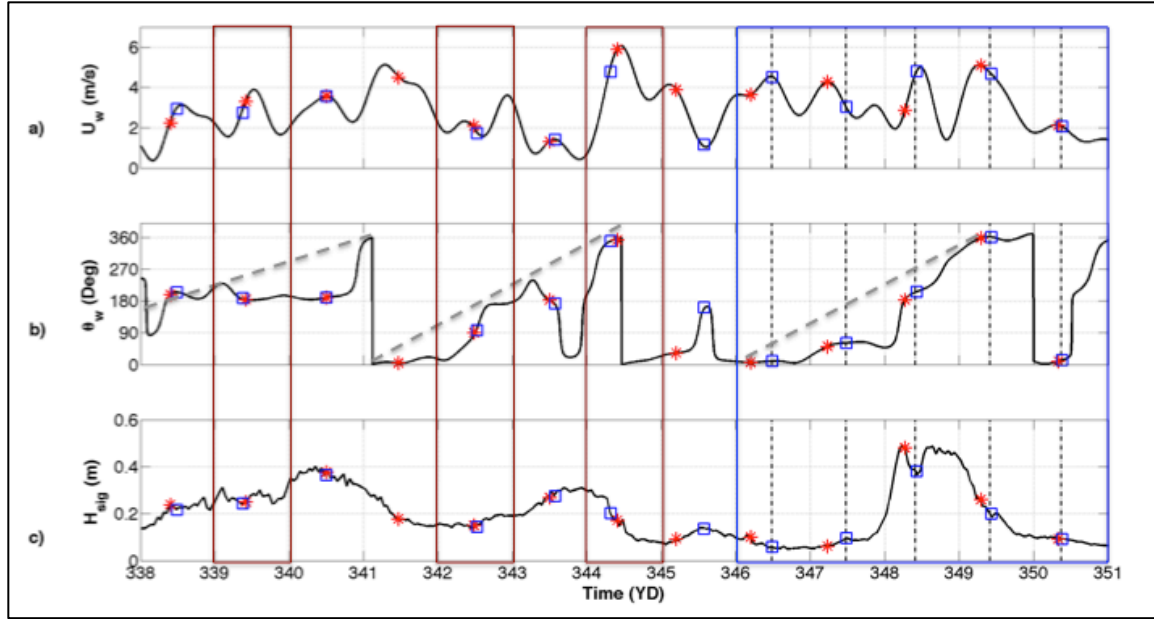
a) SCOPE 6-min sampled wind speed and b) direction from the NOAA station Pensacola, FL. (#8729840) low-pass filtered using a 12-hour cut-off frequency. Gray dashed lines highlight the rotation of winds with the passage of winter storms. c) SCOPE hourly significant wave height. Brown boxes highlight drifter deployment in Destin Inlet on YD 339, 342, and 344. Blue box highlights the synoptic storm of interest and period of triplet drifter deployments. Black dashed lines indicate CTD cast times from 0.50 km drifter deployment station. Small blue squares represent the time that all drifters are in the water for each deployment. Red stars annotate low tide. No drifters were deployed on YD 341.

Figure 3.2.   Field Observations of Wind and Waves

A series of low-pressure extratropical cyclones O(100 km) with moderate winds of magnitude O (5 m/s) that rotate 360° over 3–5 day periods passed from west to east during the experiment (gray lines, Fig. 3.2b). These synoptic storms are common during winter on the Florida Panhandle (Gutierrez de Velasco and Winant 1996). Cross-shore winds (northerly and southerly) were most frequently observed at JBP (Fig. 3.3a). The strongest winds were from the north. In comparison, alongshore winds were less frequent but did, at times, blow with equal strength, O(5 m/s), from the east, northeast. Winds from the west were rarely observed.

46
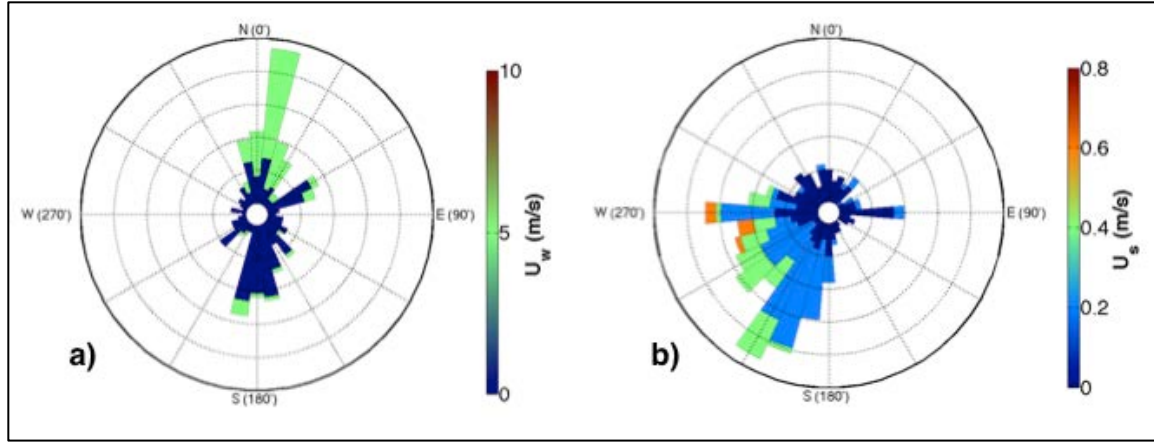
SCOPE a) hourly JBP wind (from) and b) hourly surface current (to) histograms depicting the most frequent direction and magnitude of the wind and wind and plume-driven surface flow (<1 m) as observed by the 10 m ADCP.

Figure 3.3.   Observed Wind and Currents during SCOPE

Wave heights were calculated from ADCP pressure observations and linear wave theory. The synoptic storm spanning YearDay (YD) 346–350 produced the largest waves observed during SCOPE, H_{sig} = ~0.5 m (Fig. 3.2c). Throughout the experiment, the largest waves occurred when winds were from the south, ahead of frontal passage, which is consistent with the observations of Huh et al. (1984). When the winds were from any other direction the coastline limited fetch and prevented the waves from building (Fig. 3.2,b,c). The tides were primarily diurnal with 30 cm range. Low tide shifted ~0.75 hours later each day.

During SCOPE, the Choctawhatchee River had a discharge of O(150 m^3/s), which is near the annual minimum. The river exited Destin Inlet into the inner shelf 7 km east of the experiment site with the ebb tide as a buoyant plume at the surface. Plumes are dynamically classified by the Kelvin Number,

$$K = \frac{\gamma L}{c/f},$$ (1)

in which the across-shore length scale of the discharge, γL, is defined as slenderness, γ, times the alongshore length of the discharge, L, and is compared to the baroclinic Rossby radius, c/f, defined by the internal wave phase speed, c, divided by the Coriolis parameter, f, (Garvine 1995). Destin inlet has a depth of 7 m and width of 450 m (Valle-

Levinson et al. 2015). Setting γL equal to the width of the inlet, assuming the initial depth of the plume is equal to the depth of the inlet, and using a representative observed density difference between the plume and ambient shelf water of 1.5 kg/m^3, Eq. 1 yields a Kelvin Number of 0.11. Because K $<<$ 1, the Choctawhatchee Bay plume is classified as a small-scale plume (Garvine 1995). The Choctawhatchee Bay plume is one of a series of small-scale wind-driven plumes in the NGoMex, which includes the Mobile Bay plume (Gelfenbaum and Stumpf 1993) and Perdido Bay plume (Xia et al. 2011).

2. SCOPE Drifters

More than 350 drifters were deployed from the beach, in the inlet, and in the inner shelf to observe surface (<1 m) transport during SCOPE. Drifters deployed from the inner shelf on YD 346–350 targeted the passage of the storm. They were deployed in the morning after ebb tide and after the plume had progressed out of the inlet and into the inner shelf (Fig. 3.2 blue squares and red stars). Each of the 5 deployments consisted of the release of 15 drifters from 7 stations in the inner shelf (Fig. 3.1 yellow dots). At each of the 7 stations, a CTD was lowered through the water column coincident with drifter release to determine if the drifters were deployed in plume or oceanic water. Twelve drifters were launched in a triangular triplet configuration with O(1-10 m) initial separation distance at four cross-shore locations 0.25 km to 4.50 km from the beach. The three remaining drifters were released at distances of 0.375 km, 1.25 km, and 3.25 km diagonally from the beach. The 75 drifters deployed over the 5-day period created a total of 525 original pairs of drifters for dispersion analysis with various initial separation distances. One of the locations of the drifter releases corresponded with the location of the ADCP for additional comparisons.

SPOT GPSs housed in small waterproof boxes were affixed to the top of the drifter (inset a, Fig. 3.1). The GPS transmitted their positions every 5 minutes for near real-time tracking and data archiving. The drifters were designed to be able to withstand and operate in the breaking waves of the surf zone while having a small surface expression to mitigate the effects of direct wind forcing, known as windage. Additionally, the drifters were made to be stackable and man-portable so that they could be deployed

and re-deployed using small boats in multiple locations and in large quantities, which is important for Lagrangian statistics (LaCasce 2008). The surface foam ring provided the appropriate buoyancy. A 5 lbs. weight was mounted on the bottom to create a lower center of mass, increase stability, and reduce surfing when drifters cross into the surf zone (Schmidt et al. 2003; MacMahan et al. 2009). Open holes at the top and bottom of the drifter allow water to free fill within the drifters and they submerge to just below the waterproof box. This creates a ~5 cm surface expression and minimal (<7%) cross-sectional area that is exposed to wind while still enabling satellite communication.

During a qualitative experiment in Monterey Bay, SCOPE drifters and surf-zone drifters, designed by MacMahan et al. (2009), behaved similarly in the inner shelf. The surf-zone drifter is estimated to have a measurement error due to windage of ~0.01 m/s surface velocity per 1 m/s of wind velocity (MacMahan et al. 2010). SCOPE drifters have a smaller exposed cross-sectional area than surf-zone drifters because they do not have a 0.7 m antenna mast, but the same error due to windage is conservatively assumed.

3.   ADCP Measurements of the Near Surface Velocity Data

Eulerian measurements of the surface flow can be obtained using an ADCP, but surface bin observations often have errors due to acoustic side lobe effects. A typical approach to remove these errors is to discard the upper two bins below the mean sea level (MSL). Depending on bin size, removal of two bins may leave only subsurface (>1 m below MSL) velocity data available for analysis, which can be different than the surface (<1 m below MSL) flow. To remove the effects of side lobe errors from the ADCP data, MSL and H_{sig} are computed every 15 minutes using linear wave theory. The 15-minute quality control window represents stationarity for MSL and sea-swell waves. Velocity measurements above the MSL minus $H_{sig}/2$, referred to as the wave trough level, are discarded. Owing to the small tidal range and small waves during SCOPE, this technique removes 1 bin below the MSL (0-0.5 m below MSL). The two bins immediately below the wave trough level (0.5-1.5 m below MSL) are depth-averaged and used here to represent the near-surface flow. Note that this technique also removes Stokes drift from the observations. ADCP velocities are hourly-averaged by bin from 0.5 meters above the

bottom to the surface and presented in Figure 3.4. Only observations below the wave trough level are kept. The red dashed lines at 8.5 m in Figure 3.4 depict a clear delineation of surface versus subsurface flow structures, which often differ in magnitude and direction.
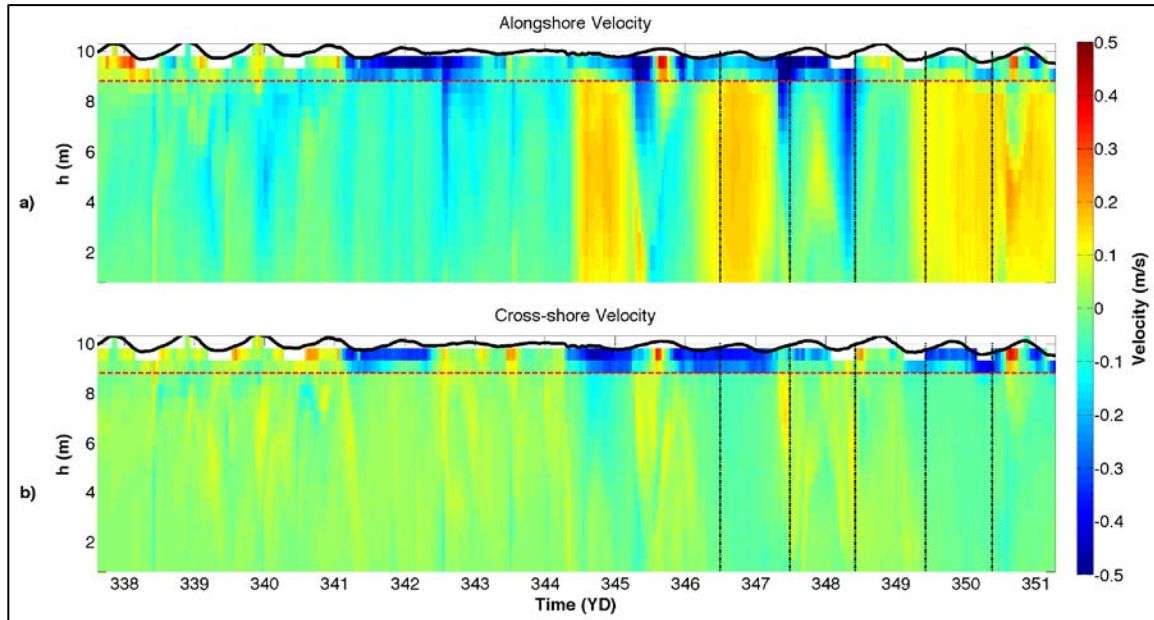
a) ADCP alongshore, u, and b) cross-shore, v, hourly velocity profiles with depth for the 10 m ADCP. Positive velocities (red) are eastward and northward (onshore); negative velocities (blue) are westward and southward (offshore) in m/s. Black solid lines are the sea surface. Red dashed lines separate the surface layer from the subsurface layer. Vertical black dashed lines indicate CTD cast times from the 0.50 km drifter deployment station.

Figure 3.4.   Observed Along-shore and Cross-shore Currents in 10 m Water Depth

C.   RESULTS

1.   The River Plume in the Inner Shelf and Coastal Current Formation

Drifters were deployed within the inlet during ebb tide to track the location of the plume as it emerges into the nearshore. Drifters were deployed on YD 339, 342, and 344 corresponding to days with light and variable, becoming southerly winds; weak winds with an easterly component; and moderate northerly winds (brown boxes Fig. 3.2). On YD 339 (blue lines Fig. 3.5), after the drifters exit the inlet, some move east and are

pulled back into the inlet during the flood tide. Most proceed directly offshore before moving westward and onshore in an arcing pattern. These drifters trace a mid-field bulge and a far field coastal current down-coast, indicative of a prototypical plume (Horner-Devine et al. 2015). Drifters deployed during easterly winds on YD 342 do not extend as far offshore as the drifters on YD 339. These drifters do not show mid-field bulge development, and instead indicate that the outflow immediately turns west and forms a coastal current (red lines Fig. 3.5). This result is consistent with Fong and Geyer (2002), who find that an external mechanism, like wind, increases the freshwater input to the coastal current. When this occurs the coastal current deepens, widens, and increases in both speed and extent down the coast, as will be shown in Section 3.3. The enhanced coastal current is hereafter referred to as a coastal jet. Under moderate northerly winds on YD 344, the drifters emerge and continue directly offshore and neither the bulge, nor the coastal current forms (green lines Fig. 3.5.).
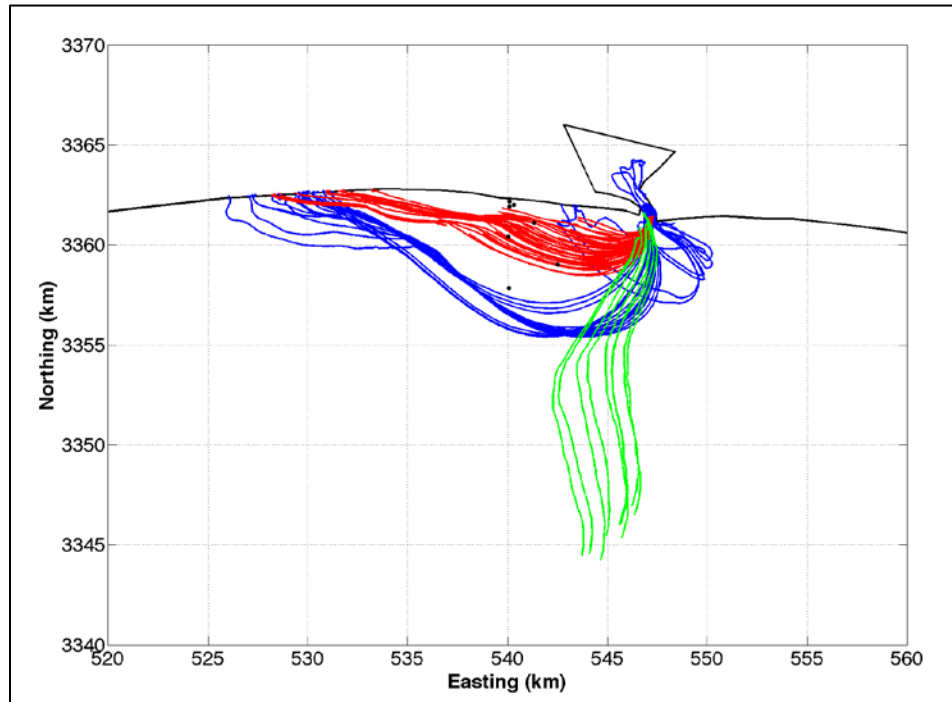
Drifters deployed in the inlet on YD 339 (blue), YD 342 (red) and YD 344 (green) trace the plume into the inner shelf. Black circles near 540E are drifter deployment stations for YD 346–350 inner shelf drifter deployments.

Figure 3.5.   Inlet Drifter Deployments

51

2. Wind and Plume-driven Surface Flow

The wind- and plume-driven surface flow in response to the passage of a synoptic storm is observed with both drifters and near-surface ADCP observations. To make comparisons between Lagrangian and Eulerian observations, pathlines (X, Y) are calculated by integrating the hourly (dt) subsurface and surface ADCP velocities (u and v) for the first 30 hours (T) corresponding to drifter releases, where

$$X = \int_0^T u\,dt \tag{2}$$

and

$$Y = \int_0^T v\,dt. \tag{3}$$

The pathlines are compared to the trajectories of drifters deployed at the location of the ADCP (0.5 km offshore) on YD 346–350. The one exception is YD 348 when moderate southerly winds caused the drifters deployed at the 0.5 km station to beach quickly. On this day, drifter trajectories farther offshore (3.25 km) are used instead (Fig. 3.1).

Comparison of subsurface and surface pathlines during storm passage reveals that the surface current flows in different directions than the subsurface current (Fig. 3.6a,b). The subsurface current alternates exclusively northwest to southeast (Fig. 3.6a). In contrast, the surface current flows offshore to the south and west (Fig. 3.6b). Subsurface pathlines and drifter trajectories compare poorly in both direction and extent (Fig. 3.6a,b). Surface pathlines qualitatively match, but do not exactly replicate drifter trajectories due to inhomogeneities in the flow away from the ADCP (Fig. 3.6a,b). Windage and remaining side lobe errors may also contribute to discrepancies between surface pathlines and drifter trajectories. However, the agreement between surface pathlines and drifter trajectories, as compared to the poor agreement between the subsurface pathlines and drifter trajectories, highlights the importance of retaining ADCP observations in as many of the near-surface bins as possible. Near-surface bin retention is particularly important in the presence of a buoyant plume that provides stratification to the water column.
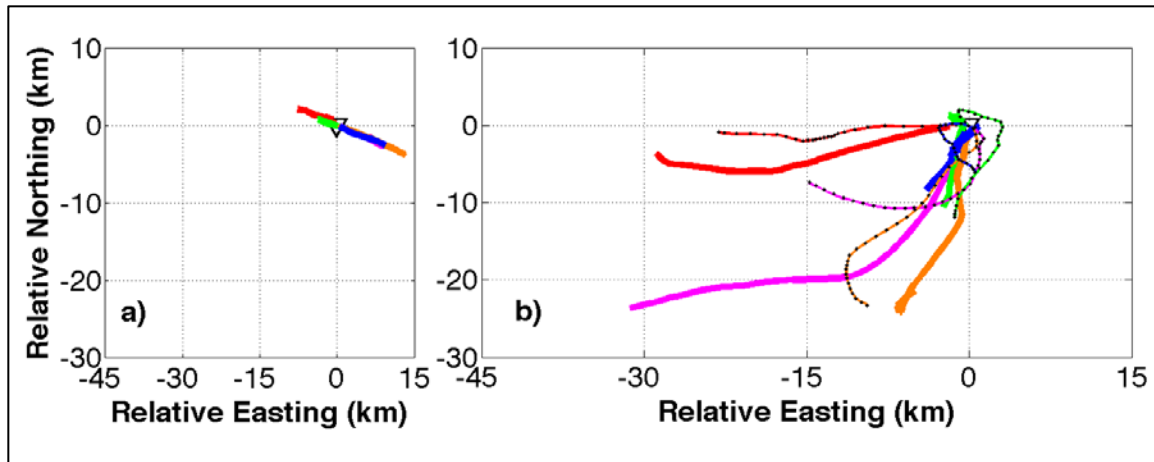
a) 30-hour pathlines of hourly depth-averaged ADCP subsurface (>1 m) current compared with b) 30-hour pathlines of ADCP surface current (<1 m) (solid lines) and drifters (solid lines with black dots) for YD 346 (magenta), YD 347 (red), YD 348 (green), YD 349 (orange), and YD 350 (blue). Note the YD 348 drifter originates from the 3.25 km deployment station because the drifters at the 0.50 km station washed ashore within 7 hours. The location of the ADCP is represented by a black triangle at 0E, 0N.

Figure 3.6.   Surface and Subsurface Pathlines

Surface pathlines and drifters trajectories both indicate that the surface flow responds to rotary winds associated with the synoptic storm. Surface currents and drifters flow south with northerly winds early on YD 346 and all day on YD 349 (Fig. 3.2b; Fig. 3.6b magenta and orange lines). Easterly winds on YD 347 drive a coastal jet (Fig. 3.2b; Fig. 3.6b red lines). The atmospheric front passes the experiment site on YD 348 and forces onshore surface flow early in the day followed by a rapid reversal to the south, offshore (Fig. 3.2b; Fig. 3.6b green lines). On YD 350 winds decrease to <2 m/s and become variable (Fig. 3.2a,b). Light and variable winds lead to a small surface current that shifts between southwest and northeast until it flows consistently southwest, likely the result of the radial expansion of the plume bulge once it extends over the ADCP (Fig. 3.6b blue solid line).

The similarity between drifter trajectories and surface pathlines around the passage of a synoptic storm suggests that ADCP surface flow observations are useful for describing long term surface transport at this location. For all of SCOPE, near-surface ADCP velocities are significantly correlated at the 95% confidence level with the JBP wind speeds in the alongshore and cross-shore direction resulting in r-squared values, R^2,

of 0.52 and 0.76. The associated linear slopes are 0.068 and 0.037, which represent the ratio of ADCP surface velocity to wind velocity. These ratios are higher than the theoretical ratio of 0.01 as estimated by the inner shelf vertical flow structure model of Lentz et al. (2008) using environmental conditions observed during SCOPE (see the appendix at the end of this chapter for more details). The high alongshore and cross-shore slope values are hypothesized to be an effect of the plume passing the ADCP as a coastal current, similar to the along- and cross-shelf flow ~10 km behind the leading edge of the coastal current associated with Chesapeake Bay observed by Lentz et al. (2003). Hourly ADCP observations throughout SCOPE show that the surface layer flows predominantly to the southwest away from the beach, but frequently flows quickly along the coast (Fig. 3.3b). Fast westward flow is indicative of the presence of coastal currents and jets and supports the idea that the surface flows are both wind- and plume-driven.

3.   SCOPE Drifter Fate

Throughout SCOPE, 355 drifters were deployed into the wind- and plume-driven surface layer. Salinity measurements from CTD casts during triplet deployments on YD 346–350 are used to categorize drifters deployed into the plume as plume drifters and drifters deployed outside the plume as oceanic drifters (Fig. 3.7a). CTD casts reveal that the freshest water is offshore and near the surface on YD 346. On YD 347, brackish water exists at all drifter deployment stations to a depth of 10 m, but is freshest at the coast. The three inshore stations remain fresh on YD 348. The water column is vertically mixed to an oceanic salinity across all four stations on YD 349 and YD 350, indicating that the plume has not reached the cross-shore array. The presence of coastal currents are inferred from wind and bottom salinity records to categorize drifters deployed within 300 m of the beach on YD 338, 343, 345, and 347 as plume drifters (Fig. 3.7b; Fig. 3.2a,b). Bottom salinity records show a cross-shore gradient of brackish water during predominantly southerly winds prior to YD 341. After YD 341, drops in salinity across the bottom CTDs appear to be related to the deepening and widening of the coastal current (Fig. 3.7b). All drifters deployed in the inlet are grouped as plume drifters.
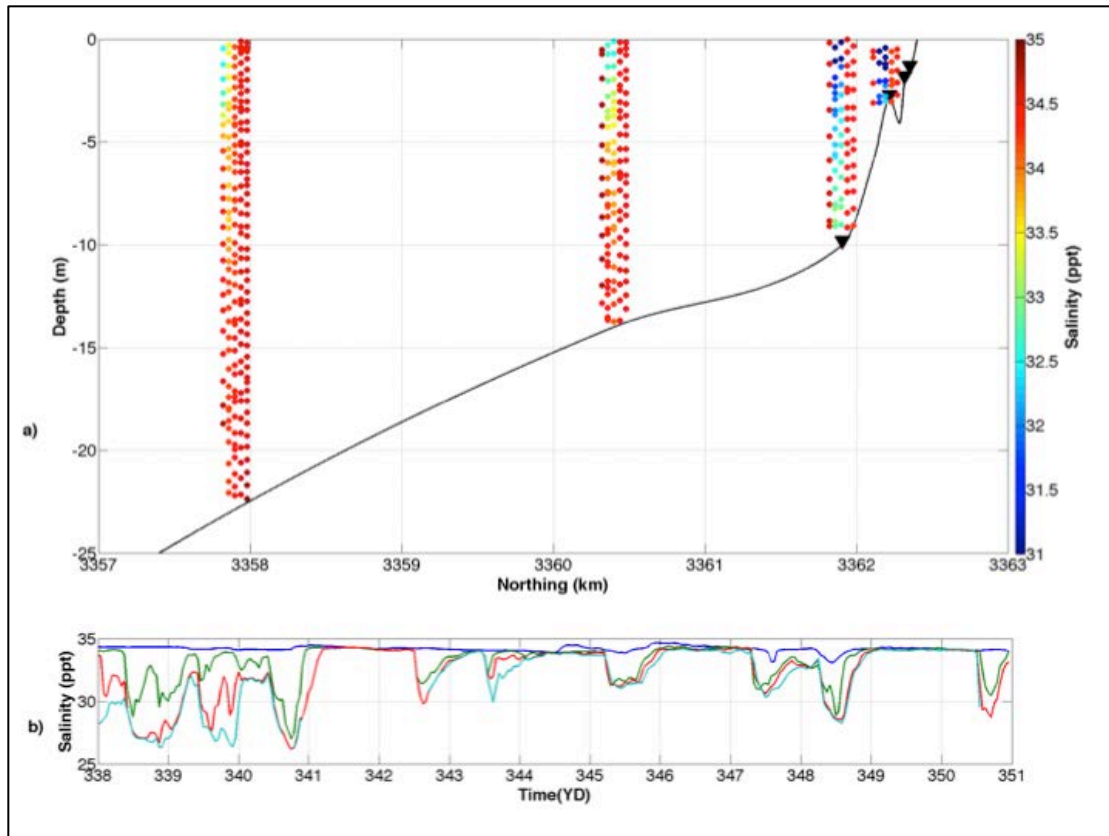
a) Salinity observations with depth at the four cross-shore drifter deployment stations. CTD up-casts on YD 346 through YD 350 are depicted chronologically from left to right at each station. Black triangles near 3362N and shoreward represent the bottom CTD. b) Time series of salinity observations at the 10 m (blue), 3 m (green), 2 m (red), and 1.5 m (light blue) bottom CTD.

Figure 3.7.   SCOPE Salinity Observations

Of the 216 plume drifters more than 90% beach within 27 km west of the inlet (Fig. 3.8a). The remaining ~10% move offshore to the south or southwest. Plume drifter paths reflect the net Eulerian surface flow alongshore and offshore observed by the ADCP (Fig. 3b). In contrast, oceanic drifters often travel far offshore in circuitous paths before returning towards the coast (Fig. 3.8b). When they do return to the coast these drifters often experience a deflection west within 27 km of the inlet (520 km E). 62 of the 139 oceanic drifters go directly to the beach during a period of sustained southerly winds from YD 338 through YD 340, at the beginning of the experiment (red lines, Fig. 3.8b).
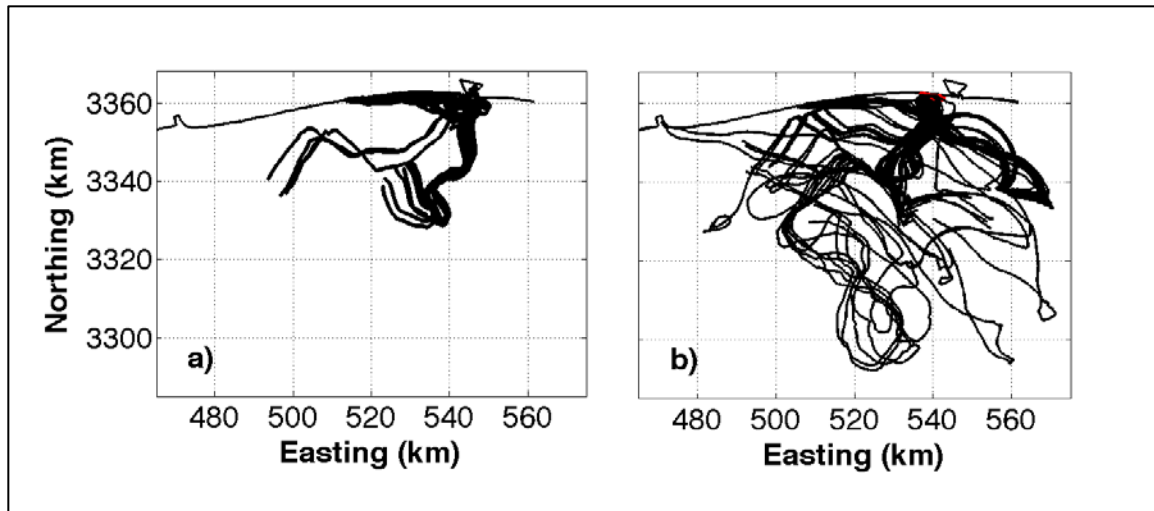
Paths of drifters deployed a) into the plume and b) into oceanic water. Red lines in 8b represent oceanic drifters deployed close to the beach during sustained southerly winds that go directly onshore.

Figure 3.8.   Plume and Oceanic Drifter Paths

Following a similar technique to that employed by Spydell et al. (2007) and Brown et al. (2009), 5-minute position differences for 322 drifter records are used to construct probability density functions (PDF) of drifter displacements. Oceanic drifters (33) associated with 2 extended inner shelf deployments form the majority of the long circuitous offshore paths in Fig. 3.8 and are left out of this analysis. A PDF is made for each of three categories of drifters, similar to those depicted in Figure 3.8: plume, oceanic deployed during sustained southerly winds on YD 338 and YD 340, and oceanic deployed under rotary winds surrounding the synoptic storm, YD 346–350 (Fig. 3.9). The PDFs provide the most common five-minute magnitude and direction of movement of the drifters. The most common displacement for plume drifters is west along the coast with no preference in movement onshore or offshore (Fig. 3.9a). Oceanic drifters deployed near the beach during periods of sustained southerly winds also move west but are consistently forced north toward the beach (Fig. 3.9b). The oceanic drifters deployed around the storm transit primarily to the south or have a strong westward component to their cross-shore movement (Fig. 3.9c). The PDFs represent the net Lagrangian transport across the nearshore and complement the ADCP surface histogram (Fig. 3b) by showing

that the plume forces surface material primarily west, parallel and south, away from the beach.
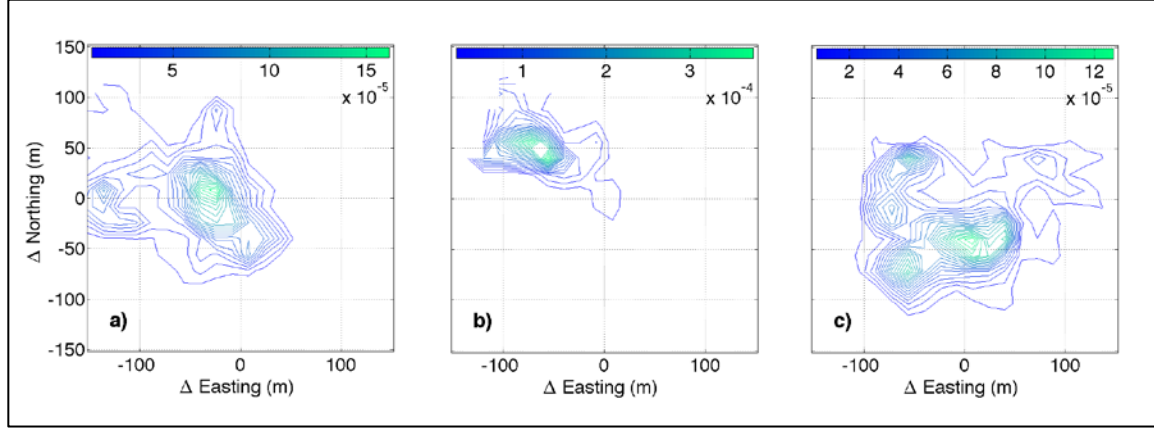
Probability density functions for the most common displacement of a) plume drifters, b) oceanic drifters under sustained southerly winds, and c) oceanic drifters deployed during the approach and passage of a synoptic storm. Green contours are the most frequent displacement. Contours are normalized by both the number of drifters and the number of displacement bins.

Figure 3.9.   Drifter Displacement Probability Density Functions

a.   *Drifter Dispersion Associated with the Passage of Synoptic Storms*

The continuous divergence and convergence of drifters over time is calculated statistically as the relative dispersion between pairs of drifters using the equation of variance (Spydell et al. 2007),

$$D_{ii}^2(t, s_0) = < [s_i(t) - s_{0i}]^2 > - < [s_i(t) - s_{0i}] >^2, \qquad (4)$$

where s_{0i} is the initial pair separation distance at the time of deployment, $s_i(t)$ is the time-dependent pair separation distance, and angle brackets denote ensemble average. Eq. 4 is only valid for multiple pairs of drifters, and the calculation ceases when a drifter beaches or is recovered.

Inner shelf drifter deployments on YD 346–350 created 105 pairs daily for dispersion calculations. Plotting D^2 on a log-log scale allows determination of the power

law between D^2 and t. On each day dispersion grows approximately as $D^2 \sim t^2$, indicative of local, ballistic dispersion caused by constant shear (LaCasce 2008; Schroeder et al. 2012) (Fig. 3.10a). Though the observation of ballistic dispersion is consistent with the literature, there are large variations in growth between deployments and within each deployment. To attribute these variations to specific underlying physical processes, dispersion with respect to time is evaluated linearly to examine the finer details of D^2 growth (Fig. 3.10b). Of note, D^2 for YD 348 is calculated using only 4 drifters instead of 15 drifters because the 11 drifters deployed closest to shore beached quickly under the influence of southerly winds.
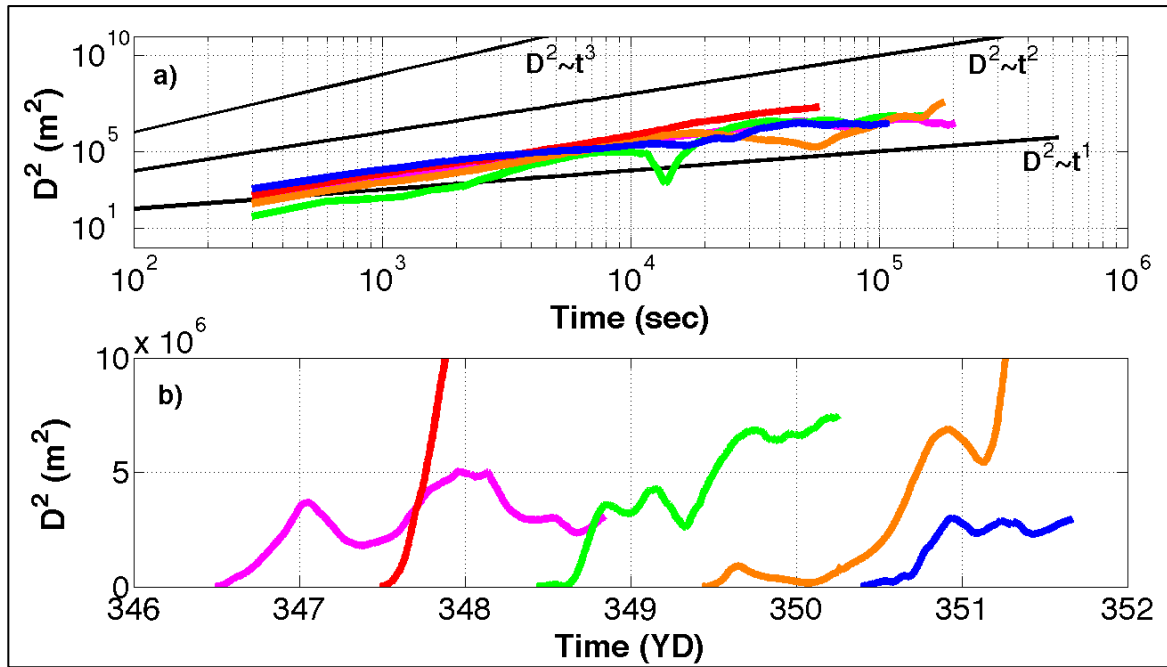
a) Loglog plot of relative dispersion (D^2) for triplet deployments on YD 346 (magenta), YD 347 (red), YD 348 (green), YD 349 (orange), and YD 350 (blue) starting from the first position fix after release (300s); b) linear plot of same D^2. Solid black lines are dispersion growth curves with time; Diffusive ($D^2 \sim t^1$), Ballistic ($D^2 \sim t^2$), and Richardson ($D^2 \sim t^3$).

Figure 3.10.   Drifter Dispersion Growth Curves

In the linear view, D^2 varies between the deployments, which represent different stages and wind directions of the synoptic storm. Initially (YD 346) the winds are northerly (Fig. 3.2a,b), and D^2 linearly increases before reaching a relative maximum

58

(4×10^6 m^2) in 0.5 days (Fig. 3.10a magenta line). Dispersion begins to increase and decrease over the remainder of the deployment around an asymptotic mean of 4×10^6 m^2. As the storm approaches JBP on YD 347, D^2 increases exponentially (Fig. 3.10 red line), which is associated with the deployment of drifters into a coastal jet (described below). As the winds shift direction to southerly, D^2 increases linearly (Fig. 3.10 green line) before reaching a similar relative maximum (4×10^6 m^2) in ~0.25 days. Dispersion is relatively constant for half of a day before increasing again to another relative maximum (7×10^6 m^2) as winds shift to northerly and increase in speed on YD 349. There is minimal initial growth for the YD 349 deployment (Fig. 3.10 orange line) until YD350 when the winds become light and variable and dispersion increases to a maximum of 7×10^6 m^2 in 1 day. Dispersion on YD 350 also increases quickly under light and variable winds, but after 1 day oscillates about an asymptotic mean of 3×10^6 m^2 (Fig. 3.10b blue line), similar to YD 346.

When drifters from two deployments are in the water at the same time, D^2 can be similar, as is the case on the afternoon of YD 350 (Fig. 3.10b orange and blue lines). However, in general, periods of convergence and divergence that constitute D^2 are unique spatially by deployment (Fig. 3.10b.) This highlights the heterogeneity of the surface flow in the nearshore region, which in the NGoMex is related to mesoscale wind forcing and submesoscale plume-induced coastal currents and fronts.

b. Observations of a Coastal Jet and Generation of Coastal Barriers

On YD 347, the wind direction shifts from northerly to northeasterly and the wind speed increases to 4 m/s at low tide (Fig. 3.2a,b). These easterly winds create a strong westward coastal jet that flows parallel to the beach away from the inlet, similar to the jet that existed on YD 342 when drifters were deployed in the inlet (Fig. 3.11; Fig. 3.5 red lines). The coastal jet is important for the mixing and transport in the nearshore region for two reasons: 1) it generates a horizontal velocity shear across the nearshore, and 2) it induces a coastal barrier that prevents surface material from moving onto the beach.

59
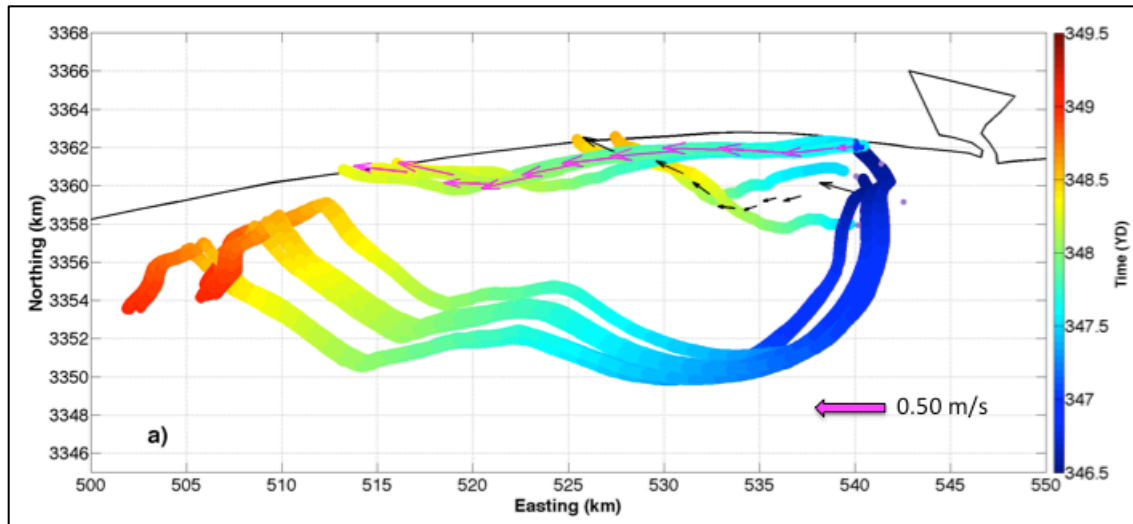
a) Offshore, oceanic drifter trajectories scattered with time show that drifters deployed on YD 346 bounce off the YD 347 coastal jet west of 515E on ~YD 348.6. The jet is represented by drifter trajectories parallel to the beach and scattered with time. The jet is fastest near the coast (magenta arrows) inducing shear with slower currents offshore (black arrows). CTD casts during drifter deployment show that the plume is least dense at the coast (blue circles). Purple circles represent the increase in plume density offshore.
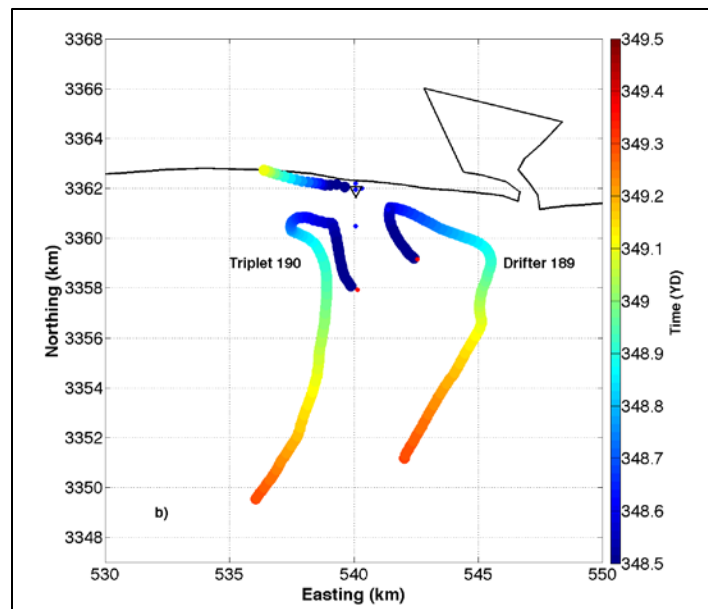
b) Four oceanic drifters deployed on YD 348 encounter a coastal barrier and deflect offshore. The barrier is indicated by an ADCP surface pathline that shows a westward current at the coast during the time that the drifters change course away from the beach (~YD 348.6). Blue circles again depict less dense plume water near the coast. Red circles show that the offshore drifters were deployed into dense oceanic water, as determined from CTD casts. Note Figure 3.11a and 3.11b have different scales for Easting and Northing.

Figure 3.11.   The Coastal Jet as a Cross-shelf Barrier to Drifters

In addition to the 15 drifters deployed from the inner shelf stations, 17 drifters are deployed outside the surf zone in approximately 1.5 m water depth on YD 347. CTD casts observe a 0.7 kg/m^3 horizontal density gradient between the second and third cross-shore deployment stations, with the least dense water near the beach (Fig. 3.11a, blue and purple circles). CTD casts also indicate that the plume extends to at least 9 m depth at the 10 m ADCP (Fig. 3.7a). Drifters deployed within 1 km of the beach trace the jet as it moves 25 km westward, down-coast at speeds of ~0.5 m/s before beaching (Fig. 3.11a, magenta arrows). The drifters deployed farther offshore also move westward, but at ~0.3 m/s or less before beaching 15 km away from the deployment stations (Fig. 3.11a, black arrows). This coastal velocity shear is responsible for the exponential increase in D^2 (Fig. 3.10b, red line). The YD 347 drifters all beach around the same time on YD 348, as the winds shift direction from easterly to southerly.

As the atmospheric front associated with the synoptic storm passes on YD 348, drifters deployed in oceanic water on YD 346 and YD 348 encounter the jet front between YD 348.5 to 348.7 and are barred from the beach (Fig. 3.2b; Fig. 3.11a,b). The YD 346 drifters, deployed during a moderate northerly wind, flow offshore initially (Fig. 3.11a). Easterly winds on YD 347 force the surface layer and YD 346 drifters to the west. Meanwhile, YD 347 drifters propagate down-coast within the newly developed coastal jet, as previously described. Soon after the start of YD 348, the wind shifts direction to southeasterly and the YD 346 drifters head toward the beach but hit the jet front, which acts as a coastal barrier, ~30 km west of the experiment site in the vicinity of 510E, 3358N and are redirected away from the coast (Fig. 3.11a).

An ADCP-derived surface pathline that originates at the time of YD 348 drifter deployment indicates that the surface current near the ADCP continues west throughout YD 348 (Fig. 3.11b). Here, the coastal front acts as a barrier to prevent four oceanic drifters that are transiting to the north from washing ashore. Of the four drifters, the three western drifters, Triplet 190, converge along the front and then are forced west by it for ~5 hours against the ambient surface current as winds shift clockwise out of the west, then northwest (Fig. 3.11b, Fig. 3.2b). During this period average speeds of Triplet 190 slow from ~0.24 m/s to less than 0.10 m/s. Conversely, Drifter 189 slows briefly when it

meets the front, but bounces to the southeast and regains its previous speed of ~0.12 m/s. This difference in trajectory and speed between the four drifters during interaction with the coastal barrier increases dispersion from YD 348.6 to 348.8 (Fig. 3.10b green line). Following atmospheric frontal passage, all four drifters continue south with the surface current forced by northerly winds.

c. *Observations of a Weak Coastal Current and Generation of Coastal Barriers*

On YD 350, the plume expands from the inlet in all directions when the winds are light and variable, <2 m/s (Fig. 3.2a,b). The boundary front associated with the plume bulge was visible ~0.50 km northeast of the 4.5 km deployment station due to convergence of foam and drifters, a darker color of water, and the congregation of birds (Fig. 3.12 arced solid blue line). Density differences are 1.5–2.0 kg/m^3, as measured by CTD casts on the west and east sides of the front near 541E, 3358N and 542E, 3361N (Fig. 3.12 red and blue circles). All drifters except one (542E, 3359N) are deployed in oceanic water. These drifters initially move southeast and then bounce off the bulge front and proceed to the west or northwest (Fig. 3.12 black lines and black arrows).
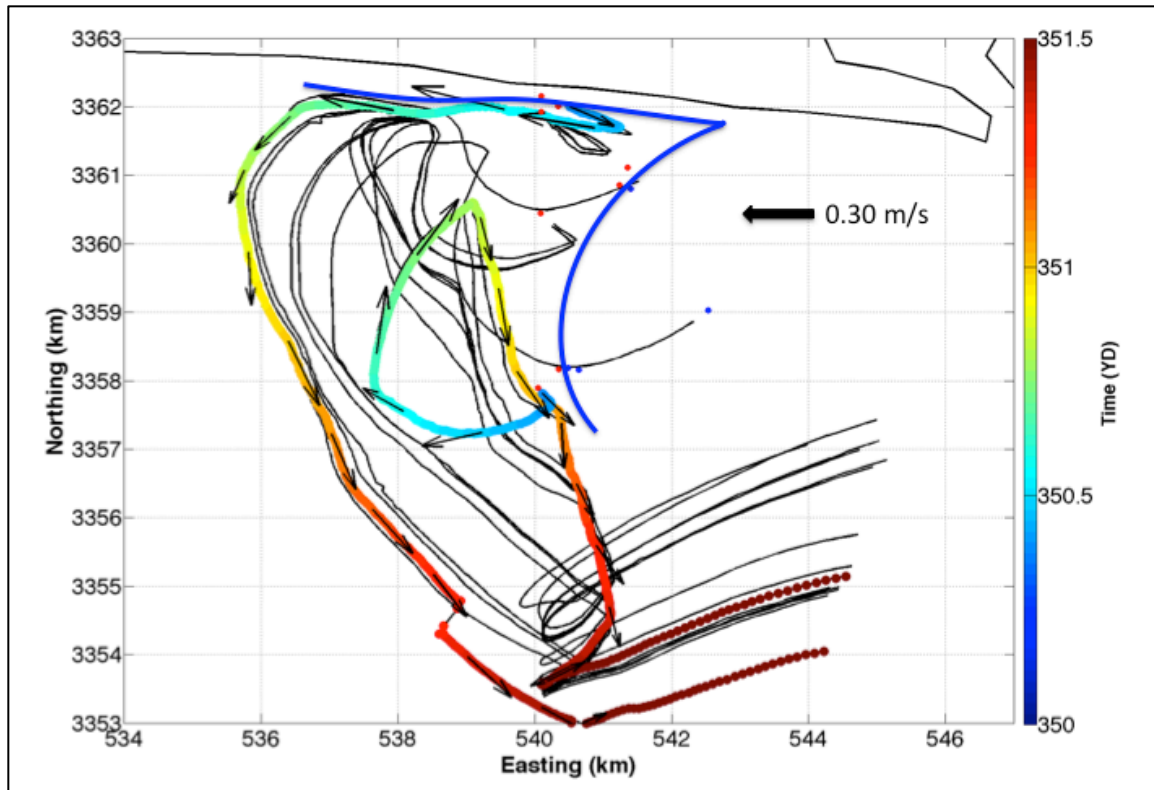
Drifters bounce off the bulge front and then interact with the coastal front on YD 350 before proceeding to the southeast (black lines and black arrows). A drifter from the 0.25 km station traces the edge of coastal front along 3362N and is colored by time. A similarly colored trajectory shows that a drifter from the 4.5 km station moves in the opposite direction at YD 350.7, highlighting the importance of the coastal barrier to surface material transport under light and variable winds. Solid blue lines are the visually observed bulge and coastal fronts. Red and blue circles indicate oceanic or plume water during drifter deployment and corroborate the presence of the expanding bulge.

Figure 3.12.   The Coastal Current as a Cross-shelf Barrier to Drifters

Closer to shore the front was visually observed to turn west and parallel the coast forming a coastal front (Fig. 3.12 solid blue line near 3362N). Drifters close to shore are barred from continuing to the beach by this coastal barrier and instead move along the front 0.50 km from the beach at speeds as high as 0.32 m/s until YD 350.7 when they turn to the south (Fig. 3.12 black arrows). In contrast, away from the coastal barrier, drifters deployed at the farthest offshore station continue north, not south, at YD 350.7 (Fig. 3.12 green segments with black arrows). By early YD 351 all drifters are moving south and begin to converge in the vicinity of 541E, 3355N. Multiple interactions

between drifters and fronts throughout the deployment lead to circuitous drifter paths, shear and the observed dispersion (Fig. 3.10b blue line).

D.   DISCUSSION

Natural coastal barriers are aperiodically created depending on wind speed and direction. They are present when winds >2 m/s have an easterly component and a coastal jet forms. Effective barriers also form when a weaker coastal current develops under light and variable winds (< 2 m/s). Wind speed and direction during ebb tide as the plume emerges are particularly important for barrier formation. During SCOPE, 8 of 13 days have winds that support barrier formation. Moderate winds with an easterly component during ebb tide are observed on YD 342, 345, 347 and 348. Light and variable winds during ebb tide are observed on YD 338, 339, 342, 343, and 350 (Fig. 3.2a,b).

The possibility of coastal barrier formation on eight days appears disproportionately high when considering the prevalence of moderate cross-shore winds compared to the frequency of moderate easterly or light and variable winds (Fig. 3a). However, rotary winds provide 2–3 opportunities for light and variable or easterly winds with the passage of each synoptic storm. Depending on the timing of these winds, formation of coastal barriers on 40–60% of days over a two-week period is reasonable, assuming 3 synoptic storms pass in two weeks. Sustainment of the barriers, however, appears to be tied to the persistence of the winds that formed the coastal barrier. This changes with each synoptic storm (gray dashed lines, Fig. 3.2b). The synoptic storm spanning YD 346–350 has the greatest period of moderate northeasterly winds of any of the three synoptic storms during SCOPE. These winds caused a coastal jet that persisted from YD 347 into YD 348, which is the longest observed.

Of the 75 drifters deployed from the inner shelf during passage of the synoptic storm (YD 346–350), the only drifters that made it to the beach were drifters deployed directly into the plume (26). Five more plume drifters and 44 oceanic drifters never washed ashore. Of the latter, 29 encountered the coastal barriers on YD 348 or YD 350 and were re-directed offshore (Fig. 3.11a,b; Fig. 3.12). The remaining 15 oceanic drifters did not beach because moderate northerly winds drove both the plume and ambient

64

surface flow offshore. Coastal barriers prevent more plume and oceanic drifters from washing ashore than moderate northerly winds (34 to 26), even if the 11 oceanic drifters that moved offshore initially with northerly winds on YD 346 are included in both groups (Fig. 3.11a). At synoptic storm time scales of ~5 days, coastal barriers are a significant physical mechanism that must be resolved to accurately determine the fate of surface material.

Results from the numerical modeling study by Xia et al. (2011) concerning the orientation of the wind-driven, small-scale Perdido Bay Estuary plume are consistent with the location of the Choctawhatchee Bay plume in the inner shelf under northerly and easterly winds. During no-wind conditions the Perdido Bay Estuary plume expands radially in all directions and is more expansive and less saline than plumes forced by strong winds from any particular direction (Xia et al. 2011). Radial expansion of the plume is consistent with bulge formation during SCOPE under light and variable wind conditions (Huguenard et al. 2016). The observed formation of coastal currents during these conditions are not reproduced by Xia et al. (2011), but are expected when the plume is unforced by winds (Fong and Geyer 2002; Horner-Devine et al. 2015).

Modeled southerly winds have two effects on the plume: 1) they inhibit the plume from flowing out of the inlet; and 2) they cause a salt flux into the mouth of the bay that reduces the plume structure (Xia et al. 2011). A plume that successfully emerges during these conditions is expected to be closer in density to the ambient oceanic water than plumes forced by easterly or light and variable winds. The associated boundary fronts are likely to be weak and mix quickly with the ambient water, causing any barriers that form to be limited temporally and in spatial extent down the coast. No barriers, or weak barriers, are anticipated on days of sustained southerly winds, which matches observations of oceanic drifters that move quickly northwest to the beach during SCOPE (Fig. 3.8b red lines; Fig. 3.9b).

Winter coastal barriers can be predicted by tracking the formation and propagation of synoptic storms. This is particularly important in NGoMex where the winds associated with these storms may simultaneously force several plumes to protect or expose multiple stretches of the coastline to oceanic pollutants. The question of what the

density difference needs to be between the inlet water and oceanic water to form an effective barrier at various distances from the inlet is left for future investigation. However, it is hypothesized that coastal barrier formation is less frequent and less effective during summer when predominantly southwest winds likely mix inlet waters to a near-oceanic salinity.

The Wind Regime Hypothesis Applied to the Deepwater Horizon Oil Spill

The SCOPE observations and findings are applied to winds that occurred during the DwH oil spill as a case study. From 20 April 2010 until 15 July 2010 oil spilled from the Macondo oil well 250 km southwest of the SCOPE site (Kourafalou and Androulidakis 2013) (Fig. 3.1). Westerly winds <5 m/s and the highest Mississippi River discharge during the active spill, 26,476 m^3/s on 28 May 2010, had pushed the resulting surface oil patch to ~88°W and 30°N, 25 km directly south of Mobile Bay and 73 km west of Pensacola by 01 June 2010 (YD 152) (Kourafalou and Androulidakis 2013). This marked the greatest northeast extent of the surface patch to that point in the spill. Prior to YD 152, the farthest east that oil had been confirmed to have washed ashore was Petite Bois Island, MS., just west of the Mississippi-Alabama border (YD 147), according to the NY Times online oil spill tracker (Aigner et al. 2010).

Winds shifted and became southerly at the end of May and increased to >5 m/s from YD 154–157 near the Mississippi Delta, indicative of summer winds in NGoMex (Gutierrez de Velasco and Winant 1996; Kourafalou and Androulidakis 2013; Valle-Levinson et al. 2015). Pensacola winds also shifted direction and became southerly by YD 151 and increased to ~5 m/s on YD 154. Predominantly southerly winds persisted through YD 166 and the surface oil patch spread along the Florida Panhandle past Destin (Kourafalou and Androulidakis 2013). As expected of beaches unprotected by coastal barriers, oil and/or tar balls started washing ashore (Aigner et al. 2010). Tar balls were confirmed to have arrived at Dauphin Island, AL. on YD 153. On YD 155, oil and tar balls arrived along a 65 km stretch of the Florida Panhandle from Perdido Key to Navarre Beach. Oil was confirmed at Fort Walton Beach, FL., 10 km west of Destin Inlet on YD 156 (05 June), well within the extent of the coastal barrier had it existed.

E.   CONCLUSION

A nearshore experiment (SCOPE) was conducted in an inner shelf within the northern Gulf of Mexico influenced by a river plume to determine how surface material, like oil, transits from deep water offshore to the beach. ADCP surface velocity observations, typically discarded from data analysis, are retained and indicate that wind and plume are the principal contributors to the speed and direction of the surface flow (<1 m) 500 m offshore. Wind and plume-driven surface velocities are ~4-7 times greater than the theoretical value of the wind and wave-driven surface currents. Despite prevalent cross-shore winds, the surface flow is predominantly southwest away from the beach (Fig. 3). Pathlines highlight the independence of the surface and subsurface flows (Fig. 3.6). Surface pathlines are useful for determining periods when the plume is oriented along the coast as a coastal current or jet (Fig. 3.11b).

The Choctawhatchee Bay plume, classified as a small-scale, wind-driven plume, adds heterogeneity to the nearshore by bringing cool, brackish water to the denser inner shelf water when it emerges from the inlet (Fig. 3.13). Plume boundary fronts are sources of shear that alter how drifters transit across the region and contribute to drifter dispersion $O(5x10^6 \text{ m}^2)$ (Fig. 3.10). Oil approaching the beach from offshore is also expected to converge and spread along plume boundary fronts (Fig. 3.13). Near the coast, the greatest dispersion ($>1x10^7 \text{ m}^2$) occurred when fast coastal jets $O(0.5 \text{ m/s})$ are generated by moderate winds (>2 m/s) with an easterly component. Coastal jets are an extension of the plume westward, parallel to the coast. A similar but weaker coastal current develops during periods of light and variable winds (<2 m/s). For both scenarios, drifters converge and change direction at the seaward coastal boundary front (Fig. 3.11; Fig. 3.12). These coastal barriers are 100% effective at barring drifters deployed outside the plume from beaching within 27 km west of Destin Inlet, and are expected to similarly prevent oil from washing ashore (Fig. 3.13).
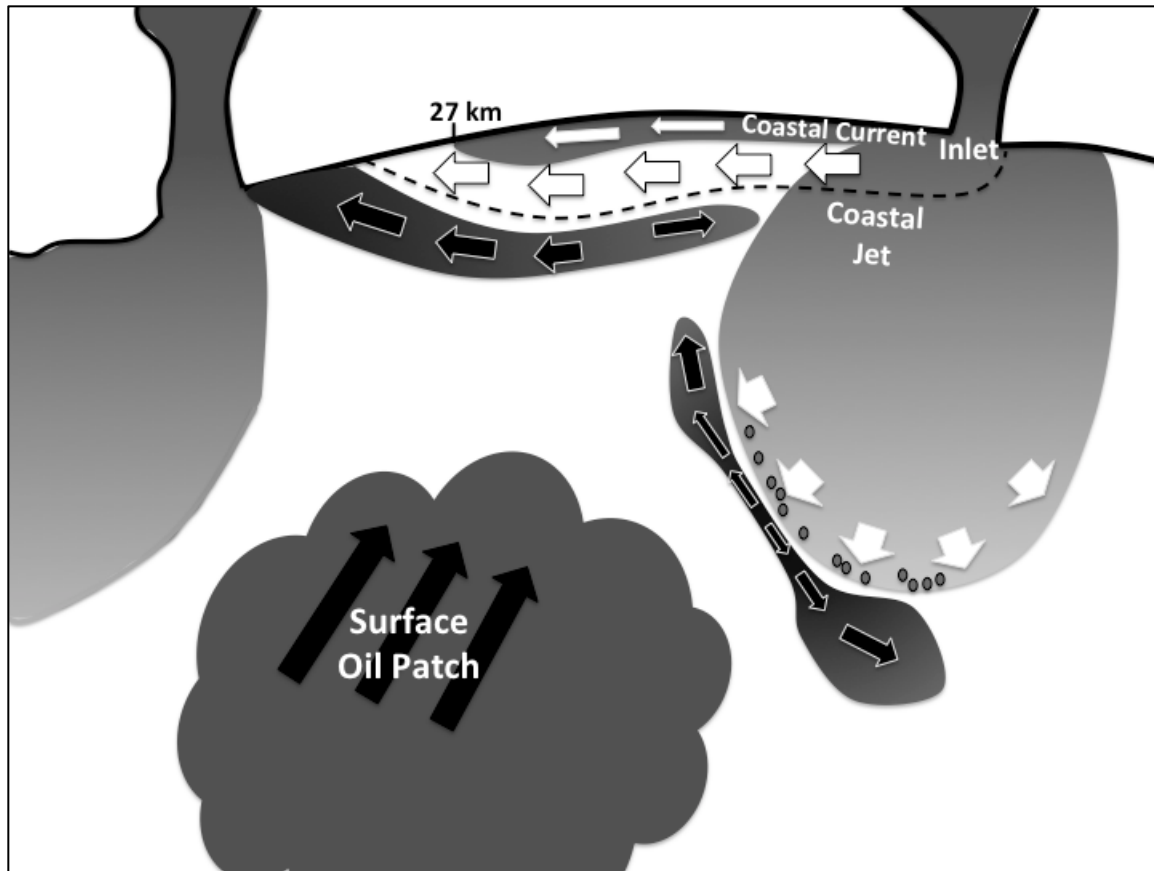
A small-scale buoyant river plume expands into the inner shelf creating a mid-field bulge and thin far field coastal current under no wind conditions. A comparatively wide and fast coastal jet emerges without formation of the bulge during periods when winds exceed 2 m/s and have an easterly component (black dashed line). Offshore oil is pushed up against the boundary front associated with both the bulge and coastal current or jet. Oil spreads along each front and the coastal front becomes a coastal barrier. Oil only reaches the beach in locations where the coastal barrier is absent. White arrows are cool, brackish estuarine water; black arrows are oil. Small dark dots inside the plume bulge represent flotsam and other surface material that align along the front.

Figure 3.13.   Conceptual Diagram of River Plumes as Coastal barriers to Oil in the Northern Gulf of Mexico

The presence of the plume in the inner shelf enhances the anisotropic conditions found in the coastal ocean and further challenges ocean circulation models to resolve submesoscale features that are needed to determine the detailed movement and fate of offshore oceanic pollutants. However, useful predictions of when and where oil will transport to the beach can be improved by forecasting the winds that cause coastal barrier formation. Natural coastal barriers are present during ~50% of the synoptic storm cycle

68

and are as effective at preventing surface material from washing ashore as moderate northerly winds that force the surface layer offshore. In both cases no drifters beach. These findings are particularly important in the northern Gulf of Mexico where a series of river inlets separated by distances <100 km may be forced simultaneously by mesoscale winds to create barriers along long stretches of the coast during the passage of synoptic storms (Fig. 3.13). During periods of moderate southerly winds when coastal barriers are absent or ineffective, oceanic pollution moves unimpeded to the beach, as it did in June 2010 following the Deepwater Horizon oil spill. In addition to improving prediction capabilities, wind- and plume-driven natural coastal barriers should be considered as part of the strategy to combat future oil spills and have implications for ecological, economic, and public health policies.

APPENDIX

The theoretical value of the wind and wave-driven surface current is estimated with the Lentz et al. (2008) inner shelf model using observational ranges from SCOPE. The wind velocities obtained at a height of 9.6 m from the NOAA station Pensacola (#8729840) were converted to wind stress,

$$\tau = \rho_a C_D W^2 , \tag{A1}$$

where ρ_a is the air density (1.22 kg/m^3), C_D is the drag coefficient (1.2x10^{-3}) and W is wind speed (0-6 m/s) corrected to an altitude of 10 m (Large and Pond 1981; Pond and Pickard 1983). The range of significant wave heights is computed from the ADCP deployed in 10 m water depth (Fig. 3.2c). A wave period of 3 seconds is used, representative of local wind-generated waves with short fetch observed during the experiment; the Coriolis parameter at JBP, 7.36x10^{-5} s^{-1}; and bottom roughness of $z_o = 10^{-3}$ m, consistent with Lentz et al. (2008) are also input to the model. The alongshore pressure gradient is assumed to be small and set equal to 0 m/s^2. The model-provided cubic eddy viscosity profile was selected following Fewings et al. (2008), who found that it provides realistic velocity profiles under cross-shore winds (Lentz 1995; Lentz et al. 2008). Model results indicate that the wind and wave-driven surface current in the top 1

meter of the water column is on average 1% of the observed wind speed (Fig. 3.14). The cross-shelf surface velocity shear profile during northerly winter winds at JBP is representative of enhanced flow at the surface caused by wind and undertow acting in the same direction, as described by Fewings et al. (2008).
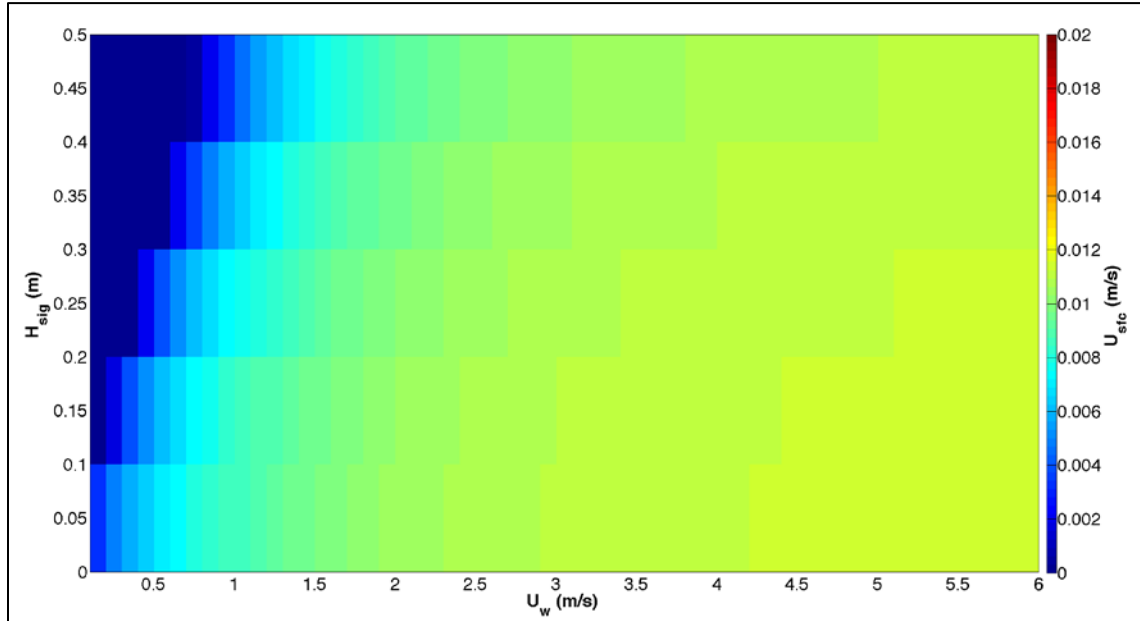
The average 1-m surface current as a function of wind speed (U_w) and significant wave height (H_{sig}) calculated with the Lentz et al. (2008) wind and wave-driven inner shelf model.

Figure 3.24.   Theoretical Value of Wind and Wave-driven Surface Current

IV. OBSERVATIONS OF SMALL-SCALE RIVER PLUME THICKNESS MODIFIED BY AMBIENT INNER SHELF CURRENTS AND WINDS

This chapter has been submitted to *Journal of Physical Oceanography* with minor formatting and content changes. As the main author of this work, I made the major contributions to the research and writing. Co-authors include Jamie MacMahan[a] and Kim Huguenard.[b]

A.   INTRODUCTION

Buoyant plumes that flow away from river mouths are a source of brackish water that create stratification within the coastal sea. Plumes dynamically classified as small-scale exit river inlets with strong advection, Froude numbers of $O(1)$, and are relatively unaffected by Coriolis (Garvine 1995, 1999). Small-scale plumes emerge into the inner shelf region with the ebb tide (Garvine 1984; Horner-Devine et al. 2015), and can be tide-driven (Garvine 1974b; O'Donnell 1990) or wind-driven (Xia et al. 2011; Gelfenbaum and Stumpf 1993). In addition to tides and winds, ambient inner shelf flows, river discharge, and coastline morphology determine the shape and orientation of the plume (Horner-Devine et al. 2015). Plumes typically consist of a near field region, where the river discharges, and a far field region, where the plume proceeds away from the inlet as a coastal current in the direction of a Kelvin wave (Horner-Devine et al. 2015; Hetland 2005).

When a coastal current develops in the far field region of the plume, it propagates as a gravity current (Lentz et al. 2003; Simpson 1982) with supercritical flow (Lentz and Helfrich 2002) and a propagating hydraulic jump at the leading edge (Garvine 1984, 1981). The interaction between the plume front and ambient shelf currents can result in velocity shear and the dissipation of the front through mixing (O'Donnell 1990; Horner-Devine 2015; Huguenard et al. 2016; Pritchard and Huntley 2006). Numerical solutions of the potential energy anomaly equation down shelf of the Rhine River and Patos

---

[a] Naval Postgraduate School.

[b] University of Maine, Orono, ME.

Lagoon find that alongshore straining, the deformation of the vertically-averaged horizontal density gradient by a velocity shear, and advection between the plume and ambient currents can maintain plume thickness and water column stratification (deBoer et al. 2008; Marques et al. 2010). These results suggest that straining and advection can preserve the plume as it extends along the coast, even as it mixes at the front edge. Coastal currents associated with large-scale plumes are observed to extend 100's of km from the inlet, affecting inner shelf processes far away from the source (Lentz et al. 1999; Garvine 1999). In the case of the Delaware Bay plume, the coastal current can connect to the Chesapeake Bay plume more than 200 km to the south (Garvine 1999).

Downwelling winds and ambient shelf currents aid down shelf transport in the far field by steering the buoyant plume water directly into the coastal current (Fong and Geyer 2002). Downwelling winds confine the current along the coast and deepen the plume, whereas upwelling winds spread the plume away from the coast and reduce the vertical plume thickness (Fong and Geyer 2001; Hetland 2005; Haus et al. 2003). When the plume is pressed up against the coast, the offshore plume boundary is a cross-shore transport barrier that prevents oceanic surface materials from reaching the beach (Roth et al., submitted). It is expected that relatively fast, thick plumes will extend coastal protection farther along the shelf than plumes that are relatively slow or thin.

In this study, the far field region of the plume is explored with a single Acoustic Doppler Current Profiler (ADCP) for 1 year in the inner shelf in 10 m water depth. Observations of plume structure and kinematics are evaluated with different wind forcing and inner shelf velocities.

B.   METHODS

1.   The Field Site

The Surfzone and Coastal Oil Pathways Experiment (SCOPE) was a two-week field experiment conducted in Choctawhatchee Bay and the adjoining inner shelf, within the Florida Panhandle (Fig. 4.1). Oil washed ashore in this region following the Deepwater Horizon oil spill (Aigner et al. 2010). The goal of SCOPE was to examine the physical processes that transport material, like oil, from the deep ocean to the beach

(Huguenard et al. 2016; Brouwer et al. 2015; Valle-Levinson et al. 2015; Roth et al., submitted; Roth et al., submitted b). A finding from SCOPE is that Choctawhatchee Bay plume is a cross-shore transport barrier to offshore surface materials away from the inlet (Roth et al., submitted).
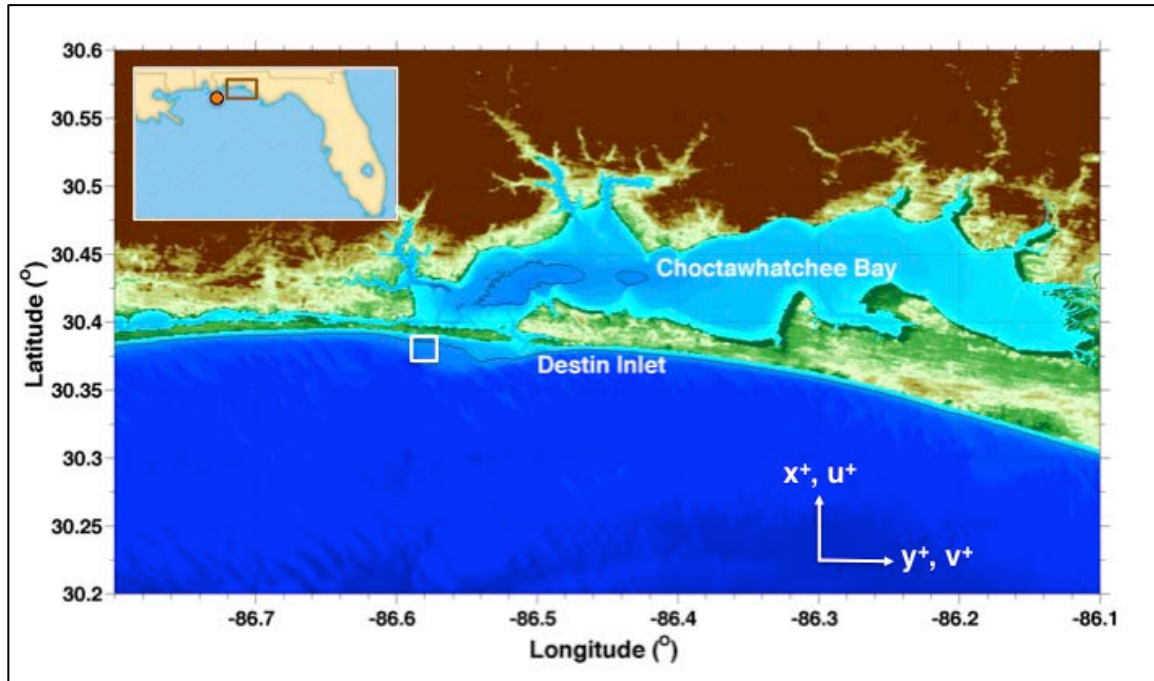
NOAA coastal digital elevation model of Choctawhatchee Bay and the adjacent inner shelf. White square indicates the location of the ADCP on the 10 m isobath. Inset shows the location of the experiment relative to the region. Orange circle represents the Orange Beach NOAA buoy and anemometer.

Figure 4.1.   Choctawhatchee Bay and the Adjacent Inner Shelf

Choctawhatchee Bay is the eastern-most bay along a latitudinal stretch of the northeastern Gulf of Mexico between Louisiana and the Florida Panhandle (Fig.1, inset). Seasonal winds are mainly cross-shore and driven by synoptic storms in the fall and winter, are from the southeast in the spring, and from the southwest in the summer (Gutierrez de Velasco and Winant 1996) (Fig. 4.2a). Circulation variability in this region is attributable to synoptic wind forcing (Ohlmann and Niiler 2005; Roth et al. submitted b). Similar to Mobile Bay and Perdido Bay to the west, the Choctawhatchee plume is

classified as small-scale and wind-driven (Gelfenbaum and Stumpf 1993; Xia et al. 2011).

2. Data Collection and Processing

Velocity observations were obtained from an Acoustic Doppler Current Profiler (ADCP) in 10 m water depth, 7 km west of Choctawhatchee Bay. The ADCP was deployed during SCOPE, as part of a cross-shelf array that included Conductivity, Temperature, and Depth (CTD) sensors, and then maintained for the next 12 months to observe the intra-annual variability of inner shelf flows. Cross-shore (U) and alongshore (V) velocities were sampled in 0.5 m bins at 1 Hz and averaged over 2.5 min. To prevent side lobe errors, surface bins are removed, limiting velocity analysis to $z < -1.5$ m, where z is the vertical coordinate and negative values are below the mean sea surface. The depth-averaged subsurface velocities in the remaining top 3 bins are described as $\bar{U}$ and $\bar{V}$ (Fig. 4.2a). Linear wave theory applied to a co-located pressure sensor reveals that Hrms is typically < 1 m (Fig. 4.2c). Wind stress is computed from hourly wind observations at the Orange Beach NOAA buoy following Large and Pond (1981), and reflect synoptic and seasonal patterns (Fig. 4.2b). Tides range from -0.1 m to 0.3 m and are classified as microtidal (Davies 1964; Dyer 1997) (Fig. 4.2d). River discharge ranged between 65 m^3 s^{-1} and 1460 m^3 s^{-1} with a normal seasonal cycle and mean annual discharge, 260 m^3 s^{-1}, that is within 1 standard deviation of the 85 year average (USGS 2016) (Fig. 4.2e). SCOPE 2.5 min averaged salinity data in 3 m water depth assists in the identification of passing plume fronts in 10 m water depth (Fig. 4.3c,f).
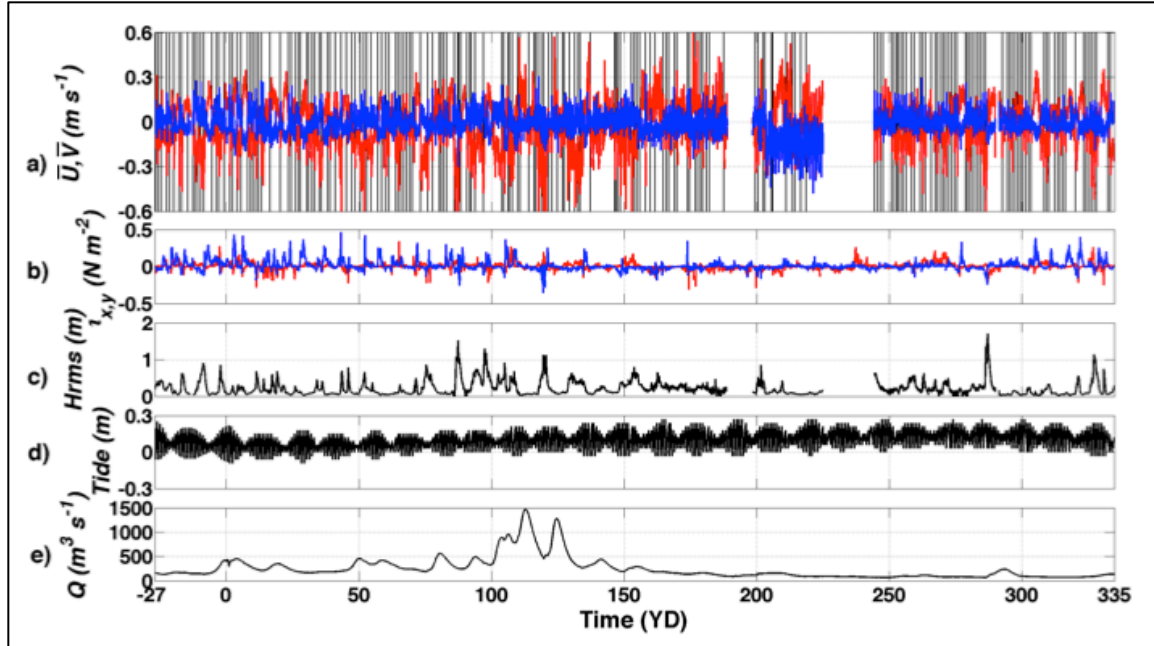
a) Cross-shelf (blue) and along-shelf (red) currents. Positive values are to the north and east. Vertical lines represent occurrence of plume front at the ADCP. b) Cross-shore (blue) and alongshore (red) wind stress. Positive values are from the north and from the east. c) Root mean square wave height. d) Tidal elevation at Destin. e) Choctawhatchee River discharge. Records extend from December 2013 until December 2014. YD < 0 are days in 2013.

Figure 4.2.   Annual Record of Currents, Wind Stress, Wave Height, Tide, and River Discharge

3.   Extraction of Plume Statistics from Inner Shelf Velocity Observations

The frontal region of each plume is distinguished from the ambient flow by a rapid acceleration in the along-shelf (y) and cross-shelf (x) directions (Fig. 4.3a,d,b,e). A well-timed, sharp decrease in salinity with the arrival of the plume fronts in both the along-shelf and cross-shelf velocity records is consistent with observations of passing plume fronts in the Columbia River plume (Stashchuk and Vlasenko 2009) and down shelf of the Chesapeake Bay (Lentz et al. 2003) (Fig. 4.3). This indicates that when the buoyant current thickens to full depth at the 3 m CTD the plume front extends at least 300 m offshore over the 10 m ADCP. It also provides confidence in selecting plume fronts for analysis based solely on rapid acceleration of currents when salinity observations are not available.

A year-long record of plume front statistics is produced with the along-shelf velocity observations (Fig. 4.3a,d). The ambient shelf flow, $\bar{V}_a$, is calculated from $\bar{V}$ 0–3 hours prior to plume arrival. The trailing edge of the plume front is visually recognized as an increase in V to > -0.2 m s^{-1}, or in the case of eastward ambient flow, a return to eastward currents above z = -3 m (Fig 4.3a,d, horizontal black line). In Figure 4.3, white arrows at z = -3 annotate the beginning and end of the plume front when $\bar{V}_a$ is to the west (Fig. 4.3a) and to the east (Fig. 4.3d). The plume velocity, $\bar{V}_p$, is the average $\bar{V}$ between the arrival and the end of the front. Plume thickness (d_p) is determined to be the maximum depth of westward flowing plume water between the beginning and end of the plume front, annotated as a third white arrow in Figure 4.3a,d.
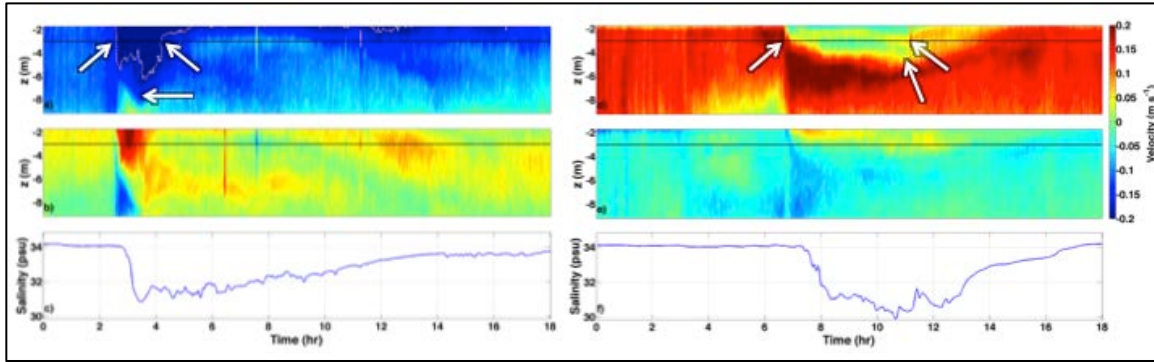
Passing fronts associated with the coastal current in the far field of the Choctawhatchee Bay plume. a-c) 2.5 min averaged along-shelf velocity (a), cross-shelf velocity (b), and salinity at 3 m water depth (c) for a plume front that flows west with the ambient currents. d-f) Same as a-c) but for a plume front that flows west in opposition to the ambient currents. Positive along- and cross-shelf velocities are to the east and to the north. Solid horizontal black line marks z = -3 m. White arrows mark the start, end, and thickness of the plume front. Dashed white line in 3a is -0.2 m s^{-1} contour.

Figure 4.3.   Plume Front Velocity and Salinity

C.   RESULTS AND DISCUSSION

More than 200 plume fronts are observed from December 2013 until December 2014 (Fig. 4.2a). 135 of the fronts are observed during periods when the ambient shelf flows to the west and the remaining 66 are observed when the ambient current is to the east, in opposition to the plume. $\bar{V}_a$ ranges from -0.3 m s^{-1} to +0.3 m s^{-1}, where negative is away from the inlet and positive is towards the inlet. $\bar{V}_p$ ranges from -0.5 m s^{-1} to 0 m

s^{-1}, and is always negative because the plume flows away from the inlet. $\overline{V}_p$ varies linearly with increasing $\overline{V}_a$ at the 95% confidence level ($r^2 = 0.53$), where $\overline{V}_p$ slows with slowing (-0.3 m s^{-1} < $\overline{V}_a$ < 0 m s^{-1}) and opposing ($\overline{V}_a$ > 0 m s^{-1}) $\overline{V}_a$. To reduce the visual bias associated with the scatter of observations, a mean value for $\overline{V}_p$ is calculated when there are 5 or more observations of $\overline{V}_p$ within $\overline{V}_a$ bins 0.1 m s^{-1} wide (Fig. 4.4a). The binned mean values of $\overline{V}_p$ are statistically independent at the 95% confidence level, owing to non-overlapping confidence intervals. 97% of the plume front velocities are faster than $\overline{V}_a$.

A similar technique is employed to examine the thickness of the plume front as a function of $\overline{V}_a$ (Fig. 4.4b). d_p varies linearly and inversely with $\overline{V}_a$ at the 95% confidence level ($r^2 = 0.50$), where d_p thins with slowing (-0.3 m s^{-1} < $\overline{V}_a$ < 0 m s^{-1}) and opposing ($\overline{V}_a$ > 0 m s^{-1}) $\overline{V}_a$. Note that the mean values of d_p in the (0 m s^{-1} < $\overline{V}_a$ < 0.1 m s^{-1}) and (0.1 m s^{-1} < $\overline{V}_a$ < 0.2 m s^{-1}) bins are not independent at the 95% confidence interval, indicating that the plume thins to ≤ 4 m with $\overline{V}_a$ > 0 (Fig. 4.4b).
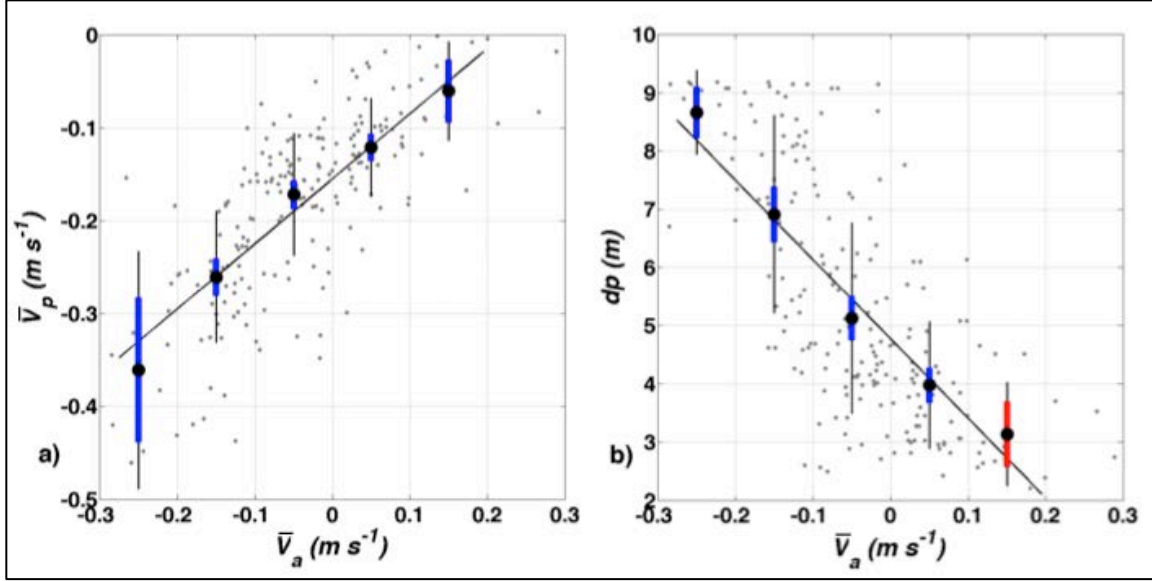
Comparisons of a) the plume front velocity, $\overline{V}_p$, and b) the plume front thickness, d_p, with the ambient along-shelf current, $\overline{V}_a$. Sloping black lines represent the best linear fit. Mean values (black bold circles) are calculated per 0.1 m s^{-1} wide bin of $\overline{V}_a$. Extending vertically from the mean values are standard deviations (vertical black lines) and 95% confidence intervals for either significantly independent (vertical bold blue lines) or not significantly independent (vertical bold red lines).

Figure 4.4.   Plume Front Velocity and Thickness versus Ambient Currents

It can be inferred from these linear relationships that when $\overline{V}_p$ and $\overline{V}_a$ are in the same direction ($\overline{V}_a < 0$ m s^{-1}) the mean d_p is greater than 4 m, but is typically less than 4 m when $\overline{V}_p$ and $\overline{V}_a$ are opposed ($\overline{V}_a > 0$ m s^{-1}). This indicates that mixing from velocity shear thins the plume when $\overline{V}_a > 0$ m s^{-1}. Huguenard et al. (2016) measured the rate of turbulent kinetic energy dissipation of the same plume to be O (10^{-5} m^2 s^{-3}) on YD -13 when $\overline{V}_p = -0.2$ m s^{-1} and $\overline{V}_a = 0.1$ m s^{-1}. This measurement is proportional to the variance of velocity shear assuming turbulence is homogenous and isotropic, and suggests that 59% of the plume is mixed at the front during the measurement period on YD -13 (Huguenard et al. 2016). Observations of turbulent kinetic energy dissipation rates are not available when $\overline{V}_a < 0$ m s^{-1}. However, numerical simulations of the small-scale wind-driven Patos Lagoon plume suggest that alongshore straining and advection thicken d_p when $Va < 0$ m s^{-1} and $Vp < 0$ m s^{-1} (Marques et al. 2010; Burrage et al. 2008).

The effect of cross-shore and alongshore wind stress, $\tau_{x,y}$, on d_p is evaluated for wind stress estimates averaged over the 3 hr period immediately before the plume arrives at the ADCP (Fig. 4.5). $\overline{\tau_{x,y}}$ are typically $O(0.1$ N m$^{-2})$ or less. 77% of plume fronts occur with downwelling winds, $\overline{\tau_y} > 0$. These fronts have an average $d_p = 5.8$ m, which is larger than the average $d_p = 4.0$ m during upwelling winds, $\overline{\tau_y} < 0$. When $\overline{\tau_y} < 0$ combine with offshore winds, $\overline{\tau_x} > 0$, the average d_p thins to 3.2 m. In contrast, when $\overline{\tau_y} > 0$, and onshore winds, $\overline{\tau_x} < 0$, combine the average d_p thickens to 6.2 m. For downwelling and onshore winds, d_p linearly increases with increasing wind stress in that quadrant at the 95% confidence level, though r^2 is reduced at 0.28. This result is consistent with downwelling winds thickening d_p by directly routing riverine water to the far field region and forcing the plume against the coast (Fong and Geyer 2001; 2002). Similarly, onshore winds push the plume against the coast, increasing d_p.
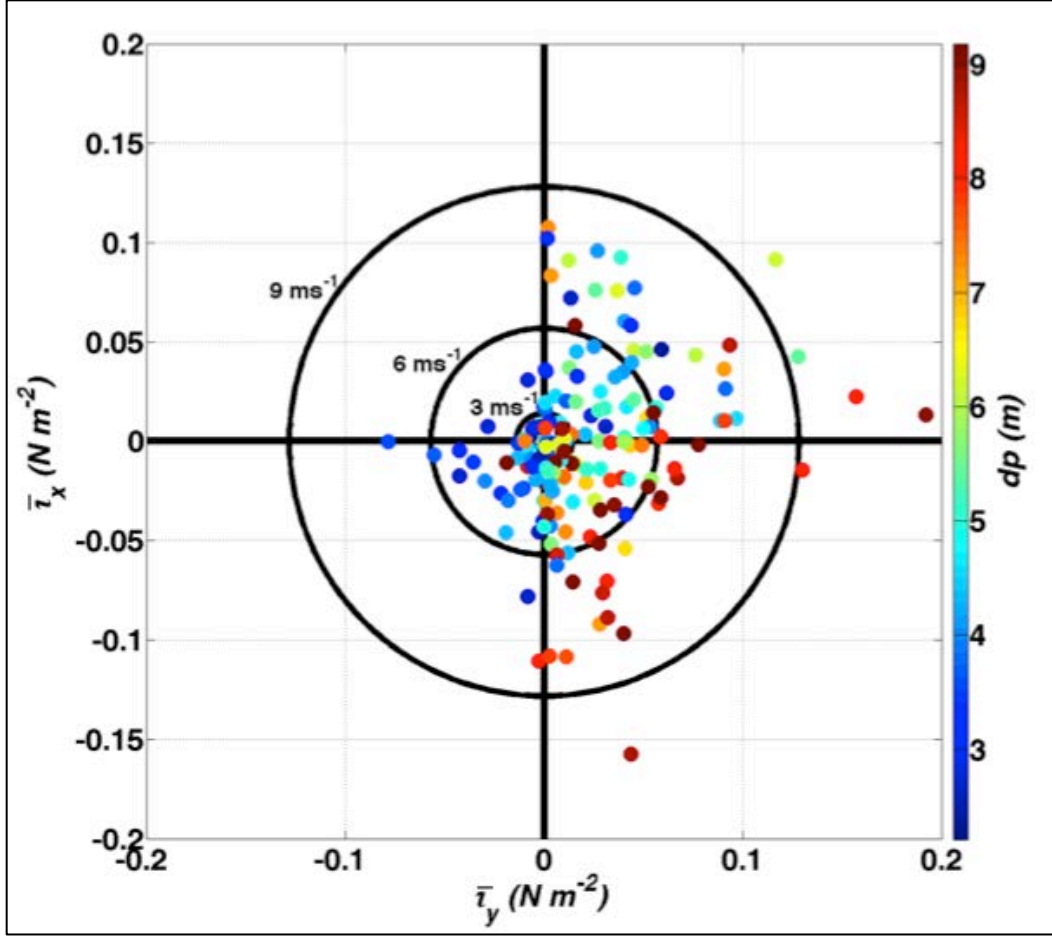
Plume front thickness scattered by 3-hr cross-shore and alongshore wind stress. Positive (negative) τ_y are downwelling (upwelling) favorable winds and positive (negative) τ_x are offshore (onshore) winds. Black rings represent the wind stress values corresponding to notional 3, 6, and 9 m s^{-1} wind speeds. Colors represent d_p with color scale plotted to the right.

Figure 4.5.   Plume Front Thickness Scattered by Wind Stress

D.   SUMMARY AND CONCLUSION

Plume front kinematics and thickness are analyzed with long-term inner shelf velocities and wind measurements. Plume front velocity ($\overline{V_p}$) ranges -0.5 m s^{-1} $< \overline{V_p} < 0$ m s^{-1}, and varies linearly, to the 95% confidence level, with the velocity of the ambient shelf currents, $\overline{V_a}$, that range -0.3 m s^{-1} $< \overline{V_a} < 0.3$ m s^{-1}. Plume thickness (d_p) has an inverse linear relationship with $\overline{V_a}$, to the 95% confidence level, and ranges 2 m $< d_p < 10$ m.

Wind stress is O(0.1 N m^{-2}) and principally downwelling prior to plume front arrival at the ADCP.

Downwelling winds enhance flow in the far field region, away from the inlet, and thicken the plume front, consistent with the findings of Fong and Geyer (2001, 2002). During these periods, $\bar{V_a}$ and $\bar{V_p}$ are both < 0 m s^{-1}, and straining and advection work in concert to thicken d_p to ≥ 5 m, thereby increasing water column stratification. $\bar{V_a} > 0$ m s^{-1} and upwelling winds promote frontal mixing and d_p thins to ≤ 4 m, reducing water column stratification. This effect is similar to a salt wedge estuary during flood tide, when along-stream straining and advection are in opposition (Giddings et al. 2011). In this way, the far field region of the plume is analogous to a displaced estuary that is supported by winds and reversing ambient currents, instead of tidal straining. $\bar{V_p}$ and d_p are likely measures of the effectiveness of small-scale plumes as cross-shelf barriers, and are modulated by winds and ambient currents as described by Fong and Geyer (2001, 2002), as well as straining and advection between $\bar{V_a}$ and $\bar{V_p}$ (deBoer et al. 2008; Marques et al. 2010). Plumes with thick, $d_p > 5$ m, and fast, $\bar{V_p} < -0.2$ m s^{-1}, fronts are expected to be the most persistent and extensive coastal barriers to surface material transport.

THIS PAGE INTENTIONALLY LEFT BLANK

V.   SUMMARY

Prediction of oil pathways from the Macondo Oil well to the beach in the NGoMex following the DwH oil spill demonstrated a need to improve understanding of the physical mechanisms within the inner shelf that drive material transport. Inner shelf material transport processes were observed during SCOPE at a beach within the Florida Panhandle where oil washed ashore six weeks after the DwH oil spill. The inner shelf is a transition zone between deep water and the surf zone where forcing mechanisms associated with the surface boundary, wind and waves; the bottom boundary, bottom friction; and the coastal boundary, river plumes and coastline curvature; can all be important to circulation patterns and material transport. All of these mechanisms were observed during SCOPE. Owing to small waves, constant bottom friction, and its proximity to Choctawhatchee Bay 7 km to the east, the experiment site was best suited for studying the effects of wind and river plume variability on material transport. The importance of coastline curvature and wind forcing were further investigated using numerical simulations from NAVGEM and HYCOM.

Winds are the principal forcing mechanism of material transport in the northern Gulf of Mexico. Synoptic patterns drive the circulation (Ohlmann and Niiler 2005). In the synoptic winter, cold air outbreaks pass across the region every 3–10 days bringing strong cross-shore winds that can reverse the along-shelf currents (V = -0.20 m s^{-1} to V = 0.20 m s^{-1}) within hours and maintain the direction of flow for days at a time. During these storms, the angle of approach of the storm relative to the orientation of the coastline is important for forcing along-shelf flows. When the cold front is perpendicular to the coast, cross-shore wind stress pre- and post-front drives along-shelf ageostrophic currents, which are the result of a balance between cross-shore wind stress, the Coriolis force, and the cross-shelf pressure gradient force. As the coastline curves toward Panama City, FL., the cold front is more parallel than perpendicular to the West Florida Shelf, and alongshore wind stress makes a larger contribution to the along-shelf currents. This is depicted in a conceptual diagram in Figure 2.13. Unlike other inner shelf studies that find along-shore wind stress and along-shelf pressure gradients drive along-shelf flows, here

cross-shelf pressure gradients set up by cross-shelf winds are the most important forcing mechanism of along-shelf currents.

Winds influence the small-scale Choctawhatchee River plume from the time it forms within the bay until it mixes fully with the ambient waters in the inner shelf. The initial direction of the plume as it entered the inner shelf is controlled by offshore and downwelling winds during ebb tide, as described numerically for the Perdido Bay, AL. plume 100 km west of Choctawhatchee Bay (Xia et al. 2011). The plume spills out into the inner shelf during light and variable wind conditions where it forms a re-circulatory bulge in the mid-field and a coastal current in the far field, characteristic of a prototypical plume (Horner-Devine et al. 2015). Downwelling winds and the ambient wind-driven currents force brackish water into the far field region of the plume (Fong and Geyer 2002), and the plume can flow at $O(-0.50 \text{ m s}^{-1})$ as a coastal jet . Downwelling winds also thicken the plume front to an average $d_p > 5$ m. Downwelling winds with an onshore component thicken the plume front to an average of $d_p > 6$ m. Conversely, upwelling winds thin the plume front to an average $d_p = 4$ m and promote frontal mixing.

The plume affects both along-shelf and cross-shelf material transport. Material within the plume spreads away from the inlet in the coastal current or jet as it extends along the coast. At the offshore boundary of the plume, where the edge is both a density gradient and a source of horizontal velocity shear, the plume becomes a cross-shelf barrier to material transport, as is shown conceptually for oil in Figure 3.13. During SCOPE, this barrier prevented 100% of drifters deployed outside of the plume from reaching the beach within 27 km west of the inlet. Along-shelf straining and advection between the ambient inner shelf currents and the plume front when $\overline{V_a} < 0 \text{ m s}^{-1}$ and $\overline{V_p} < 0$ m s^{-1} are expected to sustain the coastal barrier as it moves along the coast. When along-shelf straining and advection are in opposition, as is the case when $\overline{V_a} > 0 \text{ m s}^{-1}$ and $\overline{V_p} < 0$ m s^{-1}, mixing is expected to erode the coastal barrier. Based on wind records from May and June of 2010, the coastal barrier is not expected to have formed when oil washed ashore on the beaches of the Florida Panhandle.

Based on the results of SCOPE, natural coastal barriers are present during ~50% of the synoptic storm cycle. Their generation can be predicted by light and variable or downwelling winds during ebb tide. When they occur, they can be expected to protect the coast for kilometers away from the inlet, with the actual extent likely dependent on the direction of ambient currents and winds over the life of the plume. Coastal barriers formed from wind-driven river plumes are an important mechanism for material transport in the inner shelf. Nearshore circulation and oil prediction capabilities are likely to improve with the inclusion of this mechanism. Additionally, natural coastal barriers formed from plume fronts should be considered as part of the strategy to combat future oil spills.

THIS PAGE INTENTIONALLY LEFT BLANK

LIST OF REFERENCES

Aigner, E., J. Burgess, S. Carter, J. Nurse, H. Park, A. Schoenfeld, and A. Tse, 2010:
    Tracking the oil spill in the Gulf. *NY Times* online, Accessed 14 October 2016.
    [Available online at http://www.nytimes.com/interactive/2010/05/01/us/
    20100501-oil-spill-tracker.html?_r=0].

Beardsley, R. C., and B. Butman, 1974: Circulation on the New England continental
    shelf: Response to strong winter storms. *Geophys. Res. Lett.,* **1**, 181–184,
    doi:10.1029/GL001i004p00181.

Beardsley, R. C., H. Mofjeld, M. Wimbush, C. N. Flagg, and J. A. Vermersch Jr., 1977:
    Ocean tides and weather-induced bottom pressure fluctuations in the middle-
    Atlantic bight. *J. Geophys. Res.,* **82***,* 3175–3182, doi:10.1029/JC082i021p03175.

Brouwer, R. L., M. A. de Schipper, P. F. Rynne, F. J. Graham, A. J. H. M. Reniers, J. H.
    MacMahan, 2015: Surf zone monitoring using rotary wing Unmanned Aerial
    Vehicles. *J. Atmos. Ocean. Technol.,* **32(4)***,* 855–863, doi: 10.1175/JTECH-D-14-
    00122.1.

Brown, J., J. MacMahan, A. Reniers, and E. Thornton, 2009: Surf zone diffusivity on a
    rip-channeled beach. *J. Geophys. Res.*, **114**, C11015, doi:10.1029/2008JC005158.

Burrage, D., J. Wesson, C. Martinez, T. Perez, O. Moller Jr., and A. Piola, 2008: Patos
    Lagoon outflow within the Rio de la Plata plume using an airborne salinity
    mapper: Observing an embedded plume. *Cont. Shelf Res.,* **28**, 1625–1638,
    doi:10.1016/j.csr.2007.02.014.

Chapman D. C., and S. J. Lentz, 1994: Trapping of a coastal density front by the bottom
    boundary layer. *J. Phys. Oceanogr.*, **24**, 1464–1479, doi:10.1175/1520-
    0485(1994)024<1464:TOACDF>2.0.CO;2.

Csanady, G. T., 1980: Longshore presure gradients caused by offshore wind. *J. Geophys.
    Res. Oceans,* **85***,* 1076–1084, doi:10.1029/JC085iC02p01076.

Csanady, G.T., 1982: *Circulation in the coastal ocean*. D. Reidel Publishing Company,
    279 pp.

Crout, R. L., 1983: Wind-driven, near-bottom currents over the west Louisiana inner
    continental shelf. Dissertation, Louisiana State University, Baton Rouge, 117 pp.

Dagg, M. J., 1988: Physical and biological responses to the passge of a winter storm in
    the coastal and inner shelf waters of the northern Gulf of Mexico. *Cont. Shelf
    Res.,* **8***,* 167–178, doi:10.1016/0278-4343(88)90052-0.

Davies, J. H., 1964: A morphogenetic approach to world shorelines. *Z. Geomorphol.,* **8**, 127–142.

deBoer, G. J., J. D. Pietrzak, J. C. Winterwerp, 2008: Using the potential energy anomaly equation to investigate tidal straining and advection of stratification in a region of freshwater influence. *Ocean Modelling*, **22**, 1–11, doi:10.1016/ j.ocemod.2007.12.003.

DiMego, G. J., L. F. Bosart, and G. W. Endersen, 1976: An examination of the frequency and mean conditions surrounding frontal incursions into the Gulf of Mexico and Caribbean Sea. *Monthly Weather Review,* **104***,* 709–718, doi: 10.1175/ 15200493(1976)104<0709:AEOTFA>2.0.CO;2.

Dyer, K. R., 1997: *Estuaries: a physical introduction*. John Wiley and Sons Ltd., 195 pp.

Dzwonkowski, B., and K. Park, 2010: Influence of wind stress and discharge on the mean and seasonal currents on the Alabama shelf of the northeastern Gulf of Mexico. *J. Geophys. Res.,* **115**, C12052, doi:10.1029/2010JC006449.

Dzwonkowski, B., K. Park, and L. Jiang, 2011: Subtidal across-shelf velocity structure and surface transport effectiveness on the Alabama shelf on the northeastern Gulf of Mexico. *J. Geophys. Res.*, **116**, C10012, doi:10.1029/2011JC007188.

Dzwonkowski, B., K. Park, J. Lee, B. M. Webb, and A. Valle-Levinson, 2014: Spatial variability of flow over a river-influenced inner shelf in coastal Alabama during spring. *Cont. Shelf Res.*, **74**, 25–34, doi:10.1016/j.csr.2013.12.005.

Feng, Z. and C. Li, 2010: Cold-front-induced flushing of the Louisiana Bays. *Journal of Marine Systems,* **82**, 252–264, doi: 10.1016/j.jmarsys.2010.05.015.

Fernandez-Partegas, J. and C. N. K. Mooers, 1975: A subsynoptic study of winter cold fronts in Florida. *Mon. Weather Rev.,* **103**, 742–745, doi:10.1175/1520-0493(1975)103<0742:ASSOWC>2.0.CO;2.

Fewings, M., S. J. Lentz, and J. Fredericks, 2008: Observations of cross-shelf flow driven by cross-shelf winds on the inner continental shelf. *J. Phys. Oceanogr.*, **38**, 2358–2378, doi:10.1175/2008JPO3990.1.

Fewings, M. and S. J. Lentz, 2010: Momentum balances on the inner continental shelf at Martha's Vineyard Coastal Observatory. *J. Geophys. Res. Oceans*, **115**, C12023, doi:10.1029/2009JC005578.

Fong, D. A., and W. R. Geyer, 2001: Response of a river plume during an upwelling favorable wind event. *J. Phys. Oceanogr.*, **106**, 1067–1084, doi:10.1029/ 2000JC900134.

Fong, D. A., and W. R. Geyer, 2002: The alongshore transport of freshwater in a surface-trapped river plume. *J. Phys. Oceanogr.*, **32**, 957–972, doi:10.1175/1520-0485(2002)032<0957:TATOFI>2.0.CO;2.

Garvine, R. W., 1974a: Dynamics of small-scale oceanic fronts. *J. Phys. Oceanogr.*, **4**, 557–569, doi:10.1175/15200485(1974)004<0557:DOSSOF>2.0.CO;2.

Garvine, R. W., 1974b: Physical features of the Connecticut River outflow during high discharge. *J. Geophys. Res.,* **79**, 831–846, doi:10.1029/JC079i006p00831.

Garvine, R. W., 1981: Frontal jump conditions for models of shallow, buoyant surface layer hydrodynamics. *Tellus,* **33**, 301–312, doi: 10.1111/j.2153-3490.1981.tb01753.x.

Garvine, R. W., 1984: Radial spreading of buoyant, surface plumes in coastal waters. *J. Geophys. Res.*, **89**, 1989–1996, doi: 10.1029/JC089iC02p01989.

Garvine, R. W., 1987: Estuary plumes and fronts in shelf waters: A layer model. *J. Phys. Oceanogr.*, **17**, 1877–1896, doi:10.1175/1520-0485(1987)017<1877:EPAFIS>2.0.CO;2.

Garvine, R. W., 1995: A dynamical system for classifying buoyant coastal discharges, *Cont. Shelf Res*. **15**, 1585–1596, doi:10.1016/0278-4343(94)00065-U.

Garvine, R. W., 1999: Penetration of buoyant coastal discharge onto the continental shelf: A numerical model experiment. *J. Phys. Oceanogr.*, **29**, 1892–1909, doi: 10.1175/ 1520-0485(1999)029<1892:POBCDO>2.0.CO;2.

Garvine, R. W., and J. D. Monk, 1974: Frontal structure of a river plume. *J. Geophys. Res.*, **79**, 2251–2259, doi:10.1029/JC079i015p02251.

Gelfenbaum, G., and R. P. Stumpf, 1993: Observations of currents and density structure across a buoyant plume front. *Estuaries,* **16**, 40–52, doi:10.2307/1352762.

Giddings, S. N., D. A. Fong, and S. G. Monismith, 2011: Role of straining and advection in the intratidal evolution of stratification, vertical mixing, and longitudinal dispersion of a shallow, macrotidal, salt wedge estuary. *J. Geophys. Res.,* **116**, C03003, doi:10.1029/2010JC006482.

Gildor, H., E. Fredj, J. Steinbuck, and S. Monismith, 2009: Evidence for submesoscale barriers to horizontal mixing in the ocean from current measurements and aerial photographs. *J. Phys. Oceanogr.*, **39**, 1975–1983, doi:10.1175/2009JPO4116.1.

Gutiérrez de Velasco, G., C. D. Winant, 1996: Seasonal patterns of wind stress and wind stress curl over the Gulf of Mexico. *J. Geophys. Res.*, **101**, 18127-18140, doi:10.1029/96JC01442.

Haus, B. K., H. C. Graber and L. K. Shay and T.M. Cook, 2003: Alongshelf variability of a coastal buoyancy current during the relaxation of downwelling favorable winds. *Journal of Coastal Research*, **19** (2), 409–420.

Haza, A. C., A. C. Poje, T. M. Özgökmen, and P. Martin, 2008: Relative dispersion from a high-resolution coastal model of the Adriatic Sea. *Ocean Modeling*, **22**, 48–65, doi:10.1016/j.ocemod.2008.01.006.

Hendrickson, J., and J. MacMahan, 2009: Diurnal sea breeze effects on inner-shelf cross-shore exchange. *Cont. Shelf Res.*, *29*, 2195–2206, doi:10.1016/j.csr.2009.08.011.

Hetland, R. D., 2005: Relating river plume structure to vertical mixing. *J. Phys. Oceanogr.,* **35**, 1667–1687, doi: 10.1175/JPO2774.1.

Horner-Devine, A. R., R. D. Hetland, and D. G. MacDonald, 2015: Mixing and transport in coastal river plumes. *Annu. Rev. Fluid Mech.*, **47**, 569–594, doi:10.1146/ annurev-fluid-010313-141408.

Huguenard, K. D., D. J. Bogucki, D. G. Ortiz-Suslow, N. J. M. Laxague, J. H. MacMahan, T. M. Özgökmen, B. K. Haus, A. J. H. M. Reniers, J. Hargrove, A. V. Soloviev, and H. Graber, 2016: On the nature of the frontal zone of the Choctawhatchee Bay plume in the Gulf of Mexico. *J. Geophys. Res. Oceans*, **121**,1322–1345, doi:10.1002/2015JC010988.

Henry, W. K., 1979: Some aspects of the fate of cold fronts in the Gulf of Mexico. *Monthly Weather Review,* **107***,* 1078–1082, doi: 10.1175/1520-0493(1979)107<1078:SAOTFO>2.0.CO;2.

Huh, O. K., L. J. Rouse Jr., N. D. Walker, 1984: Cold air outbreaks over the Northwest Florida Continental Shelf: Heat flux processes and hydrographic changes. *J. Geophys. Res.*, **89**, 717–726, doi:10.1029/JC089iC01p00717.

Kourafalou, V. H., and Y. S. Androulidakis, 2013: Influence of Mississippi River induced circulation on the Deepwater Horizon oil spill transport. *J. Geophys. Res. Oceans*, **118**, 3823–3842, doi:10.1002/jgrc.20272.

LaCasce, J. H., 2008: Statistics from Lagrangian observations. *Progress in Oceanography*, **77**, 1–29, doi:10.1016/j.pocean.2008.02.002.

LaCasce, J. H., and C. Ohlmann, 2003: Relative dispersion at the surface of the Gulf of Mexico. *Journal of Marine Research*, **61**, 285–312, doi:10.1357/ 002224003322201205.

Large, W. G., and S. Pond, 1981: Open ocean momentum flux measurements in moderate to strong winds. *J. Phys. Oceanogr.*, **11**, 324–336, doi:10.1175/1520-0485(1981)011<0324:OOMFMI>2.0.CO;2.

Lentz, S. J., 1995: Sensitivity of the inner-shelf circulation to the form of the eddy viscosity profile. *J. Phys. Oceanogr.*, **25**, 19–28, doi:10.1175/1520-0485(1995)025<0019:SOTISC>2.0.CO;2.

Lentz, S. J., R. T. Guza, S. Elgar, F. Feddersen, and T. H. C. Herbers, 1999: Momentum balances on the North Carolina inner shelf. *J. Geophys. Res. Oceans,* **104**, 18,205-18,226, doi: 10.1029/1999JC900101.

Lentz, S. J., and K. R. Helfrich, 2002: Buoyant gravity currents along a sloping bottom in a rotating fluid. *J. Fluid Mech.,* **464**, 251–278, doi: 10.1017/S0022112002008868.

Lentz, S. J., S. Elgar, and R. T. Guza, 2003: Observations of the flow field near the nose of a buoyant coastal current. *J. Phys. Oceanogr.,* **33**, 933–943, doi:10.1175/1520-0485(2003)33<933:OOTFFN>2.0.CO;2.

Lentz, S. J., M. Fewings, P. Howd, J. Fredericks, and K. Hathaway, 2008: Observations and a model of undertow over the inner continental shelf. *J. Phys. Oceanogr.*, **38**, 2341–2357, doi:10.1175/2008JPO3986.1.

Lentz, S. J., and Fewings, M. R., 2012: The wind- and wave-driven inner-shelf circulation. *Annual Review of Marine Science*, **4**, 317–343, doi:10.1146/annurev-marine-120709-142745.

Li, Z., and R. H. Weisberg, 1999a: West Florida shelf response to upwelling favorable wind forcing: Kinematics. *J. Geophys. Res. Oceans,* **104**, 13507-13527, doi:10.1029/1999JC900073.

Li, Z., and R. H. Weisberg, 1999b: West Florida shelf response to upwelling favorable wind forcing: 2. Dynamics. *J. Geophys. Res. Oceans,* **104**, 23427-23442, doi:10.1029/1999JC900205.

Liu, Y., and R. H. Weisberg, 2005: Momentum balance diagnoses for the West Florida Shelf. *Continental Shelf Research,* **25**, 2054–2074, doi:10.1016/j.csr.2005.03.004.

MacMahan, J., J. Brown, and E. Thornton, 2009: Low-cost handheld global positioning system for measuring surf-zone currents. *Journal of Coastal Research*, **253**, 744–754, doi:10.2112/08-1000.1.

MacMahan, J., J. Brown, J. Brown, E. Thornton, A. J. H. M. Reniers, T. Stanton, M. Henriquez, E. Gallagher, J. Morrison, M. Austin, T. Scott, and N. Senechal, 2010: Mean Lagrangian flow behavior on an open coast rip-channeled beach: A new perspective. *Marine Geology*, **268**, 1–15, doi:10.1016/j.margeo.2009.09.011.

Mariano, A. J., V. H. Kourafalou, A. Srinivasan, H. Kang, G. R. Halliwell, E. H. Ryan and M. Roffer, 2011: On the modeling of the 2010 Gulf of Mexico oil spill. *Dynamics of Atmospheres and Oceans*, **52**, 322–340, doi:10.1016/j.dynatmoce.2011.06.001.

91

Marmorino, G. O., 1982: Wind-forced sea level variability along the west Florida shelf (winter, 1978). *J. Phys. Oceanogr.,* **12***,* 389–405, doi: 10.1175/1520-0485(1982)012<0389:WFSLVA>2.0.CO;2.

Marques, W. C., E. H. L. Fernandes, and O. O. Moller, 2010: Straining and advection contributions to the mixing process of the Patos Lagoon coastal plume, Brazil. *J. Geophys. Res.,* **115**, C06019, doi:10.1029/2009JC005653.

NOAA National Centers for Environmental Information, U.S. Coastal Relief Model, 07 October 2016. [Available online at http://www.ngdc.noaa.gov/mgg/coastal/crm.html].

NOAA Office of Response and Restoration, 2010: Field Guide to NOAA's Oil Trajectory Maps, 17 October 2016. [Available online at http://www.response.restoration.noaa.gov/oil-and-chemical-spills/response-tools/deepwater-horizon-trajectory-maps-background.html.]

O'Donnell, J., 1990: The formation and fate of a river plume: a numerical model. *J. Phys. Oceanogr.,* **20**, 551–569, doi: 10.1175/1520-0485(1990)020<0551:TFAFOA>2.0.CO;2.

Ohlmann, J. C., and P. P. Niiler, 2005: Circulation over the continental shelf in the northern Gulf of Mexico. *Progress in Oceanography*, **64**, 45–81, doi:10.1016/j.pocean.2005.02.001.

Ohlmann, J. C., J. H. Lacasce, L. Washburn, A. J. Mariano, and B. Emery, 2012: Relative dispersion observations and trajectory modeling in the Santa Barbara Channel. *J. Geophys. Res.*, **117**, C05040, doi:10.1029/2011JC007810.

Olascoaga, M. J., F. J. Beron-Vera, L. E. Brand, and H. Kocak, 2008: Tracing the early development of harmful algal blooms on the West Florida Shelf with the aid of Lagrangian coherent structures. *J. Geophys. Res.,* **113**, C12014, doi:10.1029/2007JC004533.

Poje, A. C., T. M. Özgökmen, B. L. Lipphardt, B. K. Haus, E. H. Ryan, and A. C. Haza, G. A. Jacobs, A. J. H. M. Reniers, M. J. Olascoaga, G. Novelli, A. Griffa, F. J. Beron-Vera, S. S. Chen, E. Coelho, P.J. Hogan, A. D. Kirwan Jr., H. S. Huntley, and A. J. Mariano, 2014: Submesoscale dispersion in the vicinity of the *Deepwater Horizon* spill. *Proceedings of the National Academy of Sciences,* **111**, 12693–12698, doi:10.1073/pnas.1402452111.

Pond, S., and G. L. Pickard, 1983: *Introductory Dynamical Oceanography*. Butterworth-Heinemann, 329 pp.

Poulain, P-M, 1999: Drifter observations of surface circulation in the Adriatic Sea between December 1994 and March 1996. *J. Marine Systems,* **20***,* 231–253, doi:10.1016/S0924-7963(98)00084-0.

Price, J. F., 1976: Several aspects of the response of shelf waters to a cold front passage. *Memoirs of the Royal Society of Liege, 6,* 201–208.

Pritchard, M., and D. A. Huntley, 2006: A simplified energy and mixing budget for a small river plume discharge. *J. Geophys. Res.,* **111**, C03019, doi:10.1029/2005JC002984.

Robertson, C., and C. Krauss, 2010: Gulf spill is the largest of its kind, scientists say. *NY Times*, 16 October 2016, http://www.nytimes.com/2010/08/03/us/03spill.html.

Romero, L., Y. Uchiyama, J. C. Ohlmann, J. C. McWilliams, and D. A. Siegel, 2013: Simulations of nearshore particle-pair dispersion in Southern California. *J. Phys. Oceanogr.*, **43**, 1862–1879, doi:10.1175/JPO-D-13-011.1.

Roth, M. K., J. MacMahan, A. Reniers, T. M. Özgökmen, K. Woodall, B. Haus, (submitted): Natural coastal barriers to surface material transport in the northern Gulf of Mexico. *Cont. Shelf Res.*

Roth, M. K., D. Kuitenbrouwer, J. MacMahan, A. Reniers, and T. M. Özgökmen, (submitted): Along-shelf currents forced by cross-shore winds in the inner shelf of the northeastern Gulf of Mexico. *J. Geophys. Res.*

Schiller, R. V., V. H. Kourafalou, P. Hogan, and N. D. Walker, 2011: The dynamics of the Mississippi River plume: Impact of topography, wind and offshore forcing on the fate of plume waters. *J. Geophys. Res.,* **116**, C06029, doi:10.1029/2010JC006883.

Schmidt, W. E., B. T. Woodward, K. S. Millikan, R. T. Guza, B. Raubenheimer, and S. Elgar, 2003: A GPS-tracked surf zone drifter. *Journal of Atmospheric and Oceanic Technology*, **20**, 1069–1075, doi: 10.1175/1460.1.

Schroeder, K., J. Chiggiato, A. C. Haza, A. Griffa, T.M. Özgökmen, P. Zanasca, A. Molcard, M. Borghini, P.M. Poulain, R. Gerin, E. Zambianchi, P. Falco, and C. Trees, 2012: Targeted Lagrangian sampling of submesoscale dispersion at a coastal frontal zone. *Geophys. Res. Lett.*, **39**, L11608, doi:10.1029/2012GL051879.

Seim, H. E., B. Kjerfve, and J. E. Sneed, 1987: Tides of Mississippi Sound and the adjacent continental shelf. *Estuarine, Coastal, and Shelf Science,* **25**, 143–156, doi: 10.1016/0272-7714(87)90118-1.

Simpson, J. E., 1982: Gravity currents in the laboratory, atmosphere, and ocean. *Ann. Rev. Fluid Mech.,* **14**, 213–234, doi: 10.1146/annurev.fl.14.010182.001241.

Spydell, M. S., F. Feddersen, R.T. Guza, and W.E. Schmidt, 2007: Observing surf-zone dispersion with drifters. *J. Phys. Oceanogr.*, **37**, 2920–2939, doi:10.1175/2007JPO3580.1.

Stashchuk, N., and V. Vlasenko, 2009: Generation of internal waves by a supercritical stratified plume. *J. Geophys. Res.,* **114**, C01004, doi:10.1029/2008JC004851.

Swenson, M. S., and P. Niller, 1996: Statistical analysis of the surface circulation of the California Current. *J. Geophys. Res.*, **101**, 22631–22645, doi: 10.1029/ 96JC02008.

Thornton, E. B., and R. T. Guza, 1983: Transformation of wave height distribution. *J. Geophys. Res.,* **88***,* 5925–5938, doi: 10.1029/JC088iC10p05925.

U.S. Geological Survey, 2016: National Water Information System site information for USGS Station 02366500, Choctawhatchee River near Bruce, FLA., 13 October 2016. [Available online at http://nwis.waterdata.usgs.gov/nwis/ inventory/?site_no=02366500&agency_cd=USGS]

Valle-Levinson, K. Huguenard, L. Ross, J. Branyon, J. MacMahan, A. J. H. M. Reniers, 2015: Tidal and nontidal exchange at a subtropical inlet: Destin Inlet, Northwest Florida. *Estuar. Coast. Shelf Sci.*, **155**, 137–147, doi:10.1016/j.ecss.2015.01.020.

Wang W., W. D. Nowlin Jr., and R. O. Reid, 1998: Analyzed surface meteorological fields over the northwestern Gulf of Mexico for 1992–1994: Mean, seasonal, and monthly patterns. *Monthly Weather Review,* **126***,* 2864–2883, doi: 10.1175/1520-0493(1998)126<2864:ASMFOT>2.0.CO;2.

Xia, M., L. Xie, L. J. Pietrafesa, and M. M. Whitney, 2011: The ideal response of a Gulf of Mexico estuary plume to wind forcing: Its connection with salt flux and a Lagrangian view. *J. Geophys. Res.*, **116**, C08035, doi:10.1029/2010JC006689.

Yankovsky, A. E., R. W. Garvine, and A. Münchow, 2000: Mesoscale currents on the inner New Jersey shelf driven by the interaction of buoyancy and wind forcing. *J. Phys. Oceanogr.*, **30**, 2214–2230, doi:10.1175/1520-0485(2000)030<2214:MCOTIN>2.0.CO;2.

INITIAL DISTRIBUTION LIST

1.   Defense Technical Information Center
        Ft. Belvoir, Virginia

2.   Dudley Knox Library
        Naval Postgraduate School
        Monterey, California